University of Tennessee, Knoxville
Trace: Tennessee Research and Creative Exchange

Doctoral Dissertations

Graduate School

5-2017

Modeling, Analysis, Force Sensing and Control of Continuum Robots for Minimally Invasive Surgery

Caroline Bryson Black
University of Tennessee, Knoxville, cbryson5@vols.utk.edu

Recommended Citation

Black, Caroline Bryson, "Modeling, Analysis, Force Sensing and Control of Continuum Robots for Minimally Invasive Surgery. " PhD diss., University of Tennessee, 2017.
https://trace.tennessee.edu/utk_graddiss/4443

This Dissertation is brought to you for free and open access by the Graduate School at Trace: Tennessee Research and Creative Exchange. It has been accepted for inclusion in Doctoral Dissertations by an authorized administrator of Trace: Tennessee Research and Creative Exchange. For more information, please contact trace@utk.edu.

To the Graduate Council:

I am submitting herewith a dissertation written by Caroline Bryson Black entitled "Modeling, Analysis, Force Sensing and Control of Continuum Robots for Minimally Invasive Surgery." I have examined the final electronic copy of this dissertation for form and content and recommend that it be accepted in partial fulfillment of the requirements for the degree of Doctor of Philosophy, with a major in Biomedical Engineering.

Daniel C. Rucker, Major Professor

We have read this dissertation and recommend its acceptance:

William R. Hamel, Jindong Tan, Andrew J. Russ

Accepted for the Council:
Dixie L. Thompson

Vice Provost and Dean of the Graduate School

(Original signatures are on file with official student records.)

Modeling, Analysis, Force Sensing and Control of Continuum Robots for Minimally Invasive Surgery

A Dissertation Presented for the
Doctor of Philosophy
Degree
The University of Tennessee, Knoxville

Caroline Bryson Black
May 2017

© by Caroline Bryson Black, 2017
All Rights Reserved.

I dedicate this dissertation to my amazing husband, Justin.

Your support and love have made this work possible.

Acknowledgements

First and foremost, I would like to give thanks to the Lord for the wonderful blessings of strength, perseverance and opportunity to complete this work.

I have been supported by so many family, friends, and colleagues during my research but I would like to thank a few individually. My advisor, Dr. Caleb Rucker, took me on as his first graduate student and introduced me to the amazing world of robotics. He has taught me so much more than that, including the importance of throwing out my Bananagrams puzzle and starting over to make something even better. Also, I want to thank my other committee members, Dr. William Hamel, Dr. Jindong Tan and Dr. Andrew Russ. Your input and encouragement have greatly enhanced this work.

I also want to thank my fellow lab members: John Till for his invaluable de-bugging skills long with some extremely helpful C++ code, Andrew Orekhov for sharing his design skills, Ryan Ponten for sharing in the frustrations of long transmission sections, notching, and shape setting, Kaitlin Oliver-Butler for machining and manufacturing advice, and Vincent Aloi for helping me conquer control diagrams.

This material is based upon work supported by the National Science Foundation under CMMI-1427122 as part of the NSF/NASA/NIH/USDA/DOD National Robotics Initiative and Graduate Research Fellowship DGE-1452154. Any opinion, findings, and conclusions or recommendations expressed in this material are those of the authors and do not necessarily reflect the views of the National Science Foundation.

Abstract

This dissertation describes design, modeling and application of continuum robotics for surgical applications, specifically parallel continuum robots (PCRs) and concentric tube manipulators (CTMs). The introduction of robotics into surgical applications has allowed for a greater degree of precision, less invasive access to more remote surgical sites, and user-intuitive interfaces with enhanced vision systems. The most recent developments have been in the space of continuum robots, whose flexible structure create an inherent safety factor when in contact with fragile tissues. The design challenges that exist involve balancing size and strength of the manipulators, controlling the manipulators over long transmission pathways, and incorporating force sensing and feedback from the manipulators to the user.

Contributions presented in this work include: (1) prototyping, design, force sensing, and force control investigations of PCRs, and (2) prototyping of a concentric tube manipulator for use in a standard colonoscope. A general kinetostatic model is presented for PCRs along with identification of multiple physical constraints encountered in design and construction. Design considerations and manipulator capabilities are examined in the form of matrix metrics and ellipsoid representations. Finally, force sensing and control are explored and experimental results are provided showing the accuracy of force estimates based on actuation force measurements and control capabilities.

An overview of the design requirements, manipulator construction, analysis and experimental results are provided for a CTM used as a tool manipulator in a traditional colonoscope. Currently, tools used in colonoscopic procedures are straight and exit the front of the scope with 1 DOF of operation (jaws of a grasper, tightening of a loop, etc.). This research shows that with a CTM deployed, the dexterity of these tools can be increased dramatically, increasing accuracy of tool operation, ease of use and safety of the overall procedure. The prototype investigated in this work allows for multiple tools to be used during a single procedure. Experimental results show the feasibility and advantages of the newly-designed manipulators.

Table of Contents

1 Introduction **1**

1.1 Motivation . . . 1

1.2 Fundamental Contributions . . . 4

1.3 Background on Robotic Surgery . . . 5

1.4 Robotic Considerations for NOTES . . . 8

1.4.1 Colonoscopic Surgery . . . 9

2 Literature Review **15**

2.1 Continuum Manipulators . . . 15

2.1.1 Concentric Tube Manipulators . . . 17

2.2 Parallel Robots . . . 19

2.2.1 Parallel Continuum Robots . . . 20

2.3 Manipulator Analysis . . . 22

2.4 Force Sensing and Control . . . 23

3 General Kinematic Modeling for Flexible Manipulators **28**

3.1 Cosserat Rod Equations . . . 29

3.2 Distal Boundary Conditions . . . 32

3.2.1 Fixed Joints . . . 33

3.2.2 Torsionless Joints . . . 34

3.2.3 Spherical Joints . . . 35

3.3 Proximal Boundary Conditions . . . 36

3.3.1 No Base Plate Present 36

3.3.2 Base Plate Present 37

3.4 Solution Method for Forward Kinematics 39

3.5 Generalized Problem Formulations 41

3.6 Stacked Parallel Continuum Manipulator 43

3.6.1 Additional Unknowns, Constraints and Equations 45

3.7 Qualitative Model Validation 46

3.7.1 Prototype Design and Construction 46

3.7.2 Kinematic Simulation and Analysis 47

3.7.3 Experimental Validation 52

3.7.4 Buckling Experiments 53

3.8 Validation of PCR with Gripper 54

3.8.1 Design and Fabrication 54

3.8.2 Control Architecture 57

3.8.3 Workspace Analysis 59

3.8.4 Experimental Validation 63

3.9 Concentric Tube Modeling 68

4 Analysis of Flexible Manipulators **72**

4.1 Model Linearization 73

4.2 Efficient Computation of the Kinetostatic Matrices 74

4.2.1 Approximation of Jacobian in Teleoperation 77

4.3 Matrix Analysis 78

4.3.1 Pose Variations 82

4.3.2 Design Variations 84

4.3.3 Matrix Metrics 85

4.4 Non-dimensional Analysis 87

4.5 Force Application 90

5 Force Sensing and Control with Parallel Continuum Manipulators 92

5.1 Force Sensing . . . 92

5.1.1 Manipulator Construction . . . 95

5.1.2 Repeatability . . . 95

5.1.3 Data Collection . . . 96

5.1.4 Data Analysis . . . 96

5.1.5 Stiffness Calibration . . . 97

5.1.6 Results . . . 98

5.2 Passive Stiffness Control . . . 99

5.2.1 Simulation Results . . . 101

6 Continuum Robot Tool Manipulators for Colonoscopy 104

6.1 Design Specifications . . . 105

6.2 Instrument Manipulator Design . . . 106

6.2.1 Deployed Inside the Colonoscope . . . 107

6.2.2 Deployed Outside the Colonoscope . . . 115

6.2.3 Actuation Module Design . . . 116

7 Conclusions and Future Work 119

7.1 Future Work in Parallel Continuum Robot Modeling and Analysis . . . 119

7.2 Future Work in Stiffness Control . . . 120

7.3 Future Work in Tool Manipulators for Colonoscopic Surgery . . . 121

Bibliography 122

Vita 150

Chapter 1

Introduction

1.1 Motivation

Robotic manipulators have opened up a new world of precision and dexterity to human tasks that have historically ranged from extremely difficult and hazardous to essentially impossible. There have been recent innovations in the world of industrial (1; 2) and medical robotics (3; 4) that have fundamentally changed the way humans complete these tasks. These applications have created a community of researchers seeking to push the boundaries of theoretical robotics and apply their knowledge to solve complex problems that plague the world. This work is a contribution to the iterative process moving the collective effort forward in pursuit of safer and more stable robotic partners.

Flexible robotic systems have enjoyed increased interest in industry and research due to the potential for gains in inherent safety and passive compliance when interacting with fragile structures inside their workspace (5). These fragile structures can be humans in an industrial setting, or human tissue in a surgical setting. In the second case, robots have allowed surgeons to perform increasingly minimally invasive procedures that cause less damage to the surrounding healthy tissue. Minimally invasive techniques involve completing the surgical task with smaller incisions (6).

This has the immediate benefit of decreasing the amount of healing required for recovery which leads to shorter hospitals stays and decreased medical costs. Additional benefits of minimally invasive surgery for patients include: reduced risk for adverse effects, blood loss, and pain related to the invasiveness of the intervention. By contrast, a challenge with minimally invasive procedures is the increased difficulty for surgeons. These difficulties arise from the challenges associated with the distance the robot places between the surgeon and the fragile structures of the surgical site. By contrast, absent robotic assistance, surgeons must operate on fragile structures using rigid tools with limited reach that require both triangulation and a larger workspace.

New technologies in robotics and computer assistance has advanced minimally invasive surgery and helped to alleviate some of these challenges. With these tools, surgeons now enjoy an ergonomic operating position, magnified 3D visualization, increased precision, improved tool dexterity, human tremor filtration, and increased access to difficult surgical sites. The surgeon can now more directly control the motion of an instrument held by the robot. The robot's contribution has advanced to now precisely comply with the direction of the surgeon while scaling motion, eliminating tremors and following any pre-procedure instructions. An example of these instructions would include virtual fixtures which are geometrical constraints imposed on the tool by the robot via a control algorithm that disallows motion in certain areas of the workspace where the surgeon does not want the robot to go (7).

These benefits have been welcomed in a breadth of medical specialties. In 2014, there were more than 500,000 surgical procedures performed robotically (8). Most of these procedures were urological or gynecological. Robotic systems are also used in cardiology, pediatric surgery and general surgery.

While there are now several systems on the market for surgeons to use during procedures, there are still some human and technological limitations to their capabilities and applications. First, use of robotic surgical device requires advanced training and expertise to achieve optimal utilization. Additionally, the systems are normally quite large, requiring ample space, and further, they remove the surgeon from the bedside to a control input station. The largest of these systems are thus far relegated to use in laparoscopic procedures. Due to their size and effectiveness as compared to the cost, the overall appropriateness of these large systems have been questioned by some (9). Further, the removal of the surgeon from direct contact with tissue also creates a loss of haptic feedback. Additionally, the set up and calibration of most robotic systems represents a hindrance to the clinical team as well.

Minimally invasive techniques are pushing the limits of current tools both robotic and manual. There are some procedures now calling for a completely incisionless approach where tools are introduced via natural orifices called natural orifice transluminal endoscopic surgery (NOTES). In these procedures, robotic manipulators need to be introduced down a long flexible transmission section of a endoscope which can measure up to 5 feet in length. It is this particular application that has drawn much of the research in flexible manipulators. These procedures require robots that are small and dexterous enough to reach locations deep inside the body.

This application and the robots required for its success is the focus of this research specifically modeling formulations for accurate robot control, analysis methods to help make design choices, force sensing and control methods to aid in providing enhanced feedback and increased safety, and finally, prototyping methods to achieve accurate actuation over long transmission lengths found in endoscopic devices. The manipulators presented in this dissertation advance the technology and tools toward addressing these challenges. Parallel continuum robots (PCRs) provide a dexterous wrist-like structure with an open lumen for tool manipulation. The formulation of their kinetostatics can solve for the tip forces and moments when measuring the forces at the base of the robot. Concentric tube manipulators (CTMs) are long and slender, open-channel manipulators that are well suited for endoscopic deployment.

1.2 Fundamental Contributions

The contributions of this research are an analysis of PCRs and CTMs in the application of surgical tool manipulators, investigation of force sensing and control abilities of PCRs, and an analysis of a new prototype robotic endoscopic system designed for colon tissue resection. The work is supported by the following individual contributions.

Generalized Modeling of Parallel Continuum Robots The kinetostatic modeling of a PCR utilizes Cosserat rod theory and static equilibrium equations along with boundary conditions that are specified by the physical characteristics of the manipulator. These equations are solved through a iterative approach that guesses unknowns conditions and integrates the initial value problem till the boundary value problem has been solved to meet the desired tolerance. A generalized the modeling approach for PCRs is presented in Chapter 3 that allows for a wide array of problem types (various inputs and outputs). The modeling is also enhanced with a definition of multiple boundary conditions (joint types and base plates). With this approach, it is simple to define the type of PCR being used and solve for a variety of desired input/output configurations.

Multi-segment Parallel Continuum Robot Model Along with the generalized model of PCRs that is presented in Chapter 3, modeling of a multi-segment parallel continuum robot in the Stewart Gough configuration is also presented. Although an example of a physical system exists in a rudimentary form, kinematic modeling has not yet been achieved in this extended design. This model will enable control of a $6n$ DOF manipulator where the n is the number of modules.

Linearized Kinestatic Analysis of Parallel Continuum Robots In order to closely examine the kinematic and kinetostatic capabilities of the PCR, a linearized analysis method is required. In Chapter 4, the framework for such an analysis is presented utilizing the modeling methods of Chapter 3. Previously used methods of robotic analysis including Jacobian manipulability measures and ellipsoid visualizations are applied to compliance and force matrices common to all continuum robots.

Force Sensing and Control with Parallel Continuum Robots Due to the nature of the generalized modeling, it is possible to take commanded and sensed information from the actuation points of a PCR and estimate the tip position and tip wrench. The capabilities of PCRs to be used as "intrinsic force sensors" that utilize the actuator loads to estimate the force at the tip of the manipulator and the use of that sensed force for stiffness control is examined in Chapter 5.

Feasibility of Concentric Tube Manipulators for Endoscopic Deployment The final contribution is the study of a proof-of-concept prototype of a surgical endoscope with concentric tube manipulators deployed down the tool ports. The design is analyzed for surgical effectiveness of the manipulator and a physical prototype is prepared for bench-top validation.

1.3 Background on Robotic Surgery

The union of robotics and surgical techniques is a breakthrough in surgery that is driving not only advances in technology but also improvements in clinical techniques to further increase the quality and efficacy of surgical treatments. Robotics is delivering higher levels of dexterity, vision, and access than previous tools. Currently, there are four main categories of surgical robotic systems based on function and size (see Figure 1.1). Laparoscopic systems are usually large, rigid systems like the da Vinci© by Intuitive Surgical and the Raven I and II developed by the University of Washington and the University of South Carolina. These systems are well suited for laparoscopic surgery because of their ability to triangulate the tools in the open

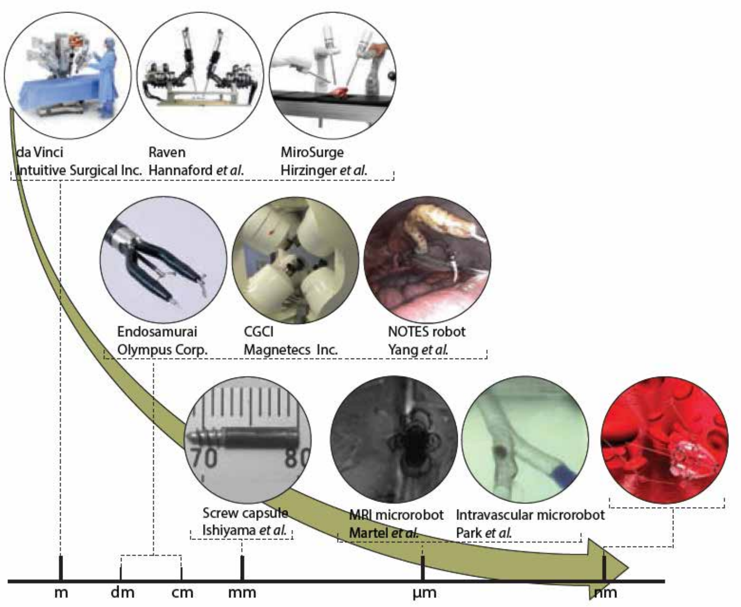
da Vinci
Intuitive Surgical Inc.
Raven
Hannaford et al.
MiroSurge
Hirzinger et al.
Endosamurai
Olympus Corp.
CGCI
Magnetecs Inc.
NOTES robot
Yang et al.
Screw capsule
Ishiyama et al.
MRI microrobot
Martel et al.
Intravascular microrobot
Park et al.
m
dm
cm
mm
µm
nm

Figure 1.1: This graphical representation of robotic manipulators shows their relationship based on size. The top manipulators on the meter scale while the bottom right corner is on the nanometer scale. This graphic appears in (10).

workspace of an insufflated (filled with air) body cavity. They have been well designed with considerable research on the engineering requirements for this category of operation (6). However, these systems are not without their challenges. They typically require a large footprint in the surgical suite, multiple operators to maintain and maneuver the tools, and they remove the doctor from the patient bedside. They also utilize long, rigid tools that are suitable for procedures like abdominal surgery but are challenged in more confined areas associated with natural orifice surgical approaches. The most important drawback to these systems is their current lack of sensory feedback in terms of forces applied to the tissue (11; 10). The endoscopic scale of surgical robot is more well suited for these types of procedures. The approach requires a long flexible instrument with multiple degrees of freedom (DOF) at the tip of a scope with a camera. This type of surgical robot is the focus of this research and is discussed in more detail below.

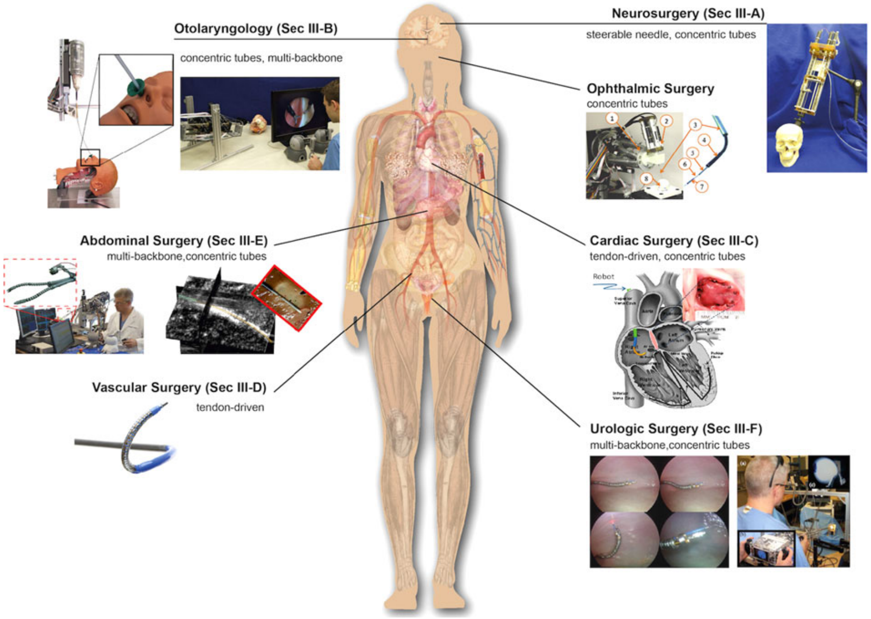
Otolaryngology (Sec III-B)
concentric tubes, multi-backbone
Neurosurgery (Sec III-A)
steerable needle, concentric tubes
Ophthalmic Surgery
concentric tubes
Abdominal Surgery (Sec III-E)
multi-backbone,concentric tubes
Cardiac Surgery (Sec III-C)
tendon-driven, concentric tubes
Robot
Vascular Surgery (Sec III-D)
tendon-driven
Urologic Surgery (Sec III-F)
multi-backbone,concentric tubes

Figure 1.2: This figure shows the progress of several research groups in using continuum robots in endoscopic surgical procedures. This graphic appears in (5).

Endoscopic procedure spaces (such as intraluminal or endoluminal) continue to necessitate an invasive and open approach due to the lack of appropriately designed robotic tools (11; 10). Thus, for these surgical needs, a different type of robotic manipulator is warranted for endoscopic procedures. The workspace is much smaller and usually consists of a long cylindrical lumen or requires navigating a complex path to reach the surgical site. The tools have to be passed through the tip of a rigid or flexible endoscope. The tools that do exist for endoscopic procedures are not dexterous and have to be actuated via non-intuitive torques of the tool and the scope. Currently there are no *commercially available* robotic systems for this type of procedure. However, several research groups are investigating this (12; 13; 14; 15; 16). The work of Simaan et. al. (17) provided a tele-operated robotic system to work in the throat. Another system by Choset (18) provides high DOF manipulator for cardiothoracic surgery. Another area of research includes the steerable needle systems (19; 20; 21). These systems are used for intravascular procedures and deep biopsies.

A summary of surgical systems by application is found in (5) and a Figure from this work is shown in Figure 1.2.

1.4 Robotic Considerations for NOTES

Natural orifice transluminal endoscopic surgery (NOTES) and the closely related endoluminal surgery (ELS) have experienced recent growth in research and application exploration both by surgeons and roboticists. This type of procedure represents the most significant innovation in surgery since the introduction of laparoscopy (22; 23) with the most promising application being direct-target NOTES. Direct-target NOTES procedures enter through natural orifices (i.e. the stomach, colon, or vagina) to reach procedure sites accessible via those orifices, and thus, they do not breach healthy tissue. By comparison, the hybrid NOTES uses laparoscopic ports/tools to complete the surgery, cutting into otherwise healthy tissue to then reach a surgical site and perform a procedure. The hybrid procedure provides assistance in tissue manipulation and visualization of the surgical field and has increased in use exponentially in rectal cancer surgery. However, when these additional incisions are made the benefits of a natural orifice approach are diminished. Patients can experience increased pain and wound complications while still being at risk for the co-morbidities of a pure NOTES procedure (tissue injury at point of access, bleeding and perforation) (24). This increased risk demonstrates the need for further enhancement of the tools available for direct-target NOTES procedures and specifically ELS procedures.

An ELS tool set currently consists of a rigid or flexible endoscope with multi-channel tool ports for cameras and surgical instruments. Since the camera extends from inside the scope, the field of view is narrow and limited due to the close proximity to the tools. The tools are also limited in their dexterity and range of motion. This limitation is compounded by the problem of spatial disorientation resulting from the movement of the scope required to manipulate the tools and the viewing angle of the embedded camera. Other limitations include limited force feedback at the tool tip and difficulty in controlling tool motions.

In order to achieve the level of safety and effectiveness needed for ELS surgery to achieve broader adoption, endoscopic tools need to be developed that address these concerns and provide small, flexible yet strong, dexterous manipulators capable of reaching difficult-to-access surgical sites via nonlinear pathways. A category of robots that promises to provide these capabilities is continuum robots.

1.4.1 Colonoscopic Surgery

One specific application that is examined in this dissertation is endoscopic submucosal dissection and resection of colorectal carcinoma. A discussion of the significance, surgical technique and robotic considerations is provided below.

Significance

The most common life-threatening disease of the digestive tract is colorectal carcinoma. Approximately 1 in 20 Americans will be diagnosed in their lifetime (25). Of these cases, 40% are diagnosed at the local stage, when the cancer has invaded the mucosa and submucosa, but has not yet penetrated the muscle layers of the colon wall and spread into the lymph nodes (see Figure 1.3 (b)). At this stage of the disease, open or laparoscopic surgery to remove a segment of the colon and anastomose the remaining ends back together is the current standard of care in the US. While these procedures are effective, they are invasive and pose a great deal of risk (infection (27%), non-infectious complications (14%), revision surgery (10%)) (26).

Treating early stage cancer from within the colon is ideal. Some carcinomas near the anal verge can be removed with laparoscopic instruments passed through the anus (27; 10; 28; 29), and small, pre-invasive polyps and lesions can be treated with endoscopic mucosal resection (EMR) during colonoscopy (30). However, as the tumors grow larger and deeper into the submucosa, the surgical procedure becomes more difficult and time intensive.

Endoscopic submucosal dissection (ESD) is a relatively new colonoscopic procedure developed to treat lesions that are larger, more advanced, and located further from the anal verge (see Figure 1.4 (a)). ESD has been proven more effective and less invasive than laparoscopic segmental resection (31). However, its widespread adoption has been hindered by the difficulty of manipulating dissection tools endoscopically (32) and the associated risks due to this difficulty. The surgeon must dissect through the inner submucosal layer, approaching, yet preserving, the musculature to protect against perforation and local paralysis.

In conventional EMR, ESD, and polypectomies, an endoscopist uses visual feedback from a distal camera to guide a colonoscope with a steerable tip to the site of the cancerous lesion (see Figure 1.4 (b)). An electrocautery knife is passed through a hollow tool channel in the colonoscope. In order to excise the cancerous tissue, this tool is inserted and activated by an assistant while the surgeon controls the steerable endoscope tip to guide the dissection. This requires the surgeon to turn knobs at the base of the colonoscope by hand to deflect the tip and the instruments together.

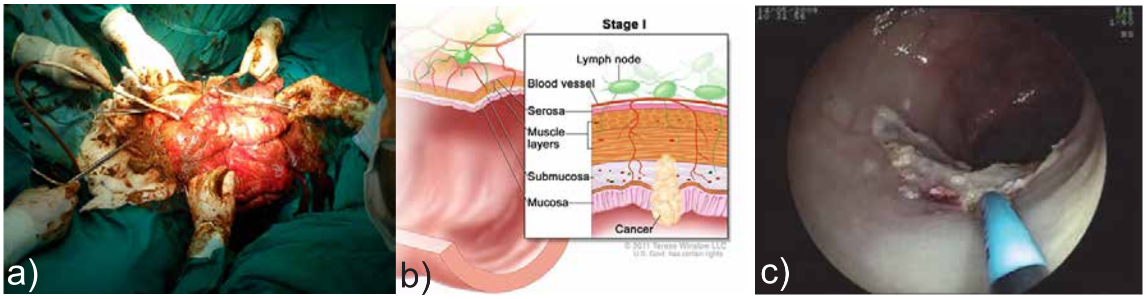

Figure 1.3: (a) The open surgical technique requires large incisions in the abdomen and breaching of the colonic wall. (b) The initial stages of colonic cancer begin in the mucosa and submucosa. It is possible to remove stage 0 or 1 tumors from within the colon using a natural orifice approach. (c) Endoscopic surgery uses a natural orifice approach with no incisions. However, current tools are rigidly attached to the endoscope and have limited dexterity.

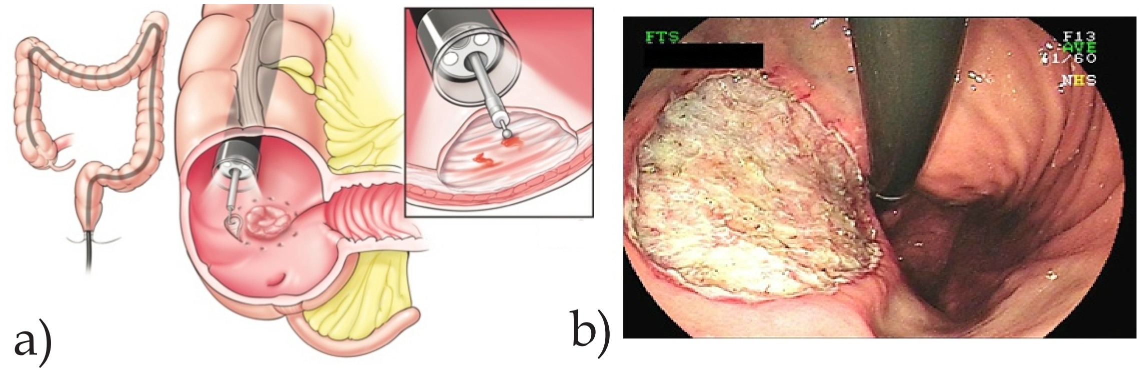

Figure 1.4: (a) ESD procedures involve navigating to a remote location in the colon via a steerable colonoscope and carefully dissecting cancerous tissue. b) A typical non-steerable electrocautery tool is shown, as seen from the endoscopic camera. The tool can be inserted along its axis, but the endoscopist must manually maneuver the entire scope tip and field of view in order to displace the tool tip vertically or horizontally. The dexterity afforded by this approach is highly limited, contributing to procedural difficulty, time, and risks.

The dexterity afforded by this approach is quite low, even when compared to the modest dexterity of laparoscopic surgery. While the tip can be deflected to move the tools, the angle of incidence between knife tip and tissue is essentially unchangeable. An added difficulty is that during colonoscope manipulation and steering, the entire field-of-view can shift in a counter-intuitive direction that is not always predictable due to colonoscope loop formations (33). Manipulating the colonoscope in this way contributes greatly to the difficulty of the procedure and its associated risks and implications discussed previously. ESD has an inherently larger risk of perforation due to the required dissection to the submucosa (which is the strongest layer in the intestinal wall (34)). Perforation can lead to possible permanent damage to the colon wall (requiring resection) as well as systemic infection of the abdominal cavity. Lower surgeon experience levels have been associated with a higher risk of perforation (35), indicating that the difficulty of manual endoscopic tool manipulation is a major barrier to performing this complex task at an expert level. Studies show a learning curve of 20-30 supervised cases (36; 37; 38) before an already experienced endoscopist can perform this procedure solo, and upwards of 100 cases before the risk of perforation decreases statistically significantly (35). Procedure time for ESD is also lengthy (40-90 minutes (39), and more than 120 minutes in difficult cases) serving to increase risks of other complications like infection (40) or blood clots due to the length of the procedure.

A robot-assisted endoscopic tool manipulation system can reduce difficulty, risk, and procedure time for colorectal ESD. The final chapter of this work provides an analysis and feasibility study of a robotically enhanced colonoscope designed to control instrument manipulators with greater DOF and dexterity than currently available tools. The long-term impact of this research will include increased adoption of the minimally invasive ESD approach resulting in reduced risks and cost, thus providing significant benefits to cancer patients who would otherwise suffer a more invasive and complicated segmental resection surgery, as well as reduced risk for their providers and healthcare institutions (Figure 1.3 (a)) as their only option.

A new robotic system also has the potential to impact procedures in a much broader range of surgical disciplines by providing a strong, dexterous, and intuitively controlled endoscopic instrument manipulator design. While colorectal ESD is the initial target application, the success of the new robotic system will also serve as a proxy and feasibility benchmark for any delicate endoluminal operation at a site accessible via flexible endoscopy. This includes surgery in the upper GI tract and the bronchial lumens as well as single-port abdominal surgery. In the long-term, the potential impact includes realizing novel procedures that are not currently performed endoscopically and making future natural orifice transluminal surgery (NOTES) procedures safer and easier to perform (41) in all areas of the body.

Related Work

Endoscopic deployment of continuum robots has been studied for several applications including neuroendoscopy (42), NOTES (43), and colonoscopies (44). Concentric-tube manipulators (as shown in Figure 2.2) have been recently proposed and advanced towards some surgical applications in other areas of the body, (e.g. neurosurgery (45), and cardiac surgery (46), thermal ablation in liver (47), and transurethral resection of the prostate (48)). However, the proposed project will be the first time that concentric tube manipulators have been applied to colonoscopic surgery. The most closely related work is the dual arm concentric tube endoscope for prostate surgery (48). This system uses a dual arm approach via a rigid endoscope. The system in Chapter 6 applies the dual arm paradigm via a flexible colonoscope. Another closely related system is the one in (49). The system utilizes a flexible endoscope with a single concentric tube and a steerable needle to biopsy lung tumors. It shows the potential for concentric tubes to be manipulated down an endoscope.

The strategy of using robotic, concentric-tube instrument manipulators is a significant departure from the strategies employed by all other flexible endoscopic systems investigated to date. First, there have been several *manually-operated* flexible platforms developed towards general NOTES (natural-orifice, transluminal, endoscopic surgery) procedures. These include the NOTES-scope and EndoSamurai (Olympus) (50), the incisionless operating platform (IOP; USGI medical) (51), the direct-drive endoscopic system (DDES; Boston Scientific) (52; 53), and the Anubis platform (Karl Storz) (54). In all of these systems, manually coordinating the DOF of the flexible endoscopes and steerable instruments simultaneously via knobs and levers is very challenging. Existing robotic platforms include efforts to robotize the Anubis scope (55; 56) and scope-mounted robotic instruments (MASTER (57; 58)). The MASTER uses tendons and sheaths that are controlled via the working channels of the endoscope and the manipulators are mounted on the front. The instruments attached at the end of the MASTER are fixed to the distal mechanism.

In contrast to these ongoing efforts, the robotic, concentric-tube approach has two main advantages: precise actuation and maximum strength and stiffness. All of the systems referenced above operate via the translation of braided steel Bowden cables routed through a flexible distal portion of the instruments. In those cases, high tension and precise control of cable displacements are required for accurate manipulation, but friction and cable stretch induce hysteresis, making the shape of the instruments difficult to predict and control.

Since the concentric-tube approach involves sliding the pre-curved tubes over each other rather than applying actuation torques with pairs of cables, precise movements can be achieved without imposing stringent requirements on actuation force and precision. In addition, solid concentric tubes can be much more stiff and strong than cable-driven designs, enabling them to apply the same forces to tissue while requiring less space and providing a hollow central working channel through which any flexible instrument can be passed. This is in contrast to all other systems which have specialized, unchangeable instruments integrated into the colonoscope structure (e.g. EndoSamurai, MASTER), or custom steerable instruments (e.g. Anubis, IOP, DDES).

Chapter 2

Literature Review

This section provides a review of robotic research that is relevant to the topics in this dissertation. Continuum and parallel robots are discussed in detail as they relate to the relevant robotic structures of this research, parallel continuum robots and concentric tube robots.

2.1 Continuum Manipulators

Continuum manipulators are continuously bending, infinite degree of freedom (DOF) robots with an elastic structure whose kinematics are modeled by the field of continuum mathematics. They are defined by their ability to take the shape of a smooth continuous curve and bend at any point along its backbone structure (59). Continuum manipulators are usually considered serial devices, due to their long slender shape, and the dominant geometric modeling paradigm is constant curvature arc segments tangentially connected in series, as reviewed in (60). However, the distinction between serial/hyperredundant devices and continuum devices is the finite number of joints. This boundary is not always clear when manipulator designs use continuously bending elements along with discrete joints. As some researchers have noted, many continuum designs also contain aspects resembling parallel architectures. For example, multiple entities are often constrained and connected in parallel within

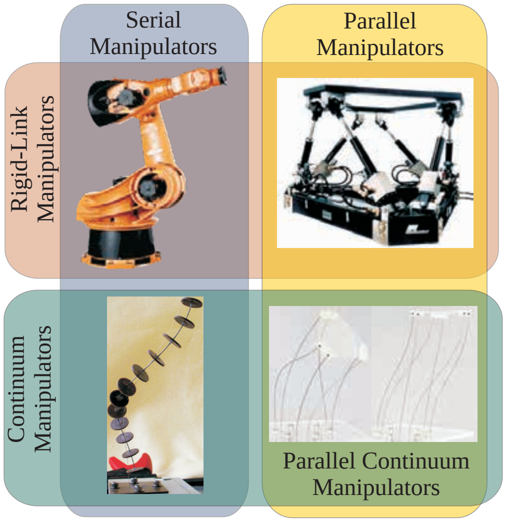

Figure 2.1: The landscape of manipulator structural types contains the broad categories of *serial* and *parallel* robots. Continuum robots have a slender elastic structure and are typically considered serial robots. Parallel continuum robots consist of the unification of parallel structures and continuous links. This graphic appears in (75).

a single arc segment to achieve 2-DOF bending actuation (e.g. pneumatic muscles (61), multi-backbone designs (62), multiple embedded tendons (63; 64; 65), and concentric precurved tubes (66; 67)). The fact that these arc segments are then arranged in series could lead one to categorize these as hybrid manipulators. Similar observations have been made in the case of concentric tube robots (66; 67), where the precurved nested tubes conform to an equilibrium shape in an analogous way to springs connected in parallel (68). One example in (17) consists of a central backbone and three secondary backbones constrained by spacer disks. Multiple entities are often connected in parallel within a single arc segment to achieve 2-DOF bending actuation (e.g. pneumatic muscles (69), multi-backbone designs (62), multiple embedded tendons (70; 71; 72), and concentric tubes (46; 73; 74; 67)). Thus, the majority of existing continuum robots would most accurately be categorized as either serial or hybrid manipulators.

There has been significant research into these types of manipulators, leading to designs and actuation strategies including cables and tendons (71; 76; 77), multiple backbone rods (17; 78; 79), pre-curved concentric tubes (80; 81; 82; 45; 83; 84), hydraulics (85; 86; 87), pneumatics (88; 89; 44), and shape-memory behavior (90; 91; 92; 93). There are now several survey articles focused on different aspects of continuum robots, including early reviews (94; 95), as well as recent reviews of soft robotics (primarily composed of easily deformable matter such as fluids, gels, and elastomers that match the elastic and rheological properties of biological tissue and organs) (96; 97; 98), snake-like robots (99; 100; 101), continuum robot modeling (60; 102), and robot strings (103). A recent review of emerging surgical robotic platforms (11) prominently highlights the ability of continuum robots to reach remote locations in the body through less invasive access routes due to their curved elastic structure.

Accurate modeling of the continuum manipulator will provide a geometric representation of the manipulator body via a kinematic and mechanics framework. These modeling structures incorporate the geometry of the design along with constitutive relationships and mechanics to relate loads from actuation and the external environment. The dominant geometric modeling paradigm is constant curvature arc segments tangentially connected in series, as reviewed in (60). While this choice is useful for a number of continuum robots, a more geometrically exact model is used for the manipulators in this research. The details of this modeling structure are shown in Chapter 3.

2.1.1 Concentric Tube Manipulators

A concentric tube manipulator (see Figure 2.2) consists of elastic, pre-curved tubes that are nested inside of one another concentrically. The shape of the needle-sized manipulator can be changed by axially rotating and translating each individual tube at the base. The curvature of the tubes enables a wide range of shapes to be

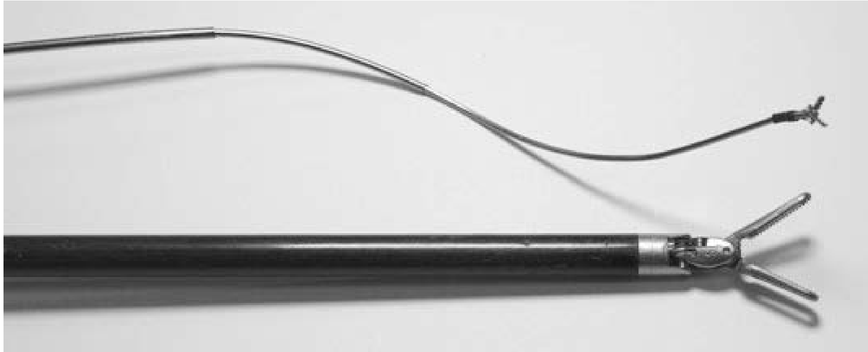

Figure 2.2: Concentric-tube robot with a standard da Vinci EndoWrist®. This graphic appears in (104).

achieved in a very small structure. The size of these manipulators makes them ideal for integration with a standard endoscope or colonoscope. This technique has been applied to a bronchoscope in (49).

In the trans-endoscope embodiment, concentric tube robots have been proposed for use in neurosurgery, transoral throat and lung surgery, and transgastric surgery with applications in transnasal skull base surgery (45), cardiac procedures (66), thermal ablation in liver (47), and transurethral resection of the prostate (48), among others. In the transvascular embodiment, concentric tube robots have been proposed for a variety of intracardiac procedures where they enter the heart through the vascular system. In the percutaneous, needle-like embodiment, applications that have been suggested include fetal umbilical cord blood sampling, ultrasound guided liver targeting and vein cannulation, vascular graft placement for hemodialysis, thermal ablation of cancer, prostate brachytherapy, retinal vein cannulation, epilepsy treatments, and general soft tissue targeting procedures. More information can be found in (104).

2.2 Parallel Robots

Parallel robots are closed-loop mechanisms whose end effector is linked to the base by several independent kinematic chains. Parallel manipulators have been the subject of robotics research since the early 1900s. They have been used in flight simulators, test beds, and manufacturing. As summarized in (105), “flexible” parallel robots have also been studied extensively, specifically in the context of how link flexibility affects the output stiffness mapping and manipulator dynamics. Other research includes design, modeling and control of planar parallel robots with compliant links (106; 107; 108; 109; 110; 111). Additionally work has been done on the control of flexible Stewart platforms (112; 113) and mechanical teleoperation of a cable-driven continuum robot using a parallel platform as the input device (114). These works are typically concerned with link deformations that are of small magnitude, modeled with lumped linear springs or distributed small-deflection Euler-Bernoulli beam theory. Furthermore, in the designs considered, the links only undergo deformation when external or inertial loads are present. During quasistatic operation in free space, the links behave as rigid members, and the joints carry no forces or moments.

Flexure joints and compliant mechanisms have been studied as a substitute for conventional structures in cases where the size, cost, or non-smooth nonlinearities must be minimized. Several unique, flexure-based, larger scale platforms have been developed and analyzed, including designs for finger rehabilitation (115), space deployed structures (116), large range modular units with compliant prismatic joints (117), 3 DOF translation platforms employing compliant cruciform hinges (118; 119), and flexure-jointed 6 DOF platforms (120; 121; 122; 123; 124).

In medical robotics, a parallel robot with series elastic actuation has been developed for ankle rehabilitation (125). Miniature parallel mechanisms have also been constructed for use in robotic capsule endoscopy, as in (126) where the universal joint at the base of each strut was replaced with a leaf spring to minimize size. Miniaturization is particularly important for minimally invasive robotic surgery, and

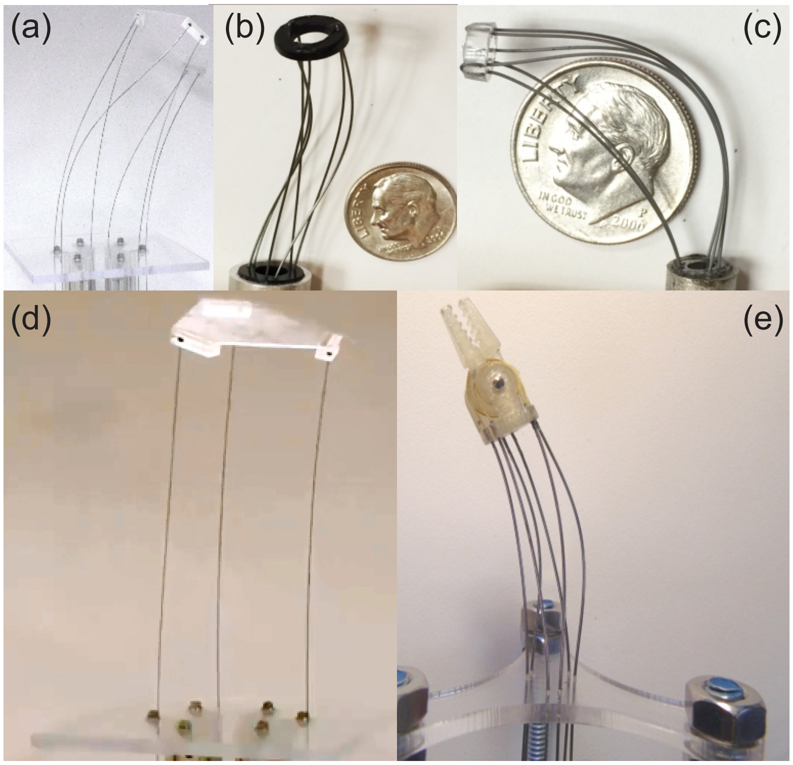

Figure 2.3: The parallel continuum design paradigm utilizes the translation of slender rods/tubes between constrained points to create large deformations in each of the flexible links. (a) Stewart Gough configuration with diameters of 87 mm, (b) 10 mm, and (c) 5 mm. (d) 3 link PCR. (e) Stewart Gough configuration 12 mm in diameter with grapser (128).

Merlet has developed a 3 DOF micro parallel robot, 7 mm in diameter, which is located at the end of an endoscope and actuated by the translation of rods outside the patient (105; 127).

2.2.1 Parallel Continuum Robots

A new and novel design of continuum robot that completes the fourth quadrant of the design space is the parallel continuum robot. A parallel continuum robot (PCR) is a manipulator with flexible elastic links arranged in parallel. Figure 2.3 shows several examples of PCRs with flexible links connected in different configurations, including the traditional 6 link Stewart-Gough pattern. The distal ends of the elastic links are connected to the end-effector platform, and the base of each link is independently translated by an actuator at its proximal end. This causes each compliant link to deform, giving rise to articulation of the end effector. This PCR design paradigm achieves multi-degree-of-freedom articulation and force sensitivity using a structure that is simple, inexpensive, lightweight, compliant, and easily scalable. These characteristics may be useful in micro-manipulation, endoscopic robotic-assisted surgery, and human-robot interaction. This manipulator design category is a natural extension of concepts presented in prior literature on continuum robots and parallel robots (60; 129; 62; 79; 130; 131), yet its design and potential advantages/tradeoffs have yet to be thoroughly investigated.

In comparison to serial continuum robots, parallel continuum designs are likely to have higher payload capacity and accuracy/repeatability. Compared to rigid-link parallel manipulators, they may exhibit greater compliance, larger workspace, and easier miniaturization to the the scale of a few millimeters in diameter or smaller. Their inherent mechanical compliance and low mass due to off-loading of the actuators can provide an important safety feature wherever parallel robots need to interact with humans. In the field of endoscopic robotic surgery, parallel continuum manipulators have the potential to provide precise, multi-DOF motion in a simple, compact, and short mechanism at the tip of an endoscope. As detailed in our prior work (132; 128), we believe that this type of design could improve robot-assisted surgical procedures by providing an easily miniaturized, remotely actuated manipulator that can achieve multi-DOF articulation in a confined space. Example procedures would include distal vein anastamosis, urethroplasty, ophthalmic surgery, and endoscopic/colonoscopic procedures. Another potential application is to provide a dexterous wrist for intra-abdominal surgeries on small structures. Parallel continuum robots are also potentially applicable to larger-scale industrial applications traditionally performed by rigid-link robots to facilitate safer operation around and in cooperation with humans. Because of the inherently lightweight, compliant nature of the design, collisions naturally result in deformation to the robot rather than injury to the human. Applications include any cooperative robot task where humans are in direct contact with the robot such as assembly of automotive components and inspection of complex systems (133).

Current manipulator designs most closely related to the PCR include the multi-backbone designs of Simaan et al. (134; 62), and the bionic tripod series of manipulators from the German company Festo (135). Multi-backbone designs typically employ serial bending segments along a primary backbone, each of which are actuated by the translation of three secondary backbone rods that terminate at the end of each segment. Within a segment, the rods are constrained by several intermediate spacer disks such that the robot shape can be described by a single backbone curve with piecewise constant curvature. A less constrained parallel continuum structure can be found in (136; 130; 137), where a mini-parallel wrist design employed 3 short, compliant rods connected to the end effector platform with ball joints. The Festo bionic tripod used the same concept, but relaxed the number of intermediate constraints to a single spacer and used 4 straight actuation rods to achieve 3-DOF articulation. Many other continuum robots also employ actuation strategies that can be categorized as parallel across a single manipulator segment with multiple segments concatenated in series (e.g. tendon-driven catheters (71), pneumatic arms (61; 138) and concentric-tube robots (46; 67)).

2.3 Manipulator Analysis

Robotic manipulators should be evaluated on their ability to perform the task in the design phase. If this is not a major step in the design of a surgical manipulator, the robot might not be able to perform the desired tasks to the satisfaction of the surgeon. Researchers have identified the importance of this analysis and striven to find appropriate metrics to analyze for their robotic designs. One of the design parameters that can be directly compared to the clinical application is the manipulator workspace. This metric can be matched to the surgical workspace via an optimization of the kinematic variables. Workspace analysis for continuum manipulators has been applied to several different systems (139; 93; 140; 141; 142; 143; 12; 144). There has also been work toward simplifying the surgical workspace to ease optimization. This is done by converting the complex geometries to simpler shape primitives. The next step in this process is to define the dexterous workspace and the non-dexterous workspace (145). Parallel manipulators have also been investigated in terms of manipulability and accuracy by Merlet in (146) and others (147; 148; 149). The most current catalog of robotic evaluation indices is contained in (150). Most of these measures are related to rigid, serial robots. However, there are some metrics that can be evaluated for continuum robots as well when examining ellipsoids of different kinematic matrices. The most current catalog of manipulator indices is contained in (150). Most of these measures are related to rigid, serial robots. Parallel manipulators have also been investigated in terms of manipulability and accuracy by Merlet in (146) and others (147; 148; 149). Analyses specifically relating to continuum robots have not been as extensively studied. Workspace analysis for continuum manipulators has been applied to several different systems (45; 141; 142; 143; 12; 144), and manipulability and force ellipsoids were investigated in (151), which also explored the compliance ellipsoid of continuum manipulators that related the change in a manipulator's position to an external force when the actuators are fixed. Kinestatic comparisons of different continuum robot designs have also been investigated in (152), where the output stiffness of three different manipulators was measured to compare the different physical designs. One goal of our current work is to provide a general framework for analysis of continuum manipulators in the context of characterizing parallel continuum robot performance.

2.4 Force Sensing and Control

Many clinicians and roboticists theorize the major limiting factor in the performance of robotic-assisted minimally invasive surgery (MIS) is the lack of haptic feedback (3).

When a surgeon is interacting with a tissue or organ, their own proprioceptive and cutaneous senses allow them to determine the appropriate amount of force to apply in order to minimize damage. This ability is removed when a robotic manipulator is interacting with the tissue. The force feedback also allows surgeons to distinguish diseased tissue from healthy areas via mechanical properties, identifying regions of lumps or tumors, and hardened or calcified portions of arteries (153; 154). The field of haptics seeks to provide the user of a tele-operated or virtual system with a realistic experience of an actual environment by providing them with the most intuitive and easy to understand information via electromechanical devices. There are two basic types of haptic feedback, tactile and force. Tactile feedback recreates sensations felt by the skin. This would include things like texture, temperature and pulsation. Force feedback replicates what a person feels from a solid boundary or object. This includes things like weight and inertia (155). It has been hypothesized that a greater degree of immersion into a virtual environment can be achieved with even rudimentary haptic devices than with more complex and higher defined visual displays alone.

Haptics research is a well-established field. The first time the concept was mentioned was by computer scientist Ivan Sutherland when he wrote that the ultimate display would allow users to feel virtual objects that could only be displayed graphically with a mechanical force-feedback device (156). This specifically refers to machine haptics in which the feedback is provided to a human user by an electromechanical device. In surgery, haptics can enhance simulations, provide vital information on tissue deformation and provide a surgeon with the feedback needed to perform complex tasks. However, sensing forces at the tip of small instruments in a confined space is a difficult design, computational, and mechatronic challenge.

Force sensors for surgical instruments would ideally be placed at the tip and provide 6 DOF measurement. However, challenges of biocompatibility, sterilization, and temperature sensitivity make this a difficult engineering task (3). Many instruments are also disposable and the cost of a high sophisticated sensor would limit its usability with these instruments. The solution becomes to place the sensors on the robotic manipulator that is outside the body. This also creates challenges because the forces encountered by the sensor can include friction in the manipulator actuation system and torques applied by the instrument at the point of insertion that can be large enough to mask the small tissue interaction forces.

Another option for force estimation involves teleoperation controllers, where the difference in the desired and actual position of the robot inside the body is an indication of the amount of force applied to the environment. One main example of this type of control method is the four-channel framework (157) where the position and force of both the master (surgeon controlled input device) and the slave (robotic manipulator inside the body) are sensed and influence the control of the manipulator. One assumption in this method is that the master and slave inputs and forces affect the output with the same dynamics. This would not be the case with compliant mechanisms. Other examples include position-position and position-force teleoperation.

While none of the commercially available systems provide a level of force feedback that would decrease damage to tissue, academic systems that include force feedback are being developed such as the RAVEN II at the University of Washington (158), an enhanced da Vinci robot (159), a laparoscopic robot (160), the NeuroArm and the LapRobot (161). Most of these systems use a method of measuring the force at the individual joints of the robot to estimate the force at the tip, a method called actuation-based force sensing.

Actuation-based force sensing is another topic that is well studied for classical rigid-link manipulators but has not been widely studied for continuum robots. In conventional rigid-link designs, end-effector wrench is mapped to the joint torques by the transpose of the Jacobian matrix (162) due to conservation of energy. For continuum robots, this simple relationship does not hold true due to the elastic energy stored within the robot links. Gravagne showed in (151) that the principal of virtual work can account for the elastic energy storage of a flexible backbone to obtain the true linearized relationship between actuator torques and end effector forces. When this energy storage is accounted for, accurate actuation-based wrench sensing is possible for multi-backbone continuum robots, as has been investigated in (163; 78; 164; 134) (termed "intrinsic wrench sensing" in those works). These works derive and validate a wrench-sensing algorithm for constant curvature manipulators via the principle of virtual work. For the general PCRs used in our research, we use a geometrically exact, nonlinear rod-mechanics model to accurately predict the tip force instead of a virtual-work framework under the constant-curvature assumption.

There has also been work in deflection-based force sensing with continuum robots (63) and catheters (165; 166). However, if the device is very stiff in one direction, this approach can become quite ill-conditioned, resulting in high estimation errors. We show that this is also true for PCRs. Our analysis also concludes that the sensitivity to sensing errors is greatly decreased for actuation-based force sensing when compared to deflection-based force sensing.

The model framework presented in Chapter 3 can be arranged in several forms, three of which can be used to sense forces at the tip of the manipulator. We compare the potential error propagation of these force sensing methods, including deflection-based force sensing, to arrive at the proposed method of actuation-based force sensing and provide results demonstrating a much lower error sensitivity. The sensing method takes 12 inputs of actuator positions (6) and actuator forces (6) to solve the static equilibrium and boundary condition equations for the entire manipulator and calculate the 6-DOF applied end-effector wrench.

Stiffness control of continuum robots is a small but growing area of research. The goal of a stiffness controller is to provide a command to the robot that incorporates the sensed tip force and changes the robot's active stiffness. The use of stiffness control with continuum robots takes advantage of their passive mechanical stiffness to increase their effectiveness in the medical application. Compliant motion control of a manipulator subject to forces along its axis during insertion through a small lumen has been investigated in (167). In (81), a concentric tube robot uses the controller to drive the actuation variables to a new desired value based on the force sensed at the tip of the manipulator using deflection based force sensing. Another example of of stiffness control with tendon driven robots can be seen in (168). In this research, a passive stiffness controller has been developed for the PCR using the modeling framework presented in Chapter 3. The controller is considered passive due to its limitation of only decreasing the stiffness of the PCR. The derivation and results of this work are presented in Chapter 5.2.

Chapter 3

General Kinematic Modeling for Flexible Manipulators

The ultimate goal of modeling a robotic manipulator is to control the joints in a way that provides accurate and dexterous motion of the end effector. A robot's model must be based on the physical parameters of its material and construction. This is especially true for continuum manipulators whose pose cannot be fully defined in a closed form solution by link lengths and joint angles (60). This chapter will review prior work in continuum robot modeling, detail the Cosserat rod equations and their use in modeling parallel continuum manipulators and concentric tube robots and outline the preliminary and proposed work on manipulator modeling in this dissertation.

For continuum manipulators, the equations defining the deformation of flexible structures are evaluated numerically and involve solving the statics or dynamics as opposed to the forward kinematics (72; 97; 67; 70). The barriers to control of continuum robots come from the limits of solving these models in real time. The Cosserat rod models used in parallel continuum manipulators and concentric tube robots have an advantage of simplification. Classical Cosserat rod models assume no cross-section deformation and gain a great amount of efficiency due to this simplification (e.g. two orders of magnitude in (169) for an extended Cosserat

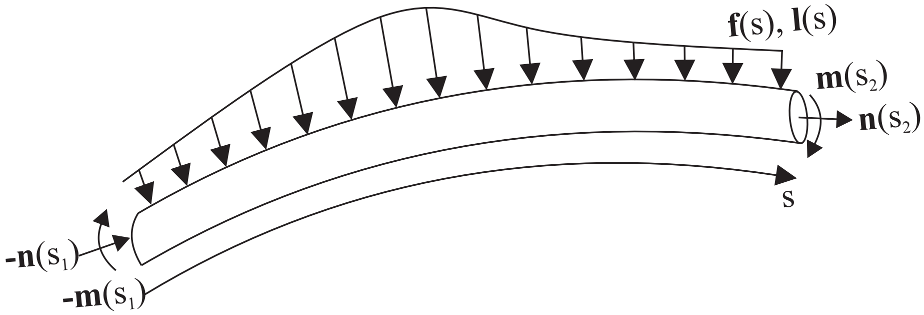

Figure 3.1: Arbitrary section of flexible link with the internal force and moment, $\mathbf{n}$ and $\mathbf{m}$, acting on the portion of the link. The distributed force and moment, $\mathbf{f}(s)$ and $\mathbf{l}(s)$, act along the entire arc length. These forces and moments are written in the global reference frame $\mathbf{g}(s)$.

model with cross-section inflation. Weak-form Cosserat rod models can be formulated and solved using a finite-element, finite-difference, or discrete-differential-geometry approach. Other systems use information related to the actuator length limits to create real-time implementations (88). With these techniques, real-time control of parallel continuum and concentric tube manipulators is possible (170; 46).

In order to establish a basis for the modeling of parallel continuum manipulators and concentric tube robots, we will review the Cosserat rod theory presented in (171) and then provide an overview of the modeling algorithms. We generalize the forward kinetostatics model that was previously presented as a minimal representation in (75). This model is more intuitive and unifies all problem formulations that we identify by only changing the known variables and utilizing the same system of equations. The new model framework also allows for the identification and efficient calculation of matrices that are applicable to any continuum manipulator or soft robot: the Jacobian, end-effector compliance, input stiffness, and wrench reflectivity matrices.

3.1 Cosserat Rod Equations

The robot is constructed of n flexible links in parallel. The shape of the ith link is defined by its position $\mathbf{p}_i(s_i) \in \mathbb{R}^3$ and material orientation in the form of an orthonormal rotation matrix, $\mathbf{R}_i\left(s_i\right) \in \mathrm{SO}(3)$, forming a material-attached reference frame,

$$\mathbf{g}_i\left(s_i\right) = \begin{bmatrix} \mathbf{R}_i\left(s_i\right) & \mathbf{p}_i\left(s_i\right) \\ \mathbf{0}^{\mathbf{T}} & 1 \end{bmatrix} \in \mathrm{SE}(3) \tag{3.1}$$

as a function of arc length $s_i \in [0 \;\; l_i]$. The position and orientation evolve along the length of the rod according to the linear, $\mathbf{v}_i(s) \in \mathbb{R}^3$, and angular, $\mathbf{u}_i(s) \in \mathbb{R}^3$, rates of change expressed in local or "body frame" coordinates of the material frame as follows:

$$\begin{aligned} \mathbf{p}_i' =& \mathbf{R}_i \mathbf{v}_i, \\ \mathbf{R}_i' =& \mathbf{R}_i \widehat{\mathbf{u}}_i, \end{aligned} \tag{3.2}$$

where $'$ denotes a derivative with respect to s_i, and $\widehat{}$ denotes mapping from $\mathbb{R}^3$ to $\mathfrak{so}(3)$ as follows:

$$\widehat{\boldsymbol{a}} = \begin{bmatrix} 0 & -a_3 & a_2 \\ a_3 & 0 & -a_1 \\ -a_2 & a_1 & 0 \end{bmatrix} \tag{3.3}$$

As in (172), we also use $^\vee$ to denote the inverse mapping of $\widehat{}$, i.e. $\left(\widehat{\mathbf{u}}\right)^\vee = \mathbf{u}$. The same symbol is overloaded to map a $\mathbb{R}^6$ to $\mathfrak{se}(3)$ as follows:

$$\widehat{\boldsymbol{a}} = \begin{bmatrix} 0 & -a_6 & a_5 & a_1 \\ a_6 & 0 & -a_4 & a_2 \\ -a_5 & a_4 & 0 & a_3 \\ 0 & 0 & 0 & 0 \end{bmatrix}. \tag{3.4}$$

Therefore, if one knows the body-frame $\mathbf{v}_i$ and $\mathbf{u}_i$ vectors and an initial frame $\mathbf{g}_i(0)$, the remaining frames can be obtained by integrating the differential equations in Equation (3.2). Since $\mathbf{v}_i$ and $\mathbf{u}_i$ are not constant with respect to s_i, numerical integration is required to obtain $\mathbf{g}_i$.

As derived in (171; 63; 67), the rates of change of the internal force vector $\mathbf{n}_i$ and internal moment vector $\mathbf{m}_i$ with respect to the arc length s_i are described by the classical Cosserat rod differential equations of static equilibrium. This is done by taking the derivative with respect to arc length of the static equilibrium balance shown in the free body diagram shown in Figure 3.1.

$$
\begin{aligned}
\mathbf{n}_i' &= -\,\mathbf{f}_i \\
\mathbf{m}_i' &= -\,\mathbf{p}_i' \times \mathbf{n}_i - \mathbf{l}_i,
\end{aligned}
\tag{3.5}
$$

where all vectors are expressed in global coordinates, and $\mathbf{f}_i$ and $\mathbf{l}_i$ are distributed force and moment vectors, respectively, applied per unit length to rod i. Distributed self-weight and any other external forces are straightforward to include within $\mathbf{f}_i$ and $\mathbf{l}_i$ (see Figure 3.1).

The kinematic variables $\mathbf{v}_i$ and $\mathbf{u}_i$ are related to the material strain (shear, extension, bending, and torsion) and can be used to calculate the internal force and moment vectors via a material constitutive law. The linear constitutive relationship used follows the form

$$
\begin{aligned}
\mathbf{n}_i &= \mathbf{R}_i\mathbf{K}_{se,i}\left(\mathbf{v}_i - \mathbf{v}_i^*\right), \quad \mathbf{K}_{se,i} = \begin{bmatrix} A_iG_i & 0 & 0 \\ 0 & A_iG_i & 0 \\ 0 & 0 & A_iE_i \end{bmatrix} \\
\mathbf{m}_i &= \mathbf{R}_i\mathbf{K}_{bt,i}\left(\mathbf{u}_i - \mathbf{u}_i^*\right), \quad \mathbf{K}_{bt,i} = \begin{bmatrix} E_iI_i & 0 & 0 \\ 0 & E_iI_i & 0 \\ 0 & 0 & J_iG_i \end{bmatrix}
\end{aligned}
\tag{3.6}
$$

and expresses $\mathbf{n}_i$ and $\mathbf{m}_i$ in global coordinates where $\mathbf{v}_i^*$ and $\mathbf{u}_i^*$ are the kinematic variables of the rod in an assigned stress free reference state. For an initially straight rod, the appropriate reference state variables are $\mathbf{v}_i^* = [0\ 0\ 1]^T$ and $\mathbf{u}_i^* = [0\ 0\ 0]^T$. The matrices $\mathbf{K}_{se,i}$ and $\mathbf{K}_{bt,i}$ contain the stiffness terms for a radially symmetric rod cross-section, which could vary with arc length, involving the area A_i, Young's modulus, E_i, shear modulus G_i, second area moment I_i (about the local x and y axes), and the polar area moment J_i about the local z axis.

Thus, for each rod, equations (3.2), (3.5), and (3.6) form a system of differential equations that describes the evolution of the state variables $\mathbf{p}_i$, $\mathbf{R}_i$, $\mathbf{n}_i$, and $\mathbf{m}_i$ with respect to s_i.

$$\begin{aligned}\mathbf{p}_i' =&\mathbf{R}_i\mathbf{v}_i, \quad \mathbf{v}_i = \mathbf{K}_{se,i}^{-1}\mathbf{R}_i^T\mathbf{n}_i + \mathbf{v}_i^* \\ \mathbf{R}_i' =&\mathbf{R}_i\widehat{\mathbf{u}}_i, \quad \mathbf{u}_i = \mathbf{K}_{bt,i}^{-1}\mathbf{R}_i^T\mathbf{m}_i + \mathbf{u}_i^* \\ \mathbf{n}_i' =& -\mathbf{f}_i \\ \mathbf{m}_i' =& -\mathbf{p}_i' \times \mathbf{n}_i - \mathbf{l}_i\end{aligned} \tag{3.7}$$

The above equations describe the shape and the internal forces and moments of the ith link. In the next section, we detail how the design of the distal end effector and the proximal base platform create geometric constraints. These constraints are enforced along with end-effector static equilibrium via a coupled set of boundary conditions that are simultaneously solved to obtain the configuration of the manipulator.

3.2 Distal Boundary Conditions

Regardless of the joint type, the following conditions of static equilibrium are enforced for the end effector:

$$\begin{aligned}&\sum_{i=1}^{n}\left[\mathbf{n}_i\left(l_i\right)\right] - \mathbf{F} = \mathbf{0} \\ &\sum_{i=1}^{n}\left[\mathbf{p}_i\left(l_i\right) \times \mathbf{n}_i\left(l_i\right) + \mathbf{m}_i\left(l_i\right)\right] - \mathbf{p}_e \times \mathbf{F} - \mathbf{M} = \mathbf{0},\end{aligned} \tag{3.8}$$

where $\mathbf{F}$ and $\mathbf{M}$ are external force and moment vectors, expressed in global coordinates and applied at the centroid of the end effector, $\mathbf{p}_e$. We combine the applied loads into a "wrench" vector $\mathbf{w} = [\mathbf{F}^T \;\; \mathbf{M}^T]^T$ for notational compactness. Also, the position of the distal end of the link is related to the center of the end effector via a constant vector $\boldsymbol{\rho}_i$ expressed in the end effector frame,

$$\mathbf{p}_e + \mathbf{R}_e\boldsymbol{\rho}_i - \mathbf{p}_i = \mathbf{0} \text{ for } i = 1...n. \tag{3.9}$$

The remaining distal boundary conditions govern the material orientation and moment of the links at $s_i = l_i$ based on the joint types which connect them to the end effector platform. We explain these rotation conditions below and summarize the entire set distal boundary conditions for each joint type in Table 3.1.

3.2.1 Fixed Joints

In the case of fixed joints (Table 3.1 “Fixed”), the orientation of the end effector platform frame, $\mathbf{R}_e$, and an orientation of each link at the tip, $\mathbf{R}_i\left(l_i\right)$, can be related by a pre-defined offset orientation, $\mathbf{R}_{\alpha_i}$ (dependent on the distal platform design). The design could utilize 3D printing construction to ensure that the links were fixed to the end effector platform at any desired orientation in the nominal configuration. The rotation between the end effector frame and the link frame can be defined as

$$\mathbf{R}_{\alpha_i} = \mathbf{R}_e^T \mathbf{R}_i(l_i), \tag{3.10}$$

where the matrix $\mathbf{R}_{\boldsymbol{\alpha}_i}$ is defined by $\boldsymbol{\alpha}_i \in \mathbb{R}^3$, containing angular displacements about the x, y, and z axes of the global frame. This rotation can be constructed via matrix exponential and the mapping in Equation (3),

$$\mathbf{R}_{\alpha_i} = e^{\widehat{\boldsymbol{\alpha}}_i} \tag{3.11}$$

This offset relationship can be written in a reduced form to be included in our solution method in the following way,

$$\left[\log\left(\mathbf{R}_i\left(l_i\right)^T \mathbf{R}_e \mathbf{R}_{\alpha_i}\right)\right]^\vee = \mathbf{0} \text{ for } i = 1...n, \tag{3.12}$$

where log() is the matrix natural logarithm, which maps SO(3) to $\mathfrak{so}(3)$ and the $^\vee$ operator subsequently maps $\mathfrak{so}(3)$ to $\mathbb{R}^3$. This form was chosen to express the angular error in the local $\mathbf{R}_i(l_i)$ frame, which facilitates a unified presentation of the torsionless

Table 3.1: Distal Boundary Conditions for Joint Types

Joint Type	Specified at $s_i = l_i$ for $i = 1 \ldots n$
Fixed	Equation (3.8) Equation (3.9) Equation (3.12)
Torsionless	Equation (3.8) Equation (3.9) $\mathbf{e}_3^T \mathbf{R}_e^T \mathbf{m}(l_i) = 0$ $\left(\log\left(\mathbf{R}_i^T \mathbf{R}_e \mathbf{R}_\alpha\right)\right)^\vee \Big\vert_{xy} = \mathbf{0}$
Spherical	Equation (3.8) Equation (3.9) $\mathbf{R}_e^T \mathbf{m}(l_i) = \mathbf{0}$

case we discuss below. The orientation of each link must equal the orientation of the end effector if $\mathbf{R}_{\alpha_i} = \mathbf{I}$.

3.2.2 Torsionless Joints

For a freely spinning joint, only the tangent vector of the link is fixed at $s_i = l_i$, and the link's rotation about its tangent vector is unconstrained. This implies the "natural boundary condition" that z component of the body frame moment, i.e. $\mathbf{e}_3^T \mathbf{R}_e^T \mathbf{m}(l_i)$ ($\mathbf{e}_3 = [0\ 0\ 1]$) must be zero. Therefore, only the x and y components of the distal constraints on the link rotation matrix in Equation (3.12) should only be applied. This is designated with the $|_{x,y}$ in Table 3.1 and is equivalent to multiplying by a truncated identity matrix which eliminates the third row. We note that if there are no distributed moments along the links and the links are straight in their unstressed reference states, a torsionless joint at the tip implies zero torsion everywhere along the

Table 3.2: Proximal Boundary Conditions

Configuration	Joint Type	Specified at $s_i = 0$	Unknown
No Base Plate	Fixed	$\mathbf{p}_i = \left[d_{ix}, d_{iy}, q_i\right]^T$ $\mathbf{R}_i = \mathbf{R}_z\left(\phi_i\right)$	$\mathbf{n}_i$ $\mathbf{m}_i$
No Base Plate	Torsionless	$\mathbf{p}_i = \left[d_{ix}, d_{iy}, q_i\right]^T$ $m_{iz} = 0$ $\mathbf{R}_i = \mathbf{R}_z\left(\phi_i\right)$	$\mathbf{n}_i$ m_{ix}, m_{iy} ϕ_i
No Base Plate	Spherical	$\mathbf{p}_i = \left[d_{ix}, d_{iy}, q_i\right]^T$ $\mathbf{m}_i = \mathbf{0}$, $\mathbf{R}_i\left(\boldsymbol{\theta}_i\right)$	$\mathbf{n}_i$ $\boldsymbol{\theta}_i$
Base Plate	Fixed	$\mathbf{p}_i = \mathbf{d}_i$ $\mathbf{R}_i = \mathbf{R}_z\left(\theta_i\right)$	$\mathbf{n}_i$ $\mathbf{m}_i$
Base Plate	Torsionless	$\mathbf{p}_i = \mathbf{d}_i$ $m_{iz} = 0$ $\mathbf{R}_i = \mathbf{R}_z\left(\phi_i\right)$	$\mathbf{n}_i$ $m_{ix,y}$ ϕ_i

link as a consequence of the differential equations defining the rod shape (Equation (3.7)). For the continuum Stewart Gough manipulator presented in this paper, torsionless joints are used for the simulations and experiments performed with the physical robot.

3.2.3 Spherical Joints

Having a spherical joint at the tip of each link implies the natural boundary condition of zero moment at the tip of each link, $\mathbf{R}_e^T\mathbf{m}(l_i) = \mathbf{0}$. The distal orientation of the links is now unknown and must be found.

3.3 Proximal Boundary Conditions

We formulate proximal boundary conditions for two types of robot designs: 1) robots with links passing through holes in a base plate between the actuators and the distal platform and 2) robots with links that are connected directly to the actuators and unconstrained along their full length (no base platform). We also consider 3 proximal joint types (fixed, torsionless, and spherical). This extends our prior work, where we considered designs with base plates and torsionless proximal joints. Our solution procedure (detailed in the next section) requires known conditions to be specified at a reference point on each link $s_i = 0$ and any unknown variables to be guessed. Table 3.2 details the specified and unknown proximal variables for the relevant joint types and base plate configurations. We note that the specified variables are functions of the actuator displacement q_i, fixed design parameters d_{ix} and d_{iy}, and some of the unknown variables at $s_i = 0$ as we describe in detail below. In both the base-plate and no-base-plate configurations (see Figure 3.2), the actuation variable, q_i, is defined as the z axis position of the base of the link in some fixed global reference frame.

3.3.1 No Base Plate Present

Without a base plate, $s_i = 0$ is designated where the link attaches to the actuator, and the length of integration is the entire length of the link, $l_i = L_i$. The position at $s_i = 0$ is specified by $\mathbf{d}_i$, which contains the actuation variable q_i as the global z position of each proximal link end, as shown in Figure 3.2 (a).

When connections are fixed, the base rotation of each link $\mathbf{R}_i(0)$ is a function of ϕ_i, a specified rotation about the z-axis, which could be a constant parameter or controlled as an additional input degree of freedom if rotational actuators were employed. The internal force and moment at $s_i = 0$ are guessed variables.

For a torsionless connections, $m_{iz}(0) = 0$, and the initial rotation is a function of an unknown rotation ϕ_i about the z axis. The internal force and the x and y components of $\mathbf{m}_i$ at $s_i = 0$ are guessed.

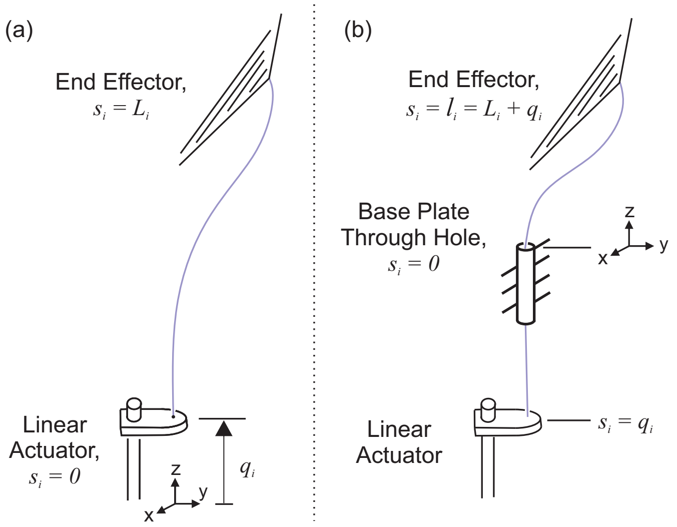

Figure 3.2: This figure shows the manipulator variables without and with a base plate in (a) and (b) respectively. The differences arise in the length of integration of the link and the definition of the arc length datum $s_i = 0$ for each link. The linear actuator controls the q_i which is equal to the initial position $p_z(0)$ of the link in the global frame. When a base plate is included, the linear actuator effectively changes the arc length l_i beyond the base plate. Without the base plate, the link arc length is constant, but the initial position of the link is changed.

In the case of spherical joints, $\mathbf{m}_i(0) = \mathbf{0}$ and the link has an unknown initial orientation, $\mathbf{R}_i(0)$, which can be parameterized by $\boldsymbol{\theta}_i(0) \in \mathbb{R}^3$, a vector of three angular displacements as

$$\mathbf{R}_i(0) = e^{\widehat{\boldsymbol{\theta}}_i}. \tag{3.13}$$

These rotations are guessed and used to construct $\mathbf{R}_i(0)$. The internal force at $s_i = 0$ is guessed.

3.3.2 Base Plate Present

With a base plate, we assume that the portion of the link between the actuator and the base plate is always straight. This is true as long as (1) this portion of the link is not precurved, (2) the tangent vector of the hole in the base plate is designed to pass through the actuator connection point, and (3) the axial compressive load is lower than the Euler critical buckling load for the current length of unsupported rod. We designate $s_i = 0$ at the base platform and integrate the differential equations from there to $s_i = l_i$, the length of the link between the base plate and the distal platform, which is a function of q_i,

$$l_i = L_i + q_i. \tag{3.14}$$

As shown in Figure 3.2, we have defined the global reference frame such that its $x - y$ plane is co-planar with the base platform, and thus each q_i is negative. With a base plate present and fixed joints, torsional deformation of each link between the actuator and the base plate should be considered. In this straight section, the Cosserat equations imply that the angular rate of change in the axial direction, $u_{iz} = \frac{m_{iz}}{J_i G_i}$, is constant. Therefore the angle of axial rotation, $\theta_{i,z}(s_i)$ varies linearly with arc length in this section. Under these assumptions, the initial condition $\theta_{i,z}(0)$ is a linear function of the actuation variable q_i, and the unknown torsional moment, m_{iz}, at $s_i = 0$:

$$\theta_{i,z}(0) = \phi_i - q_i \frac{m_{iz}(0)}{J_i G_i} \tag{3.15}$$

where ϕ_i is the initial axial rotation of the link at the point of attachment. The initial z axis rotation matrix for the link is then a function of $\theta_{i,z}$,

$$\mathbf{R}_i(0) = \mathbf{R}_z(\theta_{i,z}) = e^{\theta_{i,z}\widehat{\mathbf{e}}_3} \tag{3.16}$$

where $\mathbf{e}_3 = [0\ 0\ 1]^T$. In the case of fixed connections to the actuators, the proximal position of the links is specified with the vector $\mathbf{d}_i = [d_{ix}\ d_{iy}\ 0]^T$ and the internal force and moment are guessed. For torsionless connections at the actuators, $m_{iz}(0) = 0$ and $\mathbf{R}_i(0)$ is only a function of ϕ_i, which is a guessed variable along with the internal force and the x and y components of the internal moment.

3.4 Solution Method for Forward Kinematics

To lay groundwork for discussing the generalized problem formulations in the next subsection, we here detail our numerical solution procedure for the forward kinetostatics boundary value problem. The differential equations for the ith link (Equation (3.7)) have the form

$$\mathbf{y}_i' = f\left(\mathbf{y}_i, s_i\right) \tag{3.17}$$

where $\mathbf{y}_i = \{\mathbf{g}_i, \mathbf{n}_i, \mathbf{m}_i\}$ (see Equation (3.1) for definition of $\mathbf{g}_i$).

At the proximal end of the link ($s_i = 0$), the elements of each $\mathbf{y}_i$ are specified as functions of known or unknown proximal variables (see Table 3.2). At the distal end of the robot ($s_i = l_i$), the boundary conditions consist of six joint-specific geometric constraints for each distal link end (given in Table 3.1), and six static equilibrium equations for the entire end effector (given by Equation (3.8)), which involves the distal variables of all the rods. Thus, this set of 6n+6 distal boundary conditions effectively couple the individual rod models (3.7) together, and the entire coupled system must be solved simultaneously. We solve the coupled system via a shooting method which iteratively guesses the entire set of unknowns, integrates all rod initial value problems (3.7), and evaluates the entire set of coupled boundary conditions. The guess is updated based on the results of the boundary residual calculation until the set tolerance is satisfied. We describe the organization of this process in detail below for the forward kinetostatics problem, and adapt the same approach to solve the generalized problem formulations in the next section. The general process is depicted by an algorithmic flowchart in Figure 3.3.

The set of coupled distal boundary conditions (Table 3.1) can be organized into a single vector function of the form,

$$\mathbf{b}\left(\mathbf{g}_e, \mathbf{q}, \mathbf{w}, \boldsymbol{\tau}, \boldsymbol{\gamma}\right) = \mathbf{0} \tag{3.18}$$

where $\mathbf{q} = [q_1 \dots q_n]$ contains the actuator variables, $\mathbf{w} = [\mathbf{F}^T \ \mathbf{M}^T]^T$ is the external tip wrench, $\boldsymbol{\tau} = [-n_{i,z}(0) \cdots - n_{n,z}(0)]^T$ contains the actuator forces, all remaining unknown proximal variables are contained in $\boldsymbol{\gamma}$ (e.g., in the case of fixed joints at the proximal end with a base plate, $\boldsymbol{\gamma} = \begin{bmatrix} n_{1,x}(0) & n_{1,y}(0) & \mathbf{m}_1^T(0) \dots & n_{n,x}(0) & n_{n,y}(0) & \mathbf{m}_n^T(0) \end{bmatrix}^T$), and $\mathbf{g}_e$ is the (unknown) pose of the end effector,

$$\mathbf{g}_e = \begin{bmatrix} e^{\widehat{\boldsymbol{\varphi}}} & \mathbf{p}_e \\ \mathbf{0} & 1 \end{bmatrix} \tag{3.19}$$

with $\boldsymbol{\varphi} = [\varphi_x \ \varphi_y \ \varphi_z]^T$, $\mathbf{p}_e = [p_{ex} \ p_{ey} \ p_{ez}]^T$.

Note that while $\mathbf{q}$, $\boldsymbol{\tau}$, and $\boldsymbol{\gamma}$ do not explicitly appear in Table 3.1, $\mathbf{b}$ is implicitly dependent on them through the distal link variables. For any given guess of $\boldsymbol{\tau}$, $\boldsymbol{\gamma}$ and $\mathbf{g}_e$ and specification of $\mathbf{q}$ and $\mathbf{w}$, we can integrate the differential equations for each link from base to tip and subsequently evaluate the function $\mathbf{b}(\mathbf{g}_e, \mathbf{q}, \mathbf{w}, \boldsymbol{\tau}, \boldsymbol{\gamma})$, which we call the boundary condition residual. In prior work (75), we formulated the forward kinetostatics residual in a minimal way with only $6n$ equations that did not contain the unknown $\mathbf{g}_e$. By here introducing $\mathbf{g}_e$ as an extra 6-DOF unknown, the distal geometric constraints are written more intuitively in terms of $\mathbf{R}_e$ and $\mathbf{p}_e$ in Table 3.1. This new approach also unifies the generalized problem formulations in the next section by identifying a common set of equations that they all must solve. Note that in this form of the forward kinetostatics problem, (3.18) contains $6n + 6$ scalar equations, and the number of unknowns is also $6n + 6$ with $\boldsymbol{\gamma}$ containing $5n$ unknowns, $\boldsymbol{\tau}$ containing n unknowns and $\mathbf{g}_e$ containing 3 positions and 3 rotations as unknowns.

We use a shooting method to solve the system of equations in Table 3.1 for the specific manipulator design being modeled. The unknown proximal boundary conditions ($\boldsymbol{\gamma}$), the actuator forces ($\boldsymbol{\tau}$) and the end-effector pose ($\mathbf{g}_e$) are guessed. These guessed values along with the specified values are used to numerically integrated from $s_i = 0$ to l_i as an initial value problem using the `ode45` solver which is

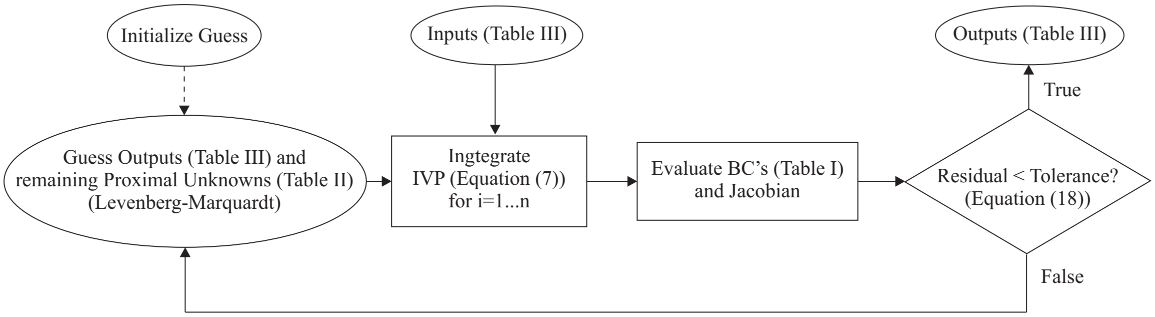
Initialize Guess
Inputs (Table III)
Outputs (Table III)
True
Guess Outputs (Table III) and remaining Proximal Unknowns (Table II) (Levenberg-Marquardt)
Ingtegrate IVP (Equation (7)) for i=1...n
Evaluate BC's (Table I) and Jacobian
Residual < Tolerance? (Equation (18))
False

Figure 3.3: Our shooting method for solving any general problem formulation is depicted in the flow chart shown above. The input variables are specified and the unknown and output variables are guessed.

implemented by the Dormand-Prince method, and the distal boundary condition equations are subsequently evaluated. This process is nested within an outer nonlinear-solver loop which iteratively updates the guessed values until the distal boundary conditions are satisfied within an appropriate tolerance. To update the guesses, we have used MATLAB's `fsolve()` function. This solver can be configured to implement several of algorithms, in this case we used the trust-region dogleg algorithm. In examining solutions for the rotation matrix, we have verified that orthonormality is maintained without implementing explicit numerical constraints. This is due to the high order numerical integration methods used, the short integration length, and low curvatures of the flexible links.

In (170) we described how this shooting method can be efficiently implemented in C++ to solve the inverse kinematics problem at rates greater than 4 kHz, thus enabling online control.

3.5 Generalized Problem Formulations

Equation 3.18 represents boundary conditions that must always be satisfied. Since $\mathbf{b}$ is written as a multi-variable function of $\mathbf{g}_e$, $\mathbf{q}$, $\mathbf{w}$, $\boldsymbol{\tau}$, and $\boldsymbol{\gamma}$, the outer nonlinear solver loop outlined in the previous section can be easily adapted to solve other general problem formulations (beyond forward kinetostatics) by merely assigning appropriate

Table 3.3: Kinetostatic Model Formulations

Formulation	Number of Unknowns	Number of Equations
$\{\mathbf{g}_e, \boldsymbol{\tau}\} = \mathrm{F}_{q,w}(\mathbf{q}, \mathbf{w})$	$6n+6$	$6n+6$
$\{\mathbf{g}_e, \mathbf{q}\} = \mathrm{F}_{\tau,w}(\boldsymbol{\tau}, \mathbf{w})$	$6n+6$	
$\{\mathbf{q}, \boldsymbol{\tau}\} = \mathrm{F}_{g,w}(\mathbf{g}_e, \mathbf{w})$	$7n$	
$\{\boldsymbol{\tau}, \mathbf{w}\} = \mathrm{F}_{g,q}(\mathbf{g}_e, \mathbf{q})$	$6n+6$	
$\{\mathbf{q}, \mathbf{w}\} = \mathrm{F}_{g,\tau}(\mathbf{g}_e, \boldsymbol{\tau})$	$6n+6$	
$\{\mathbf{g}_e, \mathbf{w}\} = \mathrm{F}_{q,\tau}(\mathbf{q}, \boldsymbol{\tau})$	$5n+12$	

sets of known and unknown (iteratively guessed) variables. For example, if we want to know the $\mathbf{q}$ and $\boldsymbol{\tau}$ required to achieve a specified $\mathbf{g}_e$ under a known constant load $\mathbf{w}$ (which could be considered an inverse kinetostatics problem), the integration procedure remains the same, but the nonlinear solver must iteratively guess the unknowns $\mathbf{q}$ and $\boldsymbol{\tau}$, and evaluate $\mathbf{b}$ with the specified $\mathbf{g}_e$ and $\mathbf{w}$. In general, any combination of variables out of the set $\{\mathbf{g}_e, \mathbf{q}, \mathbf{w}, \boldsymbol{\tau}\}$ can be selected as knowns with the remaining variables as unknowns, as long as the number of unknowns matches the number of equations in $\mathbf{b}$. Figure 3.3 summarizes the process in general, and we describe several useful cases below.

Table 3.3 shows several possible kinetostatic problem formulations and their inputs and outputs (knowns and unknowns) along with their respective number of unknowns which can be compared to the number of equations which is a constant $6n + 6$. We briefly discussed the inverse kinetostatics problem formulation above, and this is labeled $\mathrm{F}_{g,w}$ in the table. Three of the problem formulations contain the external wrench as an output. Thus these could potentially be used to estimate the wrench at the tip of the manipulator, given various known or sensed quantities. The formulation using inputs of $\mathbf{g}_e$ and $\mathbf{q}$ is essentially the deflection-based wrench sensing explored using a probabilistic framework in (63). The $\mathrm{F}_{g,\tau}$ formulation is also a deflection-based sensing formulation since it has $\mathbf{g}_e$ as an input. The $\mathrm{F}_{q,\tau}$ is perhaps the most convenient wrench sensing formulation since the actuation variables and forces are easily accessible through sensors mounted at the actuators themselves. We call the $\mathrm{F}_{q,\tau}$ formulation "actuation-based wrench sensing". This idea has been previously termed "intrinsic wrench sensing" in (163) which used a constant-curvature model framework in contrast to our general Cosserat-rod approach. We evaluate our approach experimentally for PCR's in Section 5, and we analytically show that for our prototype PCR design, actuation-based sensing is less sensitive to measurement errors than either deflection-based approach.

We note that the $\mathrm{F}_{g,w}$ formulation (inverse kinetostatics) is under constrained for $n > 6$ (which can be addressed by incorporating some method for redundancy resolution), and over constrained for $n < 6$ (which can be resolved by reducing in the dimension of the pose specification). For example, we should consider the number of desired operational degrees of freedom versus the number of actuator inputs (n). If a 6-DOF robot is used for only position control, the $F_{g,w}$, $F_{g,q}$, and $F_{g,\tau}$ algorithms will be underdetermined, and a method for redundancy resolution should be incorporated. Similarly, the actuation-based sensing formulation is over constrained if $n > 6$ (which could be resolved by a least-squares solution or a probabilistic approach) and under constrained for $n < 6$ (which could be resolved by reducing the dimension of sensed wrench components, e.g., assuming some components are zero).

3.6 Stacked Parallel Continuum Manipulator

Building on the modeling previously described, the capabilities of the parallel continuum manipulator model are expanded to include multiple stacked modules. This will provide increased dexterity and workspace pass the 6 DOF space that is currently achievable by a single unit.

Following a similar format to the concentric tube manipulator designs (46; 60), parallel continuum robots can potentially be stacked in a similar fashion where the proximal sections are tubes and the most distal section is compose of flexible rods. A version of this manipulator was prototyped by a senior design team at the Worcester

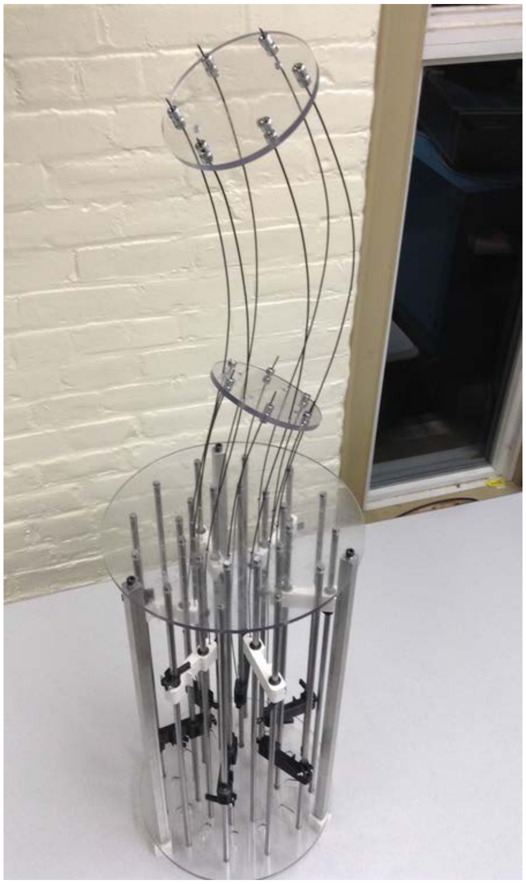

Figure 3.4: Example of a stacked parallel continuum robot (173).

Polytechnic Institute (173) (see Figure 3.4). However, this design consisted of two separate rod pathways with one set terminating at the middle section and the second set terminating at the end effector. The modeling for this manipulator was a simple stacking of the PCR model in (75) and does not accurately reflect the kinematics of the manipulator.

In order to model the kinematics of a stacked PCR with an outer concentric tube and an inner rod, a second set of static equilibrium equations must be enforced along with additional constraints on the geometry of the middle section.

3.6.1 Additional Unknowns, Constraints and Equations

In a single parallel continuum manipulator with 6 rods, the forward kinematics has 42 unknown variables (pose, internal force and moment). For a stacked model with two sections of six rods, the number of unknown variables doubles. The equations and constraints can be organized into those pertaining to the outer tube and the inner rod.

The outer tube has the same initial conditions as a single module of a PCR with the pose and rotation of each rod at the base (in a fixed case) or some portion of the internal moment (torsionless or spherical case) known. The Young's modulus and shear modulus are doubled. The tubes are integrated with the same equations stated in 3.7.

The inner rods can be modeled with an initial pose matching the distal end of the outer tubes. The integration of these rods is from the distal end position of the outer tubes to the end effector.

An additional equilibrium equation can be written for the middle plate. This equation sums the forces and moments on the plate

$$\begin{aligned} \sum_{i=1}^{n}[\mathbf{n}_{t,i}(L_i)] - [\mathbf{n}_{r,i}(0)] &= \mathbf{0} \\ \sum_{i=1}^{n}[\mathbf{m}_{t,i}(L_i)] - [\mathbf{m}_{r,i}(0)] &= \mathbf{0} \end{aligned} \tag{3.20}$$

where n_t is the internal force of the outer tubes and n_r is the internal force of the inner rods. The equilibrium equation for the end plate is similar to the single section except it only involves the inner rods.

$$\begin{aligned} &\sum_{i=1}^{n}[\mathbf{n}_{r,i}(L_i)] - \mathbf{F} = \mathbf{0} \\ &\sum_{i=1}^{n}[\mathbf{p}_{r,i}(L_i) \times \mathbf{n}_{r,i}(L_i) + \mathbf{m}_{r,i}(L_i)] - \mathbf{p}_e \times \mathbf{F} - \mathbf{M} = \mathbf{0}, \end{aligned} \tag{3.21}$$

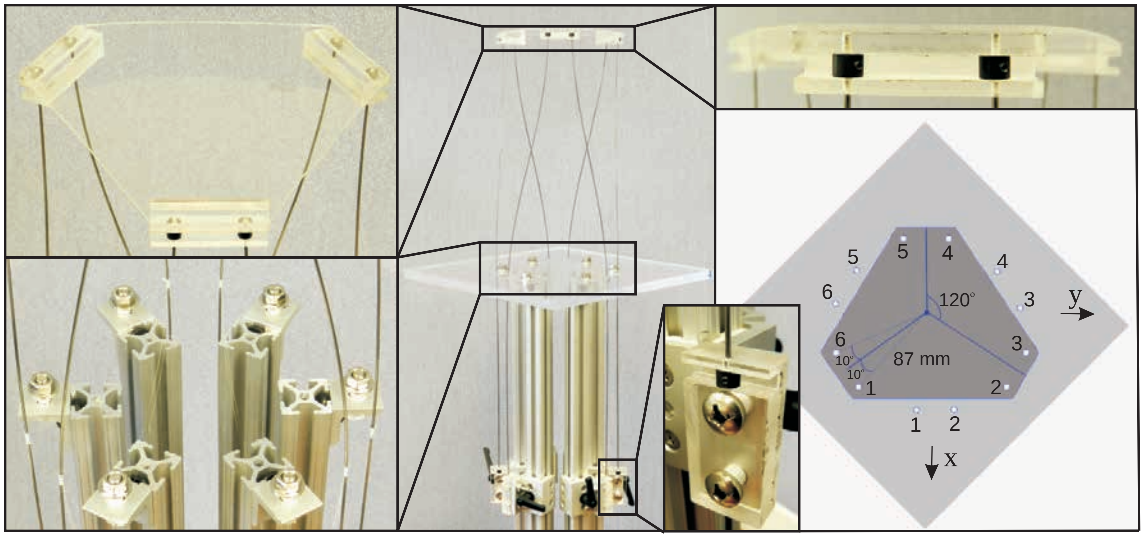

Figure 3.5: The middle picture shows our prototype parallel continuum manipulator constructed for initial proof of concept and evaluation of our modeling approach. Close-up views of the base and end platforms are shown to the left. The dimensions and patterns of the base plate pass-through holes and the top platform connection points are detailed to the right. The lengths of the compliant legs between the two platforms are actuated by manually translating linear slides connected to the rod ends below the base platform.

3.7 Qualitative Model Validation

There have been several model validations completed for the PCR modeling described above. The first is presented in (75) and comprises of a qualitative validation between model predicted configuration plots and photos of the physical system. The second validation was with a smaller system and used a 3D pose recording system to validate the model quantitatively. A third validation of the model is presented in Chapter 5 with the force sensing.

3.7.1 Prototype Design and Construction

In this section we describe the construction of a parallel continuum manipulator prototype structure designed to show proof-of-concept and study parallel continuum robot behavior. The prototype has six compliant legs connected in a similar arrangement to the legs of a 6-DOF rigid-link Stewart-Gough platform, and each leg can be manually actuated. The legs consist of 1.3 mm diameter spring steel music wire (ASTM A228) with an estimated Young's modulus of 207 GPa and Poisson's ratio of 0.305. As shown in Figure 3.5, these rods are connected to an end-effector plate of clear 1/16 inch acrylic via 3/8 inch OD shaft collars constrained in channels within small blocks attached to the plate. The rods are routed through holes in the base plate, and the proximal ends are connected to linear slide carriages in the same fashion. The carriages translate along T-slotted aluminum rails (80/20® Inc.) that are bolted in a hexagonal pattern to the base plate. The linear slide carriages can be manually repositioned and locked in place with a brake so that the length of each rod between the base plate and the end plate can be actuated independently.

The connection locations of the 6 flexible legs are arranged in a conventional radial hexapod pattern of 3 pairs of rods spaced 120° apart at a radius of 87 mm. As depicted by the numbers in Figure 3.5, the proximal holes for rods 1 and 2 are paired together (with a total separation of 20°), while at the end plate the connections for rods 2 and 3 are paired together. The same pattern follows for the other pairs of wires. Rods 3 and 4, and 5 and 6 are paired at the base plate, while 4 and 5, and 6 and 1 are paired at the distal end. In the nominal configuration shown in Figure 3.6 with all leg lengths equal, this connection pattern causes the top plate to be rotated by 60° with respect to the hole pattern in the base plate and causes all of the rods to bend from their naturally straight state.

3.7.2 Kinematic Simulation and Analysis

Figure 3.6 demonstrates the kinematic degrees of freedom and range of motion of our prototype manipulator structure by showing the manipulator shape in five different configurations. With all leg lengths equal, the robot is in a straight, nominal state, which can be raised or lowered by equal translation of the legs. By extending legs 2, 4, and 6, the distal platform twists about the z-axis. Translating legs 4 and 5 causes

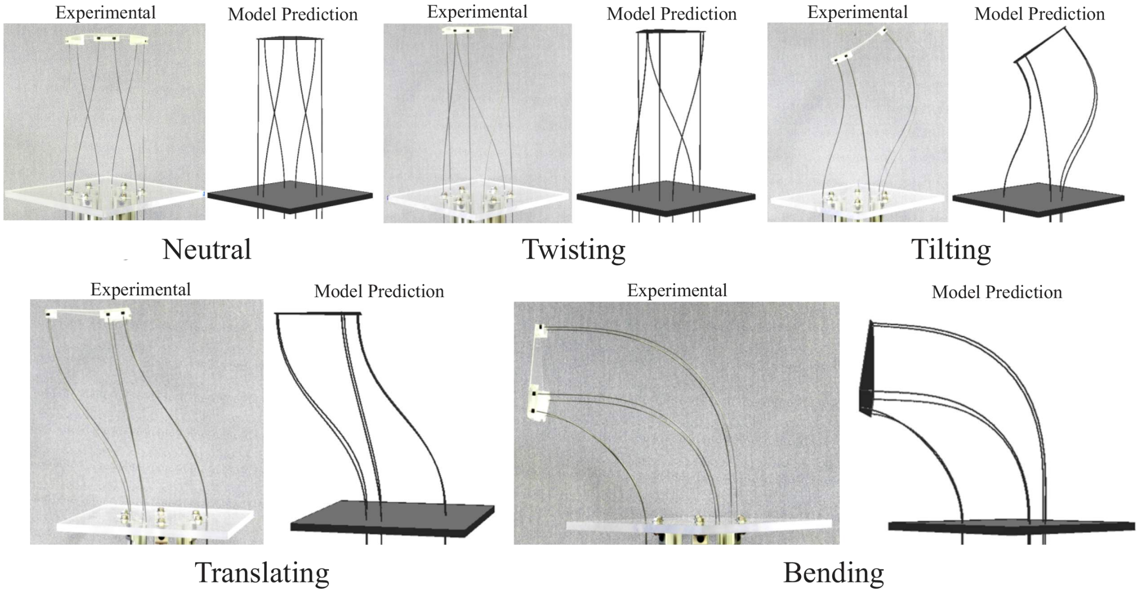
Experimental
Model Prediction
Experimental
Model Prediction
Experimental
Model Prediction
Neutral
Twisting
Tilting
Experimental
Model Prediction
Experimental
Model Prediction
Translating
Bending

Figure 3.6: We show photographs of five experimental configurations, demonstrating the ability of our prototype parallel continuum manipulator to execute axial twist, transverse tilt, translation, and bending (simultaneous translation and tilt). To the right of each experimental photograph, we show a MATLAB rendering of our rod-mechanics-based kinematic model prediction for the same actuator configurations.

the platform to tilt, and translating legs 3 and 6 causes translation. A combination of rotation and translation (bending) is achieved by extending legs 4 and 5 while retracting legs 1 and 2. The collection of legs maintains a compact form throughout all these motions, which is encouraging for potential applications in confined spaces. Figure 3.6 also shows a rendering of our forward kinematics model solution for these five cases, indicating the feasibility and qualitative accuracy of the modeling approach over a wide range of motion. We provide further quantitative assessment of model accuracy in Section 3.7.3.

To further illustrate the kinematics of the prototype design, we give the body-frame manipulator Jacobian, **J** as defined in (172), which we computed numerically for the prototype manipulator in the nominal configuration (where all leg lengths are

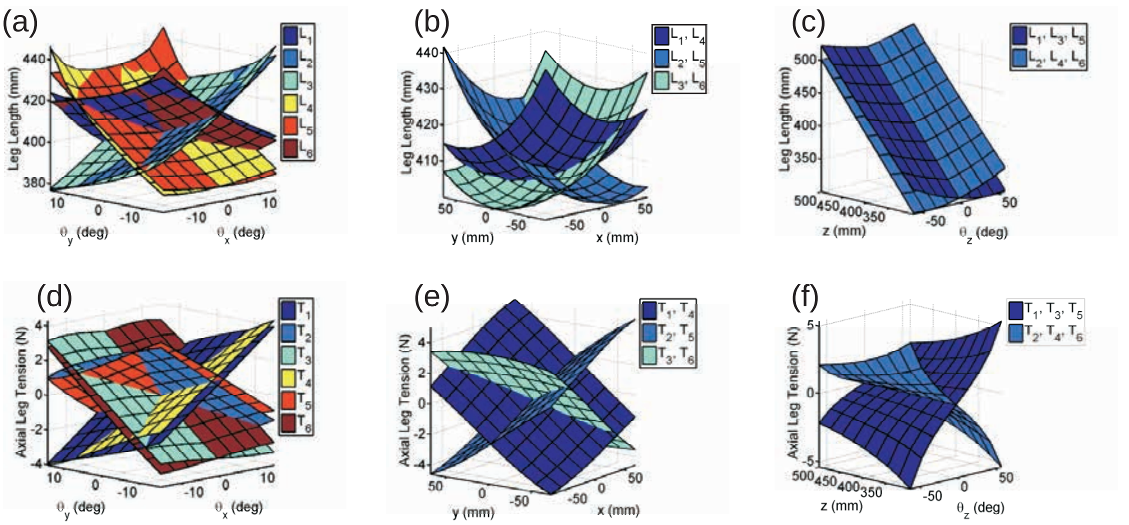

Figure 3.7: By solving the inverse formulation of the model equations (inputs of pose and wrench and outputs of actuation variables and actuation forces) in Section 3.5, we explore three two-dimensional slices of the workspace for our prototype design described in Section 3.7.1, centered about a nominal workspace point $\mathbf{p}_d = [0 \;\; 0 \;\; 400 \text{ mm}]^T$, $R_d = I$.

406 mm, and the rotation is aligned with the global reference frame.),

$$\mathbf{J} = \begin{bmatrix} -1.62 & -1.62 & 1.83 & -0.21 & -0.21 & 1.83 \\ -1.18 & 1.18 & -0.82 & -2.00 & 2.00 & 0.82 \\ 0.17 & 0.17 & 0.17 & 0.17 & 0.17 & 0.17 \\ -0.12 & 0.12 & 0.24 & 0.12 & -0.12 & -0.24 \\ -0.20 & -0.20 & 0.00 & 0.20 & 0.20 & 0.00 \\ -0.65 & 0.65 & -0.65 & 0.65 & -0.65 & 0.65 \end{bmatrix},$$

where the top 3 rows are dimensionless, and the bottom three rows have units of degrees/mm. The matrix is full rank and well conditioned, indicating that in the nominal configuration, actuators can easily move the top platform in any direction in the 6 DOF space of rigid body motion.

In Figure 3.7, we depict the inverse kinematic mapping over 3 two-dimensional slices of the workspace. The figure shows the required leg length and axial tension at the base of each leg as a function of the desired end-effector pose, which is specified by position $\mathbf{p}_d = [x \; y \; z]^T$ and orientation $R_d = \exp(\widehat{\boldsymbol{\theta}})$, $\boldsymbol{\theta} = [\theta_x \; \theta_y \; \theta_z]^T$. For each slice, two of the six pose variables were varied over a 9x9 grid of values for which the inverse kinematics computation easily converged, while all other pose variables were held constant at their nominal values of $x = y = \theta_x = \theta_y = \theta_z = 0$, and $z = 400$ mm. In (a) and (d), the required leg lengths (a) and axial tension at the base of each leg (d) are plotted as a function of desired angular displacements of the distal platform about the global x and y axes while holding the desired position constant. In (b) and (e), the required leg lengths (b) and axial tension at the base of each leg (e) are plotted as a function of desired displacements in the global x and y directions while holding the desired orientation constant. In (c) and (f), the required leg lengths (c) and axial tension at the base of each leg (f) are plotted as a function of desired displacement along and rotation about the global z axis while holding all other pose variables constant.

The first case (Figure 3.7: (a) and (d)) shows an approximately linear kinematic mapping for desired rotation about the x and y axes. The second case (Figure 3.7: (b) and (e)) shows an approximately quadratic leg length mapping and an approximately linear tension mapping for desired translation in the $x-y$ plane. We note that in this case, the required lengths and tensions are identical for legs 1 and 4, 2 and 5, and 3 and 6 respectively. The final case (Figure 3.7: (c) and (f)) shows an approximately linear leg length mapping and an approximately cubic tension mapping for desired motion which both rotates about and translates along the global z axis. In this case, the lengths and tensions are identical for legs 1, 3, and 5, and 2, 4, and 6 respectively.

The axial tension at the base of each leg corresponds to the actuator force which would be required to hold the robot in a particular configuration. We conclude that over these ranges of motion, moderate forces on the order of 5 N will be required to actuate the structure. A simulation of this kind can be used in the design process to size motors for a particular set of manipulator structural parameters, and to limit the length that the legs extend below the base platform to avoid buckling.

We can also compute the output stiffness matrix at the top platform, which maps displacement of the end effector centroid to applied force $d\boldsymbol{F} = Kd\boldsymbol{p_c}$. For the

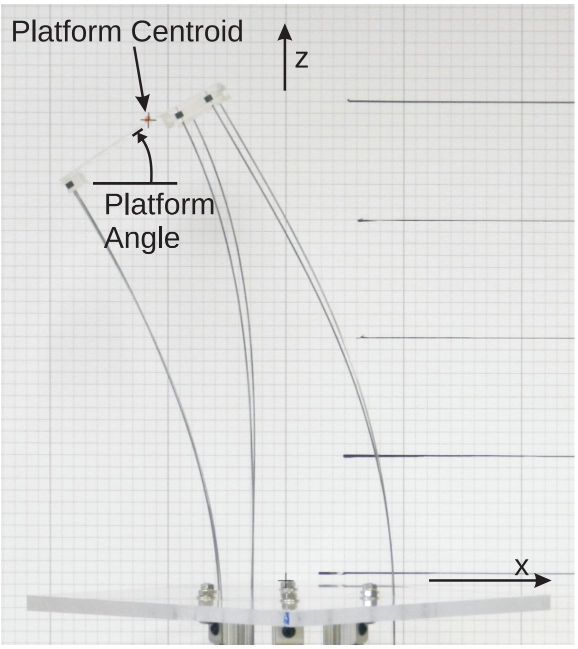

Figure 3.8: The three main measurements taken from the images are the position of the centroid of the end effector plate in the x and z, which is denoted by the marker at the top, and the orientation of the end effector in the $x-z$ plane. The orientation was measured by drawing a line along the end effector edge and then measuring the slope of the line with the grid poster.

nominal configuration in Figure 3.6, the computed stiffness matrix is

$$K = \begin{bmatrix} 17 & 0 & 0 \\ 0 & 17 & 0 \\ 0 & 0 & 122 \end{bmatrix} N/mm,$$

while for the bending configuration in Figure 3.6, the stiffness matrix is computed to be

$$K = \begin{bmatrix} 12.7 & 0 & 12.8 \\ 0 & 0.5 & 0 \\ 12.8 & 0 & 14.5 \end{bmatrix} N/mm.$$

These computations show that the stiffness in the y direction (out of the page for the bending case in Figure 3.6), is only about 3% of its value in the straight case, which is consistent with our experience with this prototype. We conclude that care should be taken when designing and controlling a parallel continuum manipulator to ensure that output stiffness is sufficient for the desired tasks.

Table 3.4: Experimental Configurations and Model Error (mm)

#	L_1	L_2	L_3	L_4	L_5	L_6	Error	% Error
1	406	406	406	406	406	406	3.4	0.8
2	386	406	386	406	386	406	6.1	1.6
3	426	406	426	406	426	406	2.9	0.7
4	406	406	426	406	406	426	8.8	2.1
5	406	406	386	406	406	386	7.1	1.8
6	406	406	366	406	406	366	5.4	1.4
7	406	406	406	386	386	406	7.5	1.8
8	406	406	406	366	366	406	10.4	2.7
9	406	406	406	426	426	406	8.9	2.1
10	406	406	406	446	446	406	7.6	1.8
11	426	426	406	386	386	406	7.0	1.7
12	446	446	406	366	366	406	10.4	2.6
13	386	386	406	426	426	406	9.3	2.3
14	366	366	406	446	446	406	11.7	2.9

3.7.3 Experimental Validation

We performed a set of model validation experiments by photographing the shape of our prototype manipulator in front of a graph poster in 14 different actuator configurations, which are listed in Table 3.4. Figure 3.8 shows the basic elements of each image that were measured, the top platform centroid and orientation in the global $x{-}z$ plane. These measurements were then compared to our forward kinematics model prediction for each actuator configuration. The photos of these planar cases were taken perpendicular to the graph plane approximately 30 feet away from the robot so that perspective error was minimized.

The resulting differences between the data and the model prediction are presented in Table 3.4. The positional error was calculated as the total Cartesian error in the global $x - z$ plane, and the percent error was calculated as the position error divided by the average leg length for each case. The maximum positional error was 11.74 mm with a 2.89% associated percent error. For the configurations resulting in a change in top platform orientation (7-14 in Table 3.4), angular displacement was measured

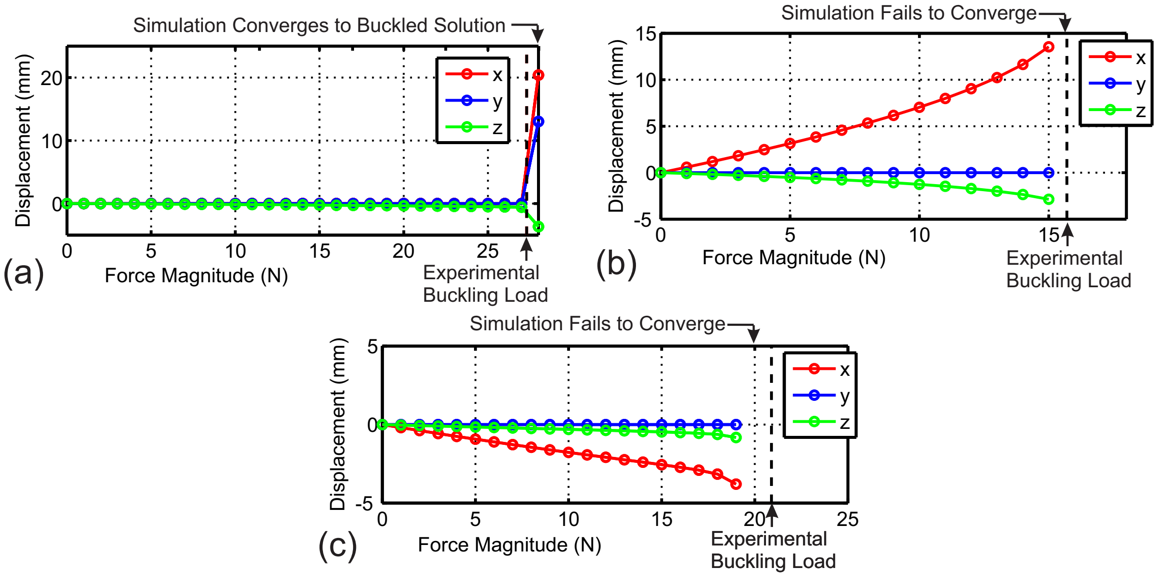

Figure 3.9: Displacements of the top platform centroid in the x, y, and z directions are plotted by using our forward kinematics model to perform quasistatic simulation with an incrementally increasing vertical load for three different manipulator configurations (1, 4, and 5 in Table 3.4) . The black dashed lines depict the experimentally determined critical buckling loads for the same cases.

graphically as shown in Figure 3.8, and the maximum angular difference between model prediction and experiment was 3.14 degrees.

We observed a small amount of flex in the top acrylic plate during the experiments. This unmodeled effect is a source of error between model prediction and actual manipulator shape. Future designs should mitigate this inaccuracy by designing the top plate thickness to better handle the expected reaction moments which can be determined using the model.

3.7.4 Buckling Experiments

We also experimentally determined a critical buckling load for the prototype structure in three different actuator configurations, (1, 4, and 5 in Table I, corresponding to a straight nominal case and two translating cases, respectively). We applied an incrementally increasing force in the negative z direction (down) through the centroid of the top plate until at least one leg in the structure began to buckle.

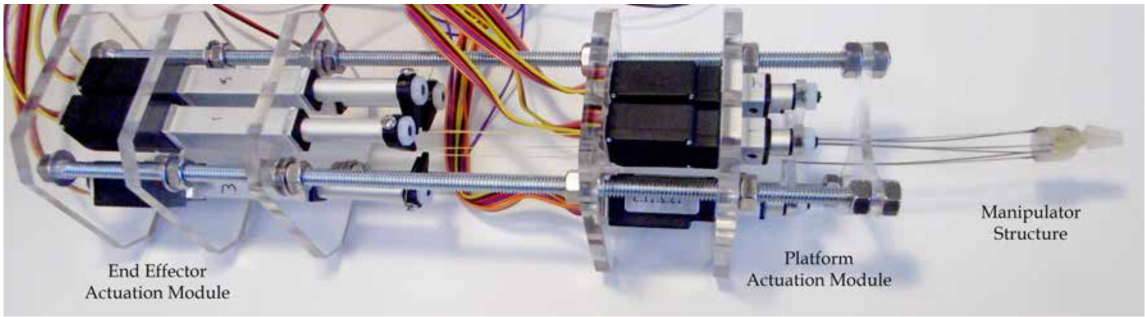

Figure 3.10: The surgical gripper system consists of the manipulator structure (right), platform actuation module (middle) and an end effector actuation module (left). The manipulator structure includes six flexible tubes connected in a conventional Stewart-Gough platform configuration. The platform actuation module uses six linear actuators to translate each leg. The end effector actuation module uses four linear actuators to control the grasper jaws via Kevlar threads that pass through the manipulator's tube legs.

The resulting experimental buckling loads are shown by the black dashed lines in Figure 3.9. When running a forward kinematics model simulation with the same incrementally increasing force, our simulation converged to a buckled solution (shown by the sudden large centroid displacement in Figure 3.9 (a)) at a load close to the experimentally determined buckling load. For configurations 4 and 5 ((b) and (c) in Figure 3.9), the simulation failed to converge to a valid forward kinematics solution just prior to reaching the experimentally determined buckling load, indicating that the buckled mode is not relatively close to the unbuckled state.

Since the publication of this paper, we have identified a more accurate method of detecting buckling in (174).

3.8 Validation of PCR with Gripper

3.8.1 Design and Fabrication

In this section, we give a condensed description of the robotic system design previously presented in (128) to provide context for the mechatronic control description in Section 3.8.2, and the analysis and validation in Sections 3.8.3 and 3.8.4.

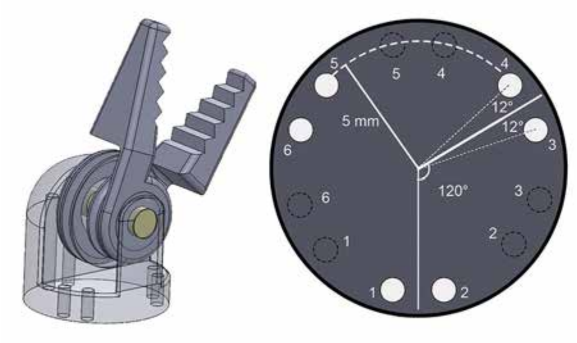

Figure 3.11: The grasper consists of two jaws, each of which is actuated by a capstan pulley and a Kevlar thread passing through the tube legs of the manipulator structure.

Manipulator Structure

The manipulator structure consists of a grasper assembly and six superelastic NiTi (Nitinol) tubes (legs) with their distal ends fixed to holes in the base of the end effector with J-B Weld 8265S epoxy. The tubes have an outer diameter of 0.597 mm and an inner diameter of 0.495 mm and are arranged in three pairs with their centers located on a 10 mm diameter circle, as shown in Fig. 3.11. The pairs are spaced 120° apart, with 24° of separation between paired tubes. The proximal ends of the tubes pass freely through six holes in a fixed platform (made from 0.125 inch [3.175 mm], laser cut acrylic) at the base of the manipulator structure. The hole pattern in the base platform is the same as the hole pattern at the end effector, rotated by 60°, and has the leg pairings shifted such that the robot resembles a classic 6-DOF Stewart-Gough platform, as shown by the numbering in Fig. 3.11. The nominal length from base to end-effector is 42 mm when the robot is in its neutral home configuration (all leg lengths equal). Axial translation of tube bases by linear actuators behind the base platform deforms the compliant legs and changes the pose of the end effector.

Platform Actuation Module

The platform actuation module, shown in Fig. 3.12a, contains six L12 miniature linear actuators from Firgelli Technologies Inc. These actuators have a 10 mm stroke length, a positional accuracy specification of 0.1 mm, and include an internal feedback

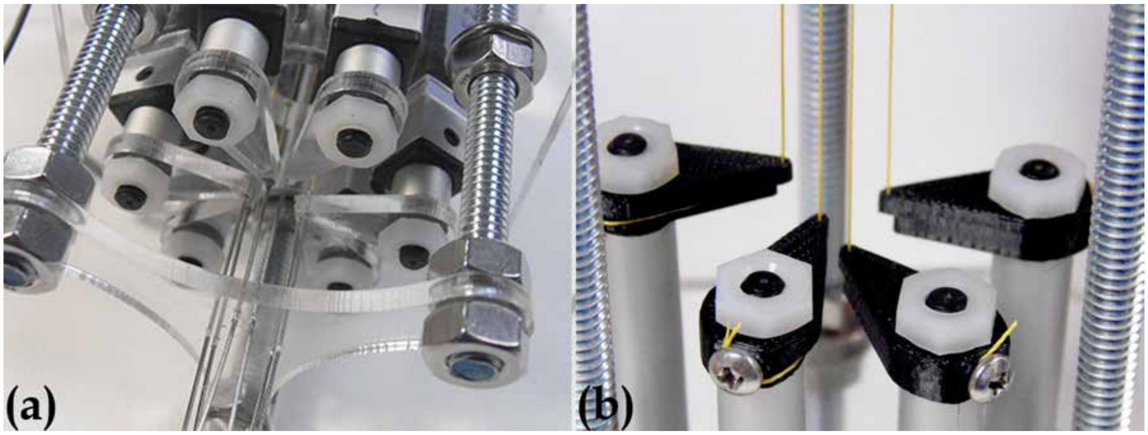

Figure 3.12: Two sets of custom tabs act as mechanical interfaces to the actuators. (a) The first set of tabs connects to the tube legs of the manipulator structure. (b) The second set of tabs holds the Kevlar cables that actuate the end effector.

potentiometer, which allows for closed-loop position control of each actuator. Analysis of the robot Jacobian reveals that high actuator resolution is necessary to accurately control this manipulator in certain directions. For example, actuator translations (or errors) of only 0.1 mm produce a 10° axial rotation of the end effector.

End Effector Actuation Module

The end effector actuation module contains four Firgelli L12 miniature linear actuators for controlling the grasper's actuation cables. These actuators differ from the platform actuators in that their stroke is 50 mm and the positional accuracy is 0.2 mm. The actuation cables for the end effector are connected to these actuators with four 3D printed tabs, shown in Fig. 3.12b.

2-DOF Cable Driven End Effector

The grasper assembly, shown in Fig. 3.11, is 12 mm in diameter and consists of a housing structure and two jaws. A capstan pulley on each jaw is oriented such that the sheave is tangent to the through holes in the base of the end effector, which allows for an actuation cable to be passed through a tube leg in the manipulator structure and around the capstan pulley. The cable then passes back through a second tube

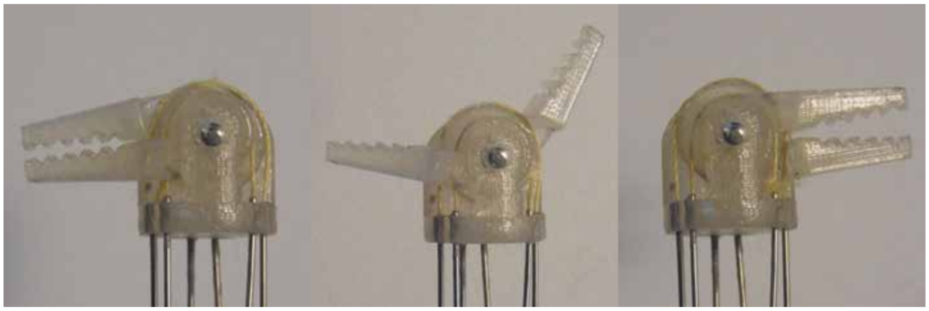

Figure 3.13: With a diameter of 12 mm, our gripper design extends the dexterous workspace of the manipulator by allowing 180° of independent motion of each jaw of the end effector.

leg. This assembly is repeated for a second actuation cable, so a total of four tube legs are used to guide the grasper actuation cables to the end effector. Kevlar thread was chosen for the cables because of its high tensile strength and resistance to bending fatigue compared to stainless steel rope, making it ideal for small diameter capstan pulleys. All of the components for the prototype end effector, with the exception of a steel dowel pin shaft, were fabricated with PLA plastic using a Replicator 2 Desktop 3D printer from Makerbot Industries. These components could also feasibly be machined from higher-strength materials using CNC micro-machining techniques. As shown in Fig. 3.13, each jaw of the grasper has 180° of independent motion. These additional DOF significantly increase the dexterous workspace of the manipulator, facilitating use in endoscopic procedures.

3.8.2 Control Architecture

The system's control hardware includes an Arduino Mega 2560 microcontroller, three Adafruit Motorshield kits (Adafruit Industries), a Windows PC running 64-bit MATLAB, and an Xbox controller (Microsoft Corp.) for user input during teleoperation. The highest level loop is coded in MATLAB and is used for solving the inverse kinematics, commanding and recording actuator positions, plotting simulations, and communicating with input devices. The manipulator kinematics are computationally expensive, so the kinematics are coded in C++ and compiled as a Matlab Executable (MEX) function. Using the efficient computation method from our previous work (170), the inverse kinematics solutions can be computed at several kilohertz, but due to the Arduino's processor speed, the serial communication is synchronized at 25 Hz. A custom Arduino script manages the low-level motor control of the linear actuators using a proportional-plus-integral (PI) controller and feedback from the linear actuators' internal potentiometers.

When not actuating the end-effector jaws, each linear actuator in the end effector actuation module must keep the cable length above the fixed platform constantly equal to the tube leg through which it runs. This is to maintain cable tension and ensure that the jaw angles do not change with the motion of the manipulator. So, for any change in position for a particular tube leg, the end effector actuator paired with that leg must move the cable an equal distance to compensate. When actuation of a grasper jaw is desired, the two linear actuators controlling the actuation cable move in opposing directions to change the jaw angle while maintaining cable tension. This control scheme allows for simultaneous control of the jaw angles and the 6-DOF end-effector pose.

The Kevlar thread diameter and the pulley diameters are difficult to accurately measure, so the end effector actuation motors required calibration. Diameter estimates were calculated iteratively to minimize the error between the desired and the measured jaw angles.

The teleoperation interface integrated with this robot is unilateral and employs velocity commands as inputs. The user interface is a Microsoft Xbox controller, which has six buttons that are each mapped to a specific positional or rotational DOF of the end effector. The scaling of each input can be adjusted according to user preference. We restrict the workspace of the manipulator to poses for which the bending strain in any tube does not exceed 2.5% (as further discussed in Section 3.8.3). If the maximum strain for a particular pose exceeds the strain limit, that pose is not commanded. Virtual limits imposed on the end-effector actuation commands furthermore prevent the grasper's jaws from colliding.

A 6-DOF Geomagic Touch input device was also successfully integrated with this system as a user interface to generate direct position and orientation commands. Although the Geomagic Touch provides a more direct interaction with the device, our preliminary trials showed that 6-DOF control was actually more difficult with the Touch than with the Xbox controller. This may be due to the decoupling of the degrees of freedom to separate buttons when using the Xbox controller. Evaluating input devices is beyond the scope of this paper. However, as reviewed in (175; 176), haptic feedback may improve teleoperation performance in minimally invasive procedures, so incorporating these features by using a haptic device like the Touch could be beneficial for future clinical applications.

3.8.3 Workspace Analysis

Reachable and Strain-Limited Workspace

We determined the reachable workspace of this manipulator by uniformly sampling the 6-DOF actuation space at seven equally spaced increments on each leg, resulting in a total of 262,144 sampled points. At each sampled point, the forward kinematics was solved using the efficient torsionless model from our previous work (75; 170), which was optimized for computational speed. As we show in Section 3.8.4, mean accuracy for this model for our system is on the order of 1 mm. The workspace volume was calculated to be approximately 12,249 mm^3 by computing the volume of the non-convex 3-D point cloud hull generated using Matlab's `boundary`() with the default shrink factor of 0.5.

This point cloud represents the set of Cartesian coordinates that the robot could possibly reach. However, the leg bending strains required in these configurations will cause plastic deformation in the legs of the manipulator if the tube material's elastic strain limit is exceeded. We can calculate a strain-limited workspace by only including poses that do not exceed a given strain limit using the relationship $\epsilon = u_{max}r$, where u_{max} is the maximum curvature at any point on any tube leg (calculated

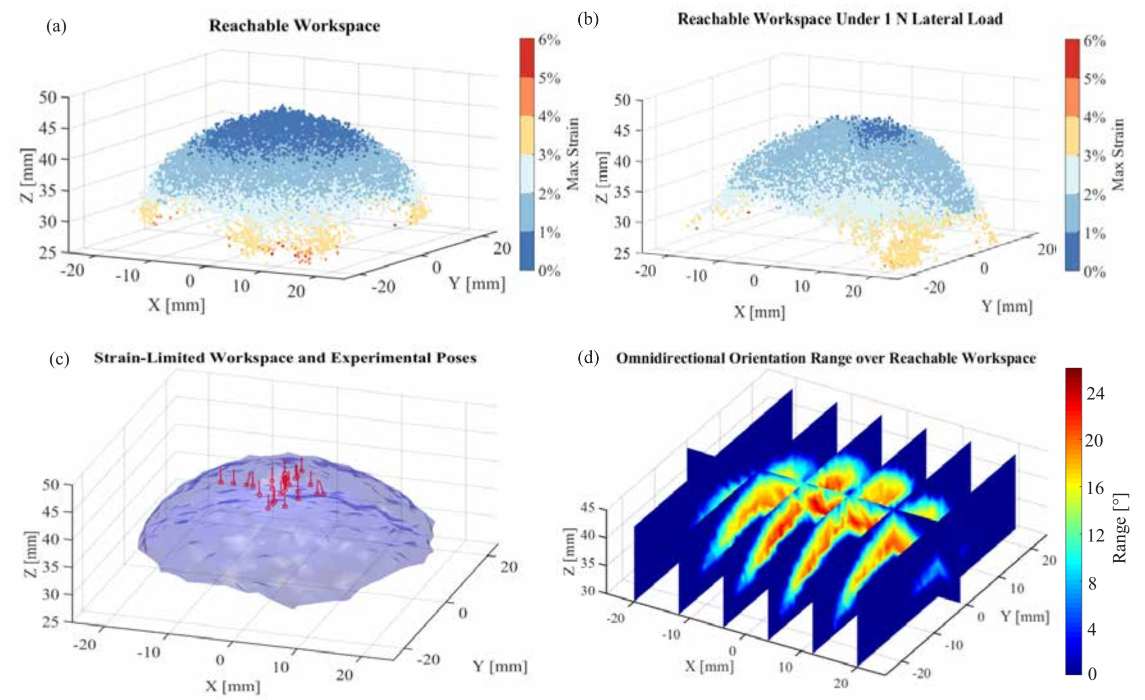
(a) Reachable Workspace

(b) Reachable Workspace Under 1 N Lateral Load

(c) Strain-Limited Workspace and Experimental Poses

(d) Omnidirectional Orientation Range over Reachable Workspace

Figure 3.14: (a) The reachable workspace of the manipulator is shown with color indicating the maximum strain in any leg at each position. (b) The reachable workspace was also simulated with a lateral load of 1N at the end effector acting along the x-axis. The subsequent shift in workspace and max strain is shown. (c) The strain-limited workspace is shown identifying the experimental poses used in our analysis with lines depicting the end-effector z-axis. (d) The dexterity of the manipulator over the workspace is visualized by calculating the range of angular displacement achievable in any direction of rotation at each reachable position.

using the model), and r is the tube radius. A plot of the workspace colored by the maximum strain at each pose is shown in Fig. 3.14 (a). The highest estimated strain over this entire workspace is 5.6%. Superelastic Nitinol has typical maximum recoverable strains of 6-8%. However, during teleoperation, we limit the workspace of the robot to strains under 2.5% to introduce a margin of safety and to reduce the effects of loading/unloading hysteresis in superelastic Nitinol. This strain-limited workspace and the experimental poses used for our analysis are shown in Fig. 3.14 (c). The workspace volume with strains below 2.5% is approximately 9,595 mm^3, a 28% reduction from the original reachable workspace. For comparison, the workspace volume is reduced to 3,974 mm^3 if the tube legs are made from spring steel, which typically has a strain limit of 1%. This is an 68% reduction. We conclude that using a material with a high recoverable strain is essential to maximize the workspace. Also note that these workspace volumes represent the positions achievable by a reference point at the center of the base of the grasper. The workspace of the tips of the grasper jaws is therefore slightly larger and more dexterous due to the length of the gripper and the two additional cable-driven DOF.

With 6-DOF, this robot can independently achieve pure translations and pure rotations in all three directions. Based on our inverse kinematics simulations, the limits of these isolated movements for our manipulator are approximately 12 mm in translation, 25° in x and y rotation, and 70° in z rotation (twist). When combining translation and rotation to achieve bending, the robot is able to reach x and y angles up to 45° with translational distances of 15 mm.

Force Application and Effects of Loading on Workspace

As discussed above, the high strain limit of Nitinol increases the workspace volume. Another benefit of Nitinol is wider availability in thin-walled tube stock compared to other flexible metals. Its relatively low elastic modulus (58 GPa) also increases the manipulator's compliance. Using our model, we can compute the manipulator stiffness matrix in any configuration. For example, in the neutral configuration shown in Fig. 3.10, the stiffness matrix is

$$K = \begin{bmatrix} 1.9 & 0 & 0 \\ 0 & 1.9 & 0 \\ 0 & 0 & 525 \end{bmatrix} N/mm.$$

The stiffness significantly varies with the configuration of the robot and the direction of the force applied. In poses near the home configuration, the stiffness matrix indicates that we can apply forces up to 5 N with a maximum displacement of 2.6 mm. The force application required during endoscopic submucosal dissection consists of applying traction to displace the mucosal and submucosal layers away from the musculature in order to dissect the tissue. This pull force has been measured on average to be 2.5 N with a maximum of 5 N (177). Tubes with higher stiffness can be used to provide higher end effector forces.

A second reachable workspace simulation was performed with a 1 N force applied in the $+x$ direction at the end effector. As shown in Fig. 3.14 (b), this applied force shifts the reachable workspace in the $+x$ direction. The total reachable workspace volume decreases to 11,326 mm^3, and the strain-limited workspace volume (for strains below 2.5%) decreases to 9,169 mm^3, which is a 4.4% reduction from the strain-limited workspace volume with no applied loads.

Required Actuation Forces

The lower elastic modulus of Nitinol also reduces the forces required for actuation. The axial tension or compression at the base of each leg is computed by our model, and this corresponds to the opposing actuator forces required to hold the manipulator at a given pose with external loading. When computing the workspace, we also recorded the required actuator forces at each pose. Over all configurations in the workspace, the maximum actuator force was 7.77 N, with an average force across the workspace of 1.02 N. In our loaded workspace simulation, the maximum actuator force was 8.20 N, and the average force was 1.27 N.

Dexterity over Workspace

Fig. 3.14 (a) depicts the reachable workspace of 3D points. However, each point in this simulation actually represents a full 6-DOF pose. To evaluate and visualize the dexterity over the reachable workspace, we chose a set of uniformly distributed “hub positions,” clustered all reachable poses within 1 mm of each hub, and evaluated the angular range of the poses in each cluster. To evaluate the angular range at each hub, we first found the Karcher mean orientation of each cluster using the algorithm in (178). Then we calculated the angular displacement between each orientation in the cluster and the mean. Next, we determined the largest origin-centered sphere that would fit within the non-convex boundary of each set of 3D angular displacements (determined by Matlab's `boundary`() command with a default shrink factor of 0.5). The diameter of this sphere represents the range of orientations that can be achieved in any direction at each hub. We also note that the set of reachable orientations at any hub is not necessarily symmetric. The metric we show in Fig. 3.14 (d) is conservative because it is limited by the direction in which the range is the smallest. In general, the range of achievable orientations about the end-effector z axis was about three times greater than the other directions.

3.8.4 Experimental Validation

In our previous work (75; 170) we presented a model for parallel continuum manipulators, an efficient computation method for solving the model in real-time, and a large-scale prototype (18 cm diameter). In the previous prototype, the rod ends were held by torsionless shaft collars that allowed axial rotation, and zero torsional moments were assumed as boundary conditions in the kinematics model. For our miniaturized design, it was impractical to include freely rotating shaft-collar connections due to size constraints, so the rods are fixed at both ends with epoxy. In this case, the relative axial rod orientations are fixed at each end, resulting in possible nonzero torsional reaction moments at the actuators and torsional deformation in the legs. This can be modeled by simply applying the appropriate boundary conditions to our models in (75; 170). In this section, we experimentally validate the accuracy of both modeling approaches (referred to as torsionless model and torsional model, respectively) for our miniaturized system.

Setup

We evaluated the open-loop accuracy of our system by measuring the position and orientation of the end effector using a tri-camera optical tracking system

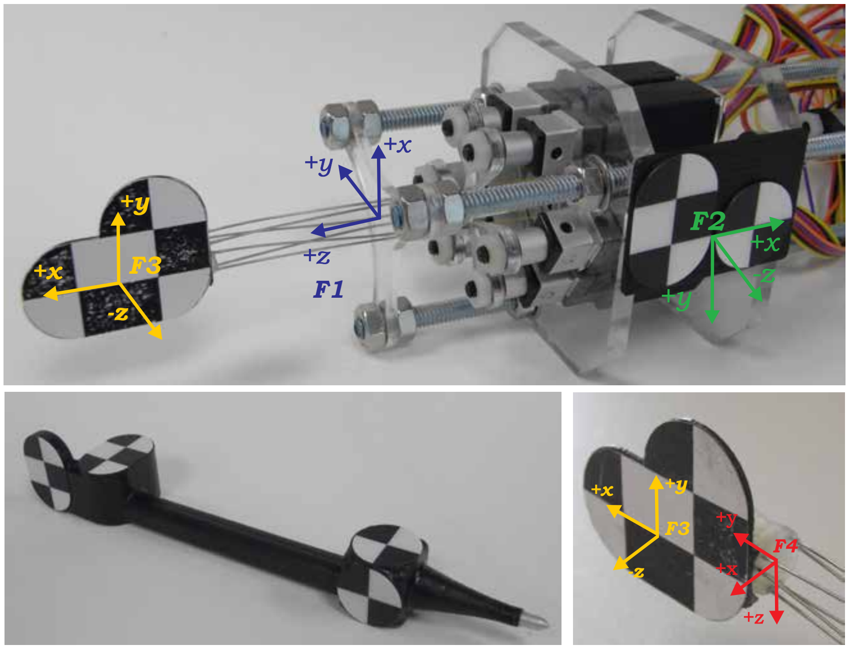

Figure 3.15: A stereo vision tracking system was used to measure the accuracy of the manipulator. Two passive markers were fixed to the robot, which allowed for measurement of the end-effector pose. A handheld stylus (bottom left) provided an accurate location of the manipulator's global frame relative to the base marker.

(MicronTracker H3-60, Claron Technology Inc.), which has a calibration accuracy of 0.2 mm RMS. Two passive 6-DOF markers were tracked, one fixed to the base of the robot (the base marker) and a second fixed to the end effector (the tip marker), as shown in Fig. 3.15. The robot reference frames used for evaluation are 1) the global frame of the manipulator F_1 (located at the base of the manipulator structure on the fixed platform), 2) the base marker frame F_2, 3) the tip marker frame F_3, and 4) the end-effector frame F_4. The pose of the end effector in the global frame is given by ${}^1\mathbf{T}_4 = {}^1\mathbf{T}_2{}^2\mathbf{T}_3{}^3\mathbf{T}_4$, where ${}^i\mathbf{T}_j \in \mathrm{SE}(3)$ is the homogeneous transformation from frame F_i to frame F_j.

Calibration

${}^1\mathbf{T}_2$ was found by measuring known points on the fixed platform using a handheld stylus with markers attached, as shown in Fig. 3.15. ${}^2\mathbf{T}_3$ was measured at each pose

Table 3.5: Calibration of Tip Marker to EE Frame Transformation

	θ_x [°]	θ_y	θ_z	x [mm]	y	z
Nominal	0	90	90	-22	0	8
Calibrated	7.5	87.95	84.46	-22.51	-1.86	6.63

using the Micron Tracker. The unknown transformation between the tip marker and the end-effector frame ${}^3\mathbf{T}_4$ was calibrated by minimizing the error between model predicted 6-DOF pose and measured 6-DOF pose using data from a set of 12 robot configurations, symmetric about the manipulator's neutral configuration, and the torsional model. These configurations included four translations, four rotations, and four cases of combined rotation and translation. To minimize the effects of repeatability error, each configuration was actuated and measured three times independently. The initial neutral configuration was also recorded to give a total of 37 measured poses. We then found the transformation that minimized a weighted combination of rotational and positional error by solving an unconstrained nonlinear optimization problem

$$P_{calibrated} = \text{argmin}_P \Big(\sum_{k=1}^{37} \left\| \begin{matrix} \vec{p}_{error} \\ S\boldsymbol{\theta}_{error} \end{matrix} \right\|^2 \Big),$$

where $P = \{x, y, z, \alpha, \beta, \gamma\}$ is the set of position vector elements and XYZ Euler angles that defines ${}^3\mathbf{T}_4$, $\vec{p}_{error} = \vec{p}_{sensed} - \vec{p}_{predicted}$ is the Euclidean distance between the predicted and sensed position, and $\boldsymbol{\theta}_{error} = (\log(R_s^T R_p))^\vee$ is the single axis rotation between the predicted rotation R_p and sensed rotation R_s. In the objective function, $\boldsymbol{\theta}_{error}$ is scaled by a characteristic length S, which we set as the distance from the end-effector frame origin to the axis of rotation of the grasper jaws (8.25 mm). The transformation that minimizes the objective function was found iteratively using Matlab's `fminsearch()`. The calibrated transformation was then used to compare model predictions to measured data for all subsequent data sets. Table 3.5 shows the initial guessed transformation and the calibrated transformation.

Table 3.6: Repeatability Error of EE Position and Rotation

	Home	Bending	Translation	Twisting
RMS Pos. [mm] (%)	0.88 (2.09)	0.35 (0.83)	0.54 (1.28)	0.74 (1.76)
Max. Pos. [mm] (%)	1.36 (3.24)	0.56 (1.33)	0.81 (1.93)	1.41 (3.33)
RMS Rot. [°]	1.96	1.37	0.77	2.47
Max. Rot. [°]	3.57	2.32	1.37	5.52

Repeatability

The repeatability of the robot was evaluated by measuring the pose in the home configuration, actuating to a new pose, actuating back to the home configuration, then measuring the pose again. This procedure was done for a set of 16 poses distributed over the workspace of the robot. These poses included 6 translations, 6 rotations, and 4 poses combining rotation and translation. The repeatability was similarly evaluated at three other representative configurations in the workspace for cases of 1) bending (6 mm translation plus 15° rotation), 2) translation of 5 mm, and 3) z-axis rotation of 30°. In addition to the position error and rotation error used for optimization, we evaluated percent error by dividing with a nominal length factor of 42 mm (length of the robot in the home configuration), that is $\%\ \text{Error} = \frac{||p_{error}||}{42mm} \times 100\%$. Table 3.6 gives the statistical results, which show that the repeatability error is no greater than 1.41 mm in position and 5.52° in rotation.

Absolute Position and Orientation Accuracy

The open-loop system accuracy was evaluated by first selecting a set of 42 desired poses distributed over the workspace of the manipulator. These poses included the initial and final neutral configurations, 14 translations, 12 rotations, 8 poses combining rotation and translation, and 6 z-axis rotations. The actuators were then commanded to move to the corresponding configurations computed by our inverse kinematics model, and the end-effector pose was measured by the tracking system and compared to the commanded pose. Table 3.7 details the statistical results of these measurements.

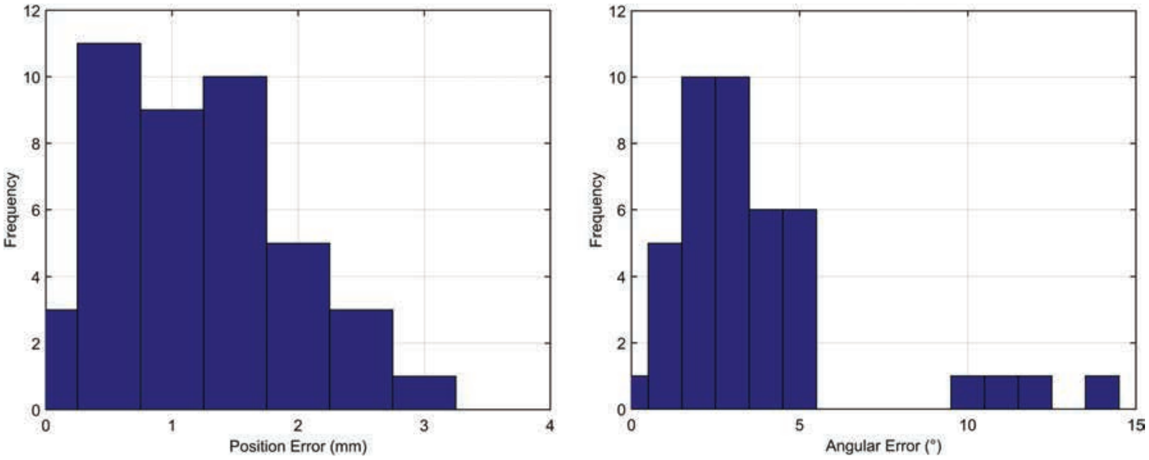

Figure 3.16: Histograms of position and rotation error for the torsional model are shown for all 42 measured poses. The six largest angular errors were calculated when pure twisting was being measured, consistent with the observation that twisting motions are particularly sensitive to actuator accuracy.

Fig. 3.16 shows the histogram for the position and rotation errors using the torsional model. The large angular errors above 5° were obtained when actuating the manipulator in pure z-axis rotation, i.e. about the manipulator's longest dimension. These large errors are mainly caused by linear actuator accuracy and interface rigidity. According to simulations, a rotation of 10° about the z-axis corresponds to a 0.1 mm actuator displacement for three of the legs. Although the specified positional accuracy of the linear actuators is 0.1 mm, axial backlash in the linear actuators and tab interfaces increases the uncertainty such that it is infeasible for such small position changes to be achieved.

We repeated the experiments using the torsionless model. As shown in Table 3.8, this increased the mean position error by 0.27 mm and the mean angular error by 0.44°. While the torsional model is more accurate, our efficient model implementation in (170) solves significantly faster in the torsionless case, for which it was optimized. The torsionless model accuracy is likely high enough for human-in-the-loop teleoperation and workspace simulation.

Table 3.7: End-Effector Pose Error: Torsional Model

Statistical Metric	Position (mm)	% Error	Angle (°)
Mean	1.19	2.83	3.81
Max.	3.05	7.26	14.0
Min.	0.13	0.31	0.33
Std. dev.	0.68	1.62	2.95

Table 3.8: End-Effector Pose Error: Torsionless Model

Statistical Metric	Position (mm)	% Error	Angle (°)
Mean	1.46	3.48	4.25
Max.	4.21	10.02	22.9
Min.	0.25	0.59	0.40
Std. dev.	0.86	2.05	5.32

3.9 Concentric Tube Modeling

Concentric-tube robots consist of multiple precurved elastic tubes which are arranged concentrically. The base of each tube is independently axially rotated and translated by an actuation system in order to change the distal shape of the tube collection and control the pose of the tip. In keeping with the physical system used in Chapter 6, we present a model for the kinematics of a collection of nested concentric tubes. The modeling is based on the work done by Rucker et al., which applied geometrically exact Kirchoff rod theory to pre-curved concentric tubes under arbitrary external point and distributed wrench loading (67). This modeling approach does not make the geometric assumptions present in classical beam theory, which allows us to simulate designs with a greater degree of accuracy. There exists two constitutive assumptions in Kirchoff rod theory, 1) inextensibility and no transverse shear strain, and 2) linear constitutive equations for bending and torsion. Since our concentric tubes must be long and very thin for endoscopic deployment, these assumptions are acceptable. The derivation of the geometrically exact model is well-described in (67). The resulting differential equations describe the tube curvatures with respect to the constitutive and kinematic variables. Friction is neglected in this modeling framework. However, as discussed in the next section, we chose to avoid tube designs which allow for overlap of two or more sections of distinct pre-curvature. This is because counter-rotation during curved section overlap contributes greatly to torsion in the tube transmissions, which causes a loss of controllability and can potentially create elastic instability (74; 179).

The resulting multi-tube kinematics and statics are defined by a set of first order differential equations for the set $\{g_1, \mathbf{u}_1, u_{2,z}, ..., u_{n,z}, \theta_2, ..., \theta_n\}$, as follows:

$$\dot{g}_1 = g_1\widehat{\boldsymbol{\xi}}, \quad \text{where} \quad \boldsymbol{\xi} = \begin{bmatrix}\mathbf{e}_3^T & \mathbf{u}_1^T\end{bmatrix}^T \tag{3.22}$$

$$\begin{aligned}\begin{bmatrix}\dot{u}_{1,x}\\ \dot{u}_{1,y}\end{bmatrix} = &-K^{-1}\sum_{i=1}^{n}\left(R_{\theta_i}(K_i(\dot{\theta}_i\frac{dR^T_{\theta_i}}{d\theta_i}\mathbf{u}_1 - \dot{\mathbf{u}}_i^*) + (\hat{\mathbf{u}}_i K_i + \dot{K}_i)(\mathbf{u}_i - \mathbf{u}_i^*)\right)\Bigg|_{x,y} \\ &- K^{-1}\left(\hat{\mathbf{e}}_3 R_1^T \int_s^{\ell}\mathbf{f}(\sigma)d\sigma + R_1^T\mathbf{l}\right)\Bigg|_{x,y}\end{aligned} \tag{3.23}$$

$$\dot{u}_{i,z} = \dot{u}^*_{i,z} + \frac{E_iI_i}{G_iJ_i}\left(u_{i,x}u^*_{i,y} - u_{i,y}u^*_{i,x}\right) + \frac{\dot{(G_iJ_i)}}{G_iJ_i}\left(u^*_{i,z} - u_{i,z}\right) - \frac{1}{G_iJ_i}\mathbf{e}_3^T R_i^T\mathbf{l}_i \tag{3.24}$$

$$\dot{\theta}_i = u_{i,z} - u_{1,z} \tag{3.25}$$

Variable definitions are listed in Table 3.9. Each variable can be expressed as a function of arc length s, and all dots denote a derivative with respect to s. The * superscript refers to the variable *before* it undergoes deformation in the nested state, which means solutions require tube pre-curvatures that are some known functions of arc-length. The $\widehat{\ }$ operator refers to a conversion of an element of $\mathbb{R}^3$ to its corresponding element in $\mathfrak{so}(3)$, as defined in Ref. 172. The x and y curvature components of the outer tubes are not necessary for describing the shape of the manipulator, because in a collection of nested concentric tubes, the deformed curves of all tubes follow the same trajectory. The main distinction from a single rod is that the tubes are free to twist independently about the local tangent z-axis.

The entire system is constrained by actuator inputs (rotations and translations) at the proximal end and static equilibrium conditions at the distal end. To implement

Table 3.9: Table of concentric tube kinematics variables.

Variable	**Definition**
g_1	Transformation describing the deformed backbone shape of the collection of tubes
$u_{i,j}$	Curvature of the ith tube about the local j axis, where the innermost tube is $i = 1$
θ_i	Angular rotation of the ith tube about the local z-axis with respect to the 1st tube
$\mathbf{e}_3$	Unit vector on local z-axis ($[0\ 0\ 1]^T$)
R_1	Rotation matrix for the first tube relative to global reference frame
R_{θ_i}	Rotation matrix (about the z-axis) for the ith tube relative to the 1st tube by the angular amount θ_i
$\mathbf{f}$	Distributed applied load
$\mathbf{l}$	Distributed applied moment
K	Stiffness matrix
E	Young's modulus
I	Second moment of area of tube cross section
G	Shear modulus
J	Polar moment of inertia of tube cross section

the forward kinematics, we solve the resulting boundary value problem by numerically integrating the first order system described in equations 3.22 - 3.25 for a given set of actuator inputs and guessed initial curvatures at the entry point of the manipulator. A shooting method is then used to iteratively find the initial curvatures which satisfy the static equilibrium at the distal end.

Overlap Constraint

In prior analysis of concentric tube kinematics, most pre-curved tubes have been designed with a single section of curvature at the distal end of the tube. For these types of designs, curved sections on separate tubes frequently overlap, causing an increase in internal moments, and creating torsion. In this paper, we constrain the design space to avoid the overlap of curved sections altogether and thereby eliminate the potential for torsional instability. We hypothesize that designs of this type are advantageous for robots which require a long, winding transmission path, as is the case in endoscopic procedures.

In our class of designs, we let all *outer* tube designs contain *straight* sections at their distal ends, with lengths that are greater than or equal to the length of the sum of all curved section lengths on *smaller* tubes. Then, tubes with pre-curvature contain segments in the order straight-curved-straight. This is in contrast to most prior designs which have simply been straight-curved. We define L_{s_i} and L_{c_i} as the lengths of the distal straight and curved sections of the ith tube, beginning from the base. Then, assuming there are at most two straight sections and one curved section in each tube design, the new section length constraint can be described as

$$L_{s_i} \geq \sum_{k=1}^{i-1} L_{c_k}. \tag{3.26}$$

Overlap of curved sections is then only possible when an inner tube is withdrawn far enough that its tip is further retracted than the tip of the next outer tube. This type of actuation does not result in any useful configurations, and therefore is disallowed in any control scheme.

Chapter 4

Analysis of Flexible Manipulators

While robotics has provided surgeons with the ability to complete complex tasks, the validation method of measuring a robot's ability to improve the surgical experience is qualitative and indirect. Most methods involve clinical parameters like reducing procedure time, increasing success rates, or minimizing tissue damage. While these factors are important and the ultimate goal of surgical robots, until the robot is almost fully constructed and implemented, these measures are difficult to assert. At present, researchers do not have an established set of guidelines for quantitatively determining whether a robotic manipulator meets the requirements for any given surgical application. The needs of a robotic manipulator have been studied in general (6), and in specific applications (3). However, the evaluation of these robots and their ability to perform tasks is still variable.

A design framework for a surgical robot was examined in (180). This framework begins with a characterization of the clinical application. This information is available for most procedures (3). Once this information is known, the researchers can choose kinematic topologies like joints, link lengths and actuation systems that will accomplish the targeted task. They can then compare kinematic simulations of their designs to clinical parameters in order to validate their robot's ability to perform a certain task.

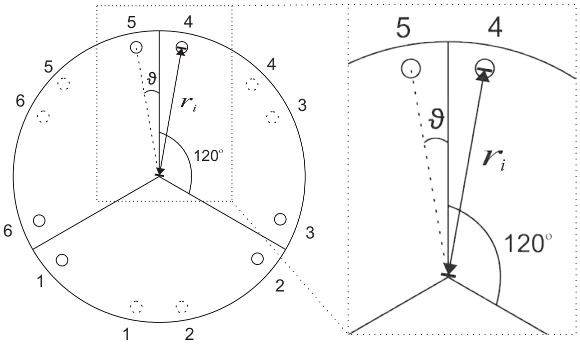

Figure 4.1: The angular offset of the flexible links is shown here as 10°. This offset can be increased or decreased by changing the location of the holes in the end effector platform. This will subsequently change the behavior of the manipulator. The radius, r_i is the radius from the center of the end effector to the center of the link.

In this chapter, we identify four kinetostatic matrices that represent the linearized robot behavior based on the kinetostatics model. We show how to numerically compute these matrices with minimal computational overhead beyond what is already required to solve the kinetostatics boundary value problem. We then analyze the design of PCRs with these matrices via (1) matrix ellipsoids, (2) matrix metrics, (3) non-dimensional analysis, and (4) force application calculations. We specifically examine three pose variations and two design variations.

4.1 Model Linearization

Linearizing the $\mathrm{F}_{q,w}$ formulation about the current robot configuration produces the following two equations

$$\begin{aligned} \left(\mathbf{g}_e^{-1}\delta\mathbf{g}_e\right)^{\vee} =& \mathbf{J}\delta\mathbf{q} + \mathbf{C}\delta\mathbf{w} \\ \delta\boldsymbol{\tau} =& \mathbf{K}\delta\mathbf{q} + \mathbf{W}\delta\mathbf{w} \end{aligned} \tag{4.1}$$

where δ denotes a very small change. In the first equation, we recognize the conventional definition of the $6 \times n$ body-frame Jacobian, $\mathbf{J}$ (mapping changes in joint positions to the corresponding changes in end-effector pose expressed in body-frame coordinates) and 6×6 body-frame compliance matrix, $\mathbf{C}$, (mapping changes in global applied wrench to body-frame pose change). This relationship has been stated for continuum robots in (181; 151), and is also generally true for robots with series-elastic actuators (182; 183) due to the flexible link between the applied actuator force and the load. As previously stated, rigid-link end-effector wrench is mapped to the joint torques by the transpose of the Jacobian matrix (162). Here, elastic energy is stored within the robot links. The compliance matrix accounts for the elastic deflection under external loading, and can be used to calculate the additional elastic energy that is stored in the flexible links of a continuum manipulator when it is deflected. In the second equation, the $n \times n$ matrix, $\mathbf{K}$ (which we henceforth refer to as the "input stiffness"), maps changes in joint positions to changes in actuator forces, and the $n \times 6$ matrix, $\mathbf{W}$ (which we call the "wrench reflectivity matrix"), maps changes in applied wrench to changes in actuator loads.

4.2 Efficient Computation of the Kinetostatic Matrices

In order to analyze the kinetostatic characteristics of a flexible manipulator, it is important to efficiently compute the required metrics on which to base design decisions. Here, we show that $\mathbf{J}, \mathbf{C}, \mathbf{K}$ and $\mathbf{W}$ can be calculated with minimal computational effort after solving the general BVP that defines any of the problem formulations outlined in Table 3.3. This method is similar to the one derived in (181). Equation (3.18) can be linearized about the current configuration in terms of pose ($\mathbf{g}_e$), actuator variables ($\mathbf{q}$), actuator forces ($\boldsymbol{\tau}$), and external wrench ($\mathbf{w}$), and the vector of remaining proximal unknowns $\boldsymbol{\gamma}$. Any small change in the residual function then has the following form,

$$\begin{aligned} \delta \mathbf{b} = & \mathbf{B}_\tau \delta \boldsymbol{\tau} + \mathbf{B}_q \delta \mathbf{q} + \mathbf{B}_w \delta \mathbf{w} \\ & + \mathbf{B}_g \left(\mathbf{g}_e^{-1} \delta \mathbf{g}_e \right)^\vee + \mathbf{B}_\gamma \delta \boldsymbol{\gamma} \end{aligned} \tag{4.2}$$

The $\mathbf{B}$ matrices in the above equation can be numerically approximated by the following finite difference procedure: For $\mathbf{B}_\tau, \mathbf{B}_q, \mathbf{B}_w, \mathbf{B}_\gamma$,

1. Increment an element of either $\boldsymbol{\tau}$, $\mathbf{q}$, $\mathbf{w}$, or $\boldsymbol{\gamma}$ by a small amount, Δ, from it's nominal value (which is either known or has already been obtained in the solution of the BVP). If the incremented variable is an element of $\mathbf{w}$, go directly to step 3.

2. Solve (3.17) for the link which is associated with the incremented variable from base to tip as an initial value problem.

3. Evaluate the change in $\mathbf{b}$ that the increment produced and divide by Δ. The resulting vector is assigned in the appropriate column of the $\mathbf{B}$ matrix associated with the incremented variable.

For $\mathbf{B}_g$,

1. Increment $\mathbf{g}_e$ as follows,

$$\Delta \mathbf{g}_e = \mathbf{g}_{e,i} \widehat{\mathbf{e}}_i \Delta \tag{4.3}$$

   where $\widehat{\ }$ maps $\mathbb{R}^6$ to $\mathfrak{se}(3)$ as given in Equation (3.4), and $\mathbf{e}_i$ is a column vector of zeros with 1 in the ith row.

2. Evaluate the change in $\mathbf{b}$ that the increment produced and divide by Δ. The resulting vector is assigned in i^{th} column of the $\mathbf{B}_g$ matrix.

Note that $\mathbf{B}_g$ and $\mathbf{B}_w$ could also be obtained analytically by direct differentiation of $\mathbf{b}$, since $\mathbf{w}$ and $\mathbf{g}_e$ appear explicitly in the distal boundary condition equations.

After solving the BVP and obtaining all of the $\mathbf{B}$ matrices, we can compute the four kinetostatic matrices by first observing that the residual vector, $\mathbf{b}$, and its derivative should remain equal to zero for any small change in any variable. Setting

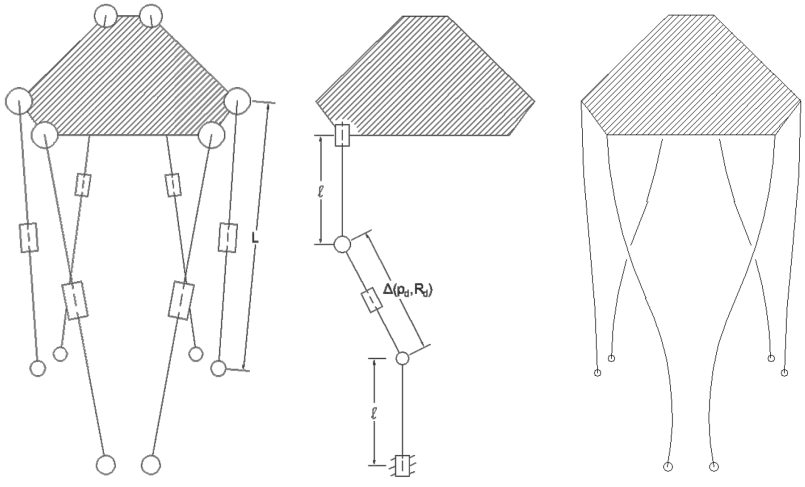

6-Link Stewart Gough 18-Link Stewart Gough Constant Jacobian

Figure 4.2: Each of the models above approximates the full Cosserat rod model body-frame Jacobian in real-time.

$\delta\mathbf{b} = 0$ and rearranging provides the following equation,

$$\begin{bmatrix} \delta\boldsymbol{\gamma} \\ (\mathbf{g}_e^{-1}\delta\mathbf{g}_e)^\vee \\ \delta\boldsymbol{\tau} \end{bmatrix} = \mathbf{G} \begin{bmatrix} \delta\mathbf{q} \\ \delta\mathbf{w} \end{bmatrix} \tag{4.4}$$

where

$$\mathbf{G} = -\begin{bmatrix} \mathbf{B}_\gamma \mid \mathbf{B}_g \mid \mathbf{B}_{\boldsymbol{\tau}} \end{bmatrix}^{-1} \begin{bmatrix} \mathbf{B}_q \mid \mathbf{B}_w \end{bmatrix} \tag{4.5}$$

$\mathbf{G}$ then contains the four kinetostatic matrices as appropriately dimensioned sub-blocks, which can be extracted from it.

$$\mathbf{G} = \begin{bmatrix} \multicolumn{2}{c}{\boldsymbol{\Gamma}} \\ \mathbf{J}_{6\times n} & \mathbf{C}_{6\times 6} \\ \mathbf{K}_{n\times n} & \mathbf{W}_{n\times 6} \end{bmatrix} \tag{4.6}$$

where Γ is the matrix relating the actuation variables and the tip wrench to $\boldsymbol{\gamma}$.

4.2.1 Approximation of Jacobian in Teleoperation

In (184), we investigated using an analytical Jacobian to teleoperate a 6-link Stewart Gough parallel continuum robot. Simpler approximate kinematic models can be obtained by considering related rigid-link Stewart-Gough platforms and linearizing the full model (see Figure 4.2).

In this 6-Link Stewart Gough approximation a standard closed form expression for leg lengths is used,

$$L_i = ||\mathbf{p} + \mathbf{R}[x_{i,e}\ y_{i,e}\ 0]^T - [x_{i,b}\ y_{i,b}\ 0]^T|| \tag{4.7}$$

The 18-Link Stewart Gough approximation uses additional links to better approximate leg shape and orientation constraints. The equation for leg length is

$$\begin{aligned} L_{i,k} =& 2l_{i,k} + ||\mathbf{p} + \mathbf{R}[x_{i,e}\ y_{i,e}\ \ -l_{i,k}]^T - [x_{i,b}\ y_{i,b}\ l_{i,k}]^T|| \\ l_{i,k+1} =& l_{i,k} + \alpha(\beta L_{i,k} - l_{i,k}) \end{aligned} \tag{4.8}$$

where l_i is the length of the outer segment and L_i is the total length. The segment converges to the fraction β of L_i with a damping constant of α. This model used $\beta = 0.25$ and $\alpha = 0.001$.

The constant Jacobian approximation is a linearization of the full Cosserat rod model at nominal configuration with a precomputed 6 DOF Jacobian matrix and leg lengths calculated by integration of velocities. The equation for the leg lengths is

$$L(t) = L(0) + \int_0^t \mathbf{J} \begin{bmatrix} v(s) \\ u(s) \end{bmatrix} ds \tag{4.9}$$

User experiments were conducted with each of the models (see Figure 4.3). Users were asked to teleoperate the PCR to a specific location with a 6-DOF mouse from 3D Connexion Inc.. The algorithms were implemented in Simulink with MATLAB. The legs were translated by 6 linear actuators from Firgelli Acutonix Motion Devices Inc.,

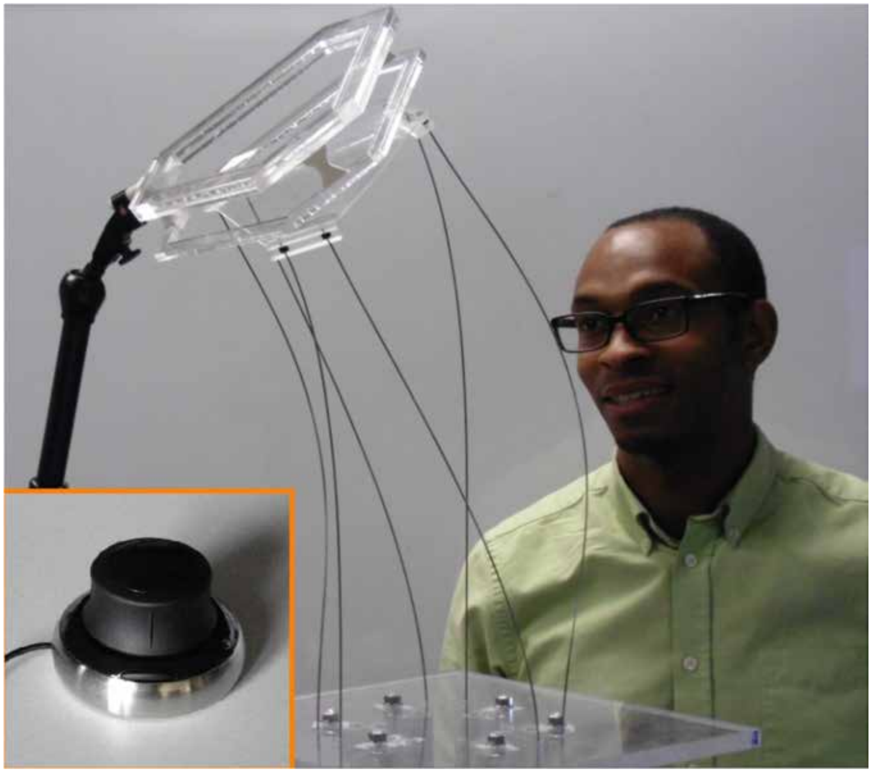

Figure 4.3: Users were asked to navigate the PCR with a 6-DOF mouse to a desired 6-DOF pose represented with a jig in the shape of the end effector.

with low level PI control from an Arduino Mega 2560 microcontroller. Six novice users maneuvered the robot to target 6 DOF pose in 3 runs for each model. The models were presented in a blind order so that the user did not know which model they were using. The time to reach the desired pose was measured and recorded.

The results of the user experiments are shown in Figure 4.4. There were insignificant difference between the rigid-link models. However, there was a significant difference between the full Jacobian and both rigid-link models. Users were able to complete the task much faster with the Jacobian model.

4.3 Matrix Analysis

In this section we employ several matrix metrics (Table 4.1) and visualize aspects of robot behavior with ellipsoids (Figures 4.5 and 4.6). The particular robot design

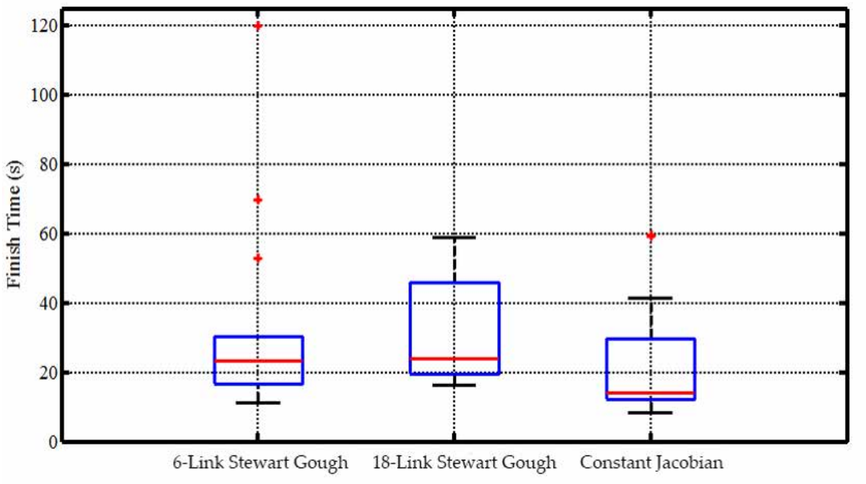

Figure 4.4: Users were asked to navigate the PCR with a 6-DOF mouse to a desired 6-DOF pose represented with a jig in the shape of the end effector.

analyzed is a Stewart-Gough design with a nominal length of 400 mm and a radius, r_i, equal to 87 mm for each link. The link connection points are offset from the three 120° dividing lines by $\vartheta = 10°$ (see Figure 4.1). This design is similar to the prototype presented in our previous work (75). The design we consider in Section 5 has different physical parameters which are more conducive to the force sensing experiments. A six link platform design was used to take advantage of the square system of inputs and outputs in order to analyze the position and rotation Jacobian matrices alongside the compliance and force reflectivity matrices. The choice of a Stewart-Gough-like hexapod arrangement for the legs provides well-conditioned control of 6-DOF pose and wrench sensing. The goal will be to characterize the robot's abilities in terms of manipulability, force application, stiffness and force sensing using the **J**, **C**, **K**, and **W** matrices. While the use of the Jacobian and compliance matrices is well-known, the stiffness matrix will aid in motor selection for specific designs by estimating the forces required to actuate the flexible links. Finally, the wrench reflectivity matrix can be used to estimate the robot's ability to intrinsically sense applied tip wrenches via the measurement of the actuator loads.

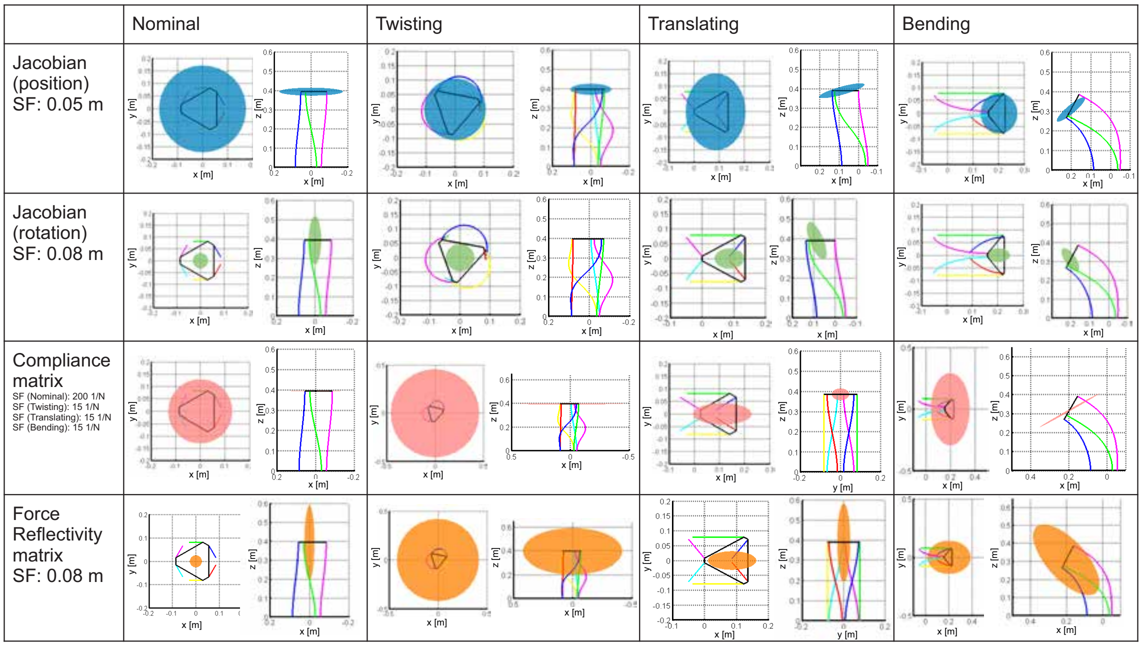

Figure 4.5: This figure shows the resulting ellipsoids when the manipulator is in 3 separate configurations, twisting about the z axis, translating along the x axis and bending in the negative x direction.

The Jacobian is commonly used to measure manipulability by analyzing several different metrics, including the determinant, the condition number of the matrix, and the volume of ellipsoids drawn from either the singular values or the eigenvalues and eigenvectors of the matrix (162; 185; 146; 150). In order to avoid the mixture of rotational and positional units, we have calculated separate ellipsoids for position and rotation manipulability (see Figure 4.5 and 4.6, rows 1 and 2). It is also possible to assign a characteristic length in order to appropriately scale the rotational elements and then analyze the entire matrix. However, this choice is arbitrary and difficult to visualize in 2D.

We generate a manipulability ellipsoid for the position and rotation portions of the matrix by mapping a unit sphere in joint space to an ellipsoid in end-effector Cartesian space through the Jacobian. Then, the magnitude of the position/rotation ellipsoid radius corresponds to the ability of the robot to move/rotate in the corresponding direction. A large radius corresponds to a small amount of displacement in the

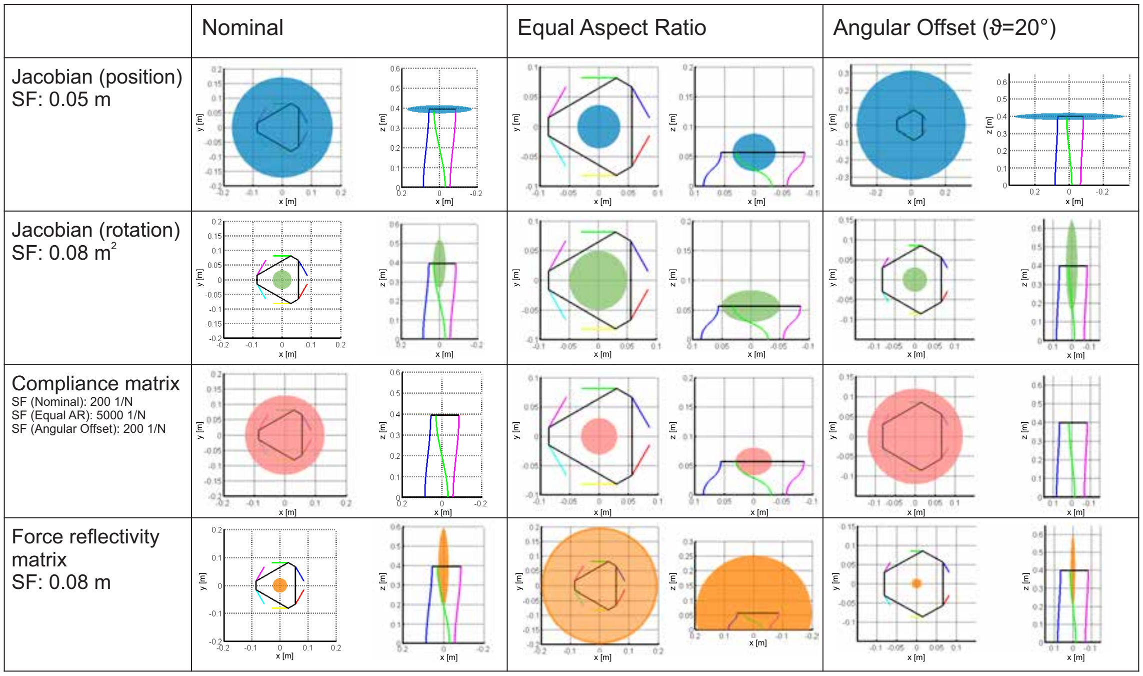

Figure 4.6: This figure shows the position (blue) and rotation (green) ellipsoids from the body Jacobian as well as the force displacement ellipsoid from the compliance matrix and the force reflectivity ellipsoid from the wrench reflectivity matrix.

actuator space required for a relatively large amount of displacement in Cartesian space.

This process can also be applied to the force/displacement portion of the compliance matrix and force portion of the wrench reflectivity matrix. Equation (4.6) contains the full compliance matrix related to linear and angular displacements and wrench. The displacement/force sub-block (the upper 3x3 block, designated $\mathbf{C}_f$) of the compliance matrix, is used to calculate the ellipsoid shown in Figures 5 and 6. This reduction in dimension is made for unit consistency and because a 6-dimensional ellipsoid is difficult to visualize in 2D projections.

Similarly, the force reflectivity ellipsoid is computed using the force/force sub-block (the upper 3x6 block, designated $\mathbf{W}_f$) of the wrench reflectivity matrix in Equation (4.6). This portion of the matrix involves only the tip forces and the actuation forces, and ensures unit uniformity. These same matrices were used in the calculation of the indices reported in Table 4.1. The ellipsoid demonstrates the direction in which the forces are more or less “sensible” via transmission to the actuator loads. If the magnitude of the ellipsoid radius is large, a small change in the external force at the tip corresponds to a large change in the actuation forces that are sensed at the base of the link. If this is the case, the measurement would be more easily detected by the sensor.

4.3.1 Pose Variations

In Figure 4.5, the particular manipulator is represented in the nominal configuration (Column 1) along with three pose variations (Columns 2-4). The radii of each ellipsoid have units corresponding to the units of the respective matrices. In order to plot the ellipsoids in Cartesian space, each ellipsoid has been scaled by a factor (SF) in order to convert the units to length and provide the best visualization for the plots. This scaling is arbitrary and has been applied to the ellipsoid uniformly over all three principle radii. The values and units for the scaling factors are shown in the figure.

Nominal Configuration

In the nominal configuration, the position manipulability ellipsoid shows that the manipulator is isotropic in the x and y directions. The z axis radius is much smaller than the x and y, indicating that the required actuator displacements are much higher to move in the z direction. The rotational ellipsoid has a large radius in the z direction compared to the x and y axes. This is consistent with the ease of twisting that is achieved in the axial direction versus the larger actuator displacement required to tilt to an equal angular displacement in the x and y directions. However, ease of movement in a direction also corresponds to higher pose error propagation in that direction. This is consistent with the fact that forces on the order of 1 N will displace the manipulator a distance on the order of 1 mm (as predicted by the plot, the compliance ellipsoid in the nominal configuration and the Scale Factor equal to 200 1/N). The compliance in the x and y directions is much larger than in the axial direction. This outcome is consistent with the direction of maximum stiffness being the axial direction. The force reflectivity matrix shows that forces in the axial direction will be well reflected at the base since the largest radius is in the axial direction.

Twisting

In Figure 4.5, the second column shows the resulting kinetostatic ellipsoids when the manipulator is twisted about the z axis. The position ellipsoid radius in the x and y direction is smaller. This would indicate that it is more difficult to move in the x and y directions when the manipulator is twisted. The rotation ellipsoid is flattened in the z direction. This would be expected since the manipulator is already twisted in that direction. The length of the radius could potentially be used as an indicator of when the twisting limit is reached. The compliance ellipsoid radius in the x and y direction is significantly larger. This would indicate that the robot is much less stiff in the x and y directions when it is twisted. The force reflectivity matrix is much larger and more isotropic, which means it could be more effective at sensing forces in this configuration.

Translating

The kinetostatic ellipsoids in the third column result from the manipulator being translated in the x-y plane. All of the ellipsoids tilt. There are no significant changes in the size of the ellipsoids except for the compliance ellipsoid which shrinks in the direction perpendicular to the plane of translation, indicating that the robot is stiffer in the direction perpendicular to its translation.

Bending

The fourth column of Figure 4.5 shows the manipulator bent in the x-z plane. Again, all the ellipsoids tilt. The position and compliance ellipsoids tilt in the opposite direction of the bending, while the rotation and force reflectivity tilt in the same direction. Both of the position and rotation ellipsoids shrink in response to the manipulator moving toward a singular configuration. The compliance matrix grows in the x and y directions, indicating that the manipulator is more flexible in the bent state in those directions. The force reflectivity ellipsoid also grows, which means the forces at the tip are better transmitted to the actuators in this pose.

4.3.2 Design Variations

In Figure 4.6, the manipulator is represented in the nominal configuration (Column 1) along with two design variations (Columns 2 and 3). The first column shows each ellipsoid while the manipulator is in the nominal configuration with all link lengths equal. The second column shows the same design but with an aspect ratio (relationship between the total length and the radius) of 1:1. The third column shows the same design with an increase in the angular displacement of the links both proximal and distal (from 10° to 20°).

Equal Aspect Ratio

The aspect ratio of the robot is the ratio of the radius, r (distance from the center of the end effector to the link constraint holes), to the total length of the robot in the nominal straight configuration, L. In the nominal configuration, this ratio was 1:4.6. In Column 2 of Figure 4.6, the ratio is 1:1. All of the ellipsoids are more isotropic than in the nominal configuration. However, the radius also decreased in all but the force reflectivity ellipsoid. The diameter of the compliance ellipsoid significantly decreased and required a much larger scaling factor in order to visualize the ellipsoid. From these results, it can be shown that a very short PCR is a very sensitive force sensor. However, the volume of the position and rotation ellipsoids are greatly decreased in the nominal configuration. This could indicate that the manipulator is more constrained in a shorter configuration. However, this was not the case for the force reflectivity ellipsoid. Instead of decreasing in size, the ellipsoid increased in volume by 6000%, providing a larger range of sensable forces.

Angular Offset

The link angular offset is the angular displacement of the links from the equally spaced 120° lines dividing the circumference of the manipulator (see Figure 4.1). In Column 1 of Figure 4.6, $\vartheta = 10°$, and in Column 3, $\vartheta = 20°$ with a total angular offset of 40° between the flexible links. The positional ellipsoid shows a much larger diameter in the x and y directions. Since the scaling of the positional ellipsoid is constant, this translates to a larger Cartesian displacement for the same amount of actuator displacement. There is also a larger diameter in the z direction for the rotational ellipsoid. This indicates a greater degree of axial twisting is possible. There is no significant change in the compliance matrix in this simulation. There is a much smaller diameter in the x and y directions of the force reflectivity matrix, suggesting that this PCR design is a much less sensitive force sensor.

4.3.3 Matrix Metrics

The μ term in (162; 150) of the form

$$\mu = \sqrt{det\,(\mathbf{A}\mathbf{A}^T)}, \tag{4.10}$$

is the most widely accepted measure for kinetostatic manipulability when applied to the Jacobian matrix. For the Jacobian matrix, μ measures the relative proximity of the current configuration to a singular configuration. If the matrix is square, it reduces to the absolute value of the determinant. For an arbitrary matrix, it generally corresponds to the notion of volume spanned by the matrix columns. A value of 0 implies a configuration that is singular. This metric is also calculated for the compliance and force reflectivity matrices. The results are reported in Table 4.1 for $\mathbf{J}_p$, $\mathbf{J}_r$, $\mathbf{C}_f$ and $\mathbf{W}_f$. The values for the force compliance matrix are close to zero.

Table 4.1: Matrix Indices

	μ			
Pose	$\mathbf{J}_p$	$\mathbf{J}_r$	$\mathbf{C}_f$	$\mathbf{W}_f$
Nominal	4.93	0.27	9.25E-12	0.25
Equal Aspect Ratio	0.34	0.13	4.45E-16	15.25
Angular Offset (+10	16.52	0.45	2.11E-12	0.06
Twisting	2.85	0.01	5.93E-07	65.62
Translating	3.64	0.22	6.06E-10	0.46
Bending	1.30	0.12	1.86E-07	7.40
	β			
Pose	$\mathbf{J}_p$	$\mathbf{J}_r$	$\mathbf{C}_f$	$\mathbf{W}_f$
Nominal	0.36	0.44	0.09	0.19
Equal Aspect Ratio	0.99	0.87	0.97	0.99
Angular Offset (+10	0.24	0.19	0.04	0.08
Twisting	0.60	0.21	0.06	0.82
Translating	0.38	0.50	0.026	0.25
Bending	0.56	0.61	0.10	0.81

This is due to the high degree of axial stiffness (in the z direction) when compared to the x and y directions from the inability to compress the links.

The second measure in the table, β, is the ratio of the largest and smallest singular values, and measures the isotropy of the ellipsoid. It is an index of the directional uniformity of the ellipsoid that is independent of its size (162). It can also be interpreted as the measure of accuracy with which the manipulator can generate output forces from input forces, and workspace velocity from joint velocity (150). The measure of isotropy has an upper bound of 1 and measures how close the ellipsoid is to a perfect sphere where all the eigenvalues would be equal.

When comparing the indices for the position and rotation ellipsoids in the nominal pose, β is not close to zero, which indicates that the robot is not singular in the

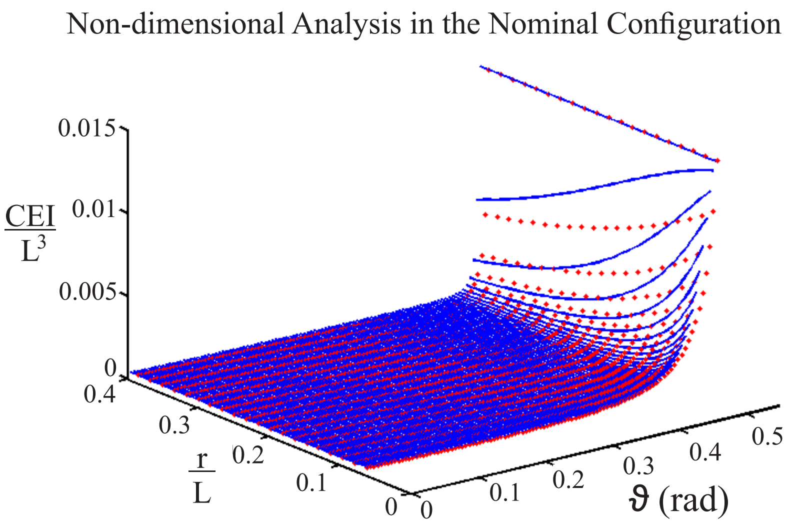

Figure 4.7: The results of the fitted data (Equation (4.12)) are shown here as red diamonds, and the simulation data is shown in the blue line. The sudden change in compliance near $\vartheta = 30°$ is an interesting result of this analysis.

configurations examined. This is consistent with previous findings of the nominal configuration in (75). The compliance matrix is significantly skewed in the x and y directions, and this leads to a very low value for the isotropy. Examining β for the equal aspect ratio case in Table 4.1, it is evident that all the matrices are extremely well conditioned in this configuration. The μ value for the angular displacement case shows the volume of the force reflectivity matrix decreased significantly.

4.4 Non-dimensional Analysis

We would like to obtain a generally applicable function that relates how the link lengths, hole-pattern radius, link bending stiffness, and hole-pattern angular offset affect the end-effector output compliance matrix (specifically the transverse compliance, $C_{xx} = \frac{\partial p_x}{\partial f_x}$, which is the first diagonal element in the compliance matrix) for any Stewart-Gough PCR in the nominal configuration. Knowing how to select physical parameters that correspond to a specific stiffness can aid in designing robots to interact with specific stiffness requirements, such as probing soft tissue or working close to a human collaborator. To obtain such a generalized relationship, we used the Buckingham Pi method (186) to find 3 dimensionless groups. For our analysis, there are 5 problem parameters (L, r, ϑ, EI, and C_{xx}) and 2 physical dimensions in the problem (length and force). According to the Buckingham Pi theory, there are then 3 dimensionless groups.

The first two groups are the aspect ratio (radius of the robot divided by the length), and the angular offset of the flexible links in degrees.

$$\Pi_1 = \vartheta$$
$$\Pi_2 = \frac{r}{L}$$

A third dimensionless group can be written in terms of the compliance, stiffness, and length,

$$\Pi_3 = \frac{C_{xx}EI}{L^3}.$$

Therefore, some function exists which relates the dimensionless groups as follows:

$$\frac{C_{xx}EI}{L^3} = f(\vartheta, \frac{r}{L}) \tag{4.11}$$

If the design required increased or decreased compliance, these non-dimensional groups provide insight on how to scale the physical parameters of the manipulator. This formulation reveals that if all the length dimensions of the manipulator (r, L, and link diameter through I) are scaled by a factor, β, the compliance, C_{xx}, will be scaled by $\frac{1}{\beta}$. Also, if the length and radius of the manipulator are both scaled by a factor, β, then the compliance will increase by a factor of β^3. These general rules equally apply to any other element of the compliance matrix, and also to the inverse of the input stiffness matrix $\mathbf{K}$, since we could have chosen any scalar compliance for the formation of Π_3.

To determine a functional approximation for Equation (4.11) above, we used the mechanics model to simulate a range of aspect ratios and angular offsets and calculated the resulting C_{xx}. The angular offset ranged from 0° to 30° (i.e. from designs with leg pairs coincident to designs with equally spaced, straight legs), and the aspect ratio ranged from 0.0625 to 0.4. The values were plotted against Π_3 and fitted to a function using the Eureqa Pro tool from Nutonian Inc., which uses a genetic algorithm to find an appropriate functional form that fits a set of data. We converged on an equation with the following form:

$$\frac{CEI}{L^3} = c_1 + c_2\vartheta + c_3\vartheta^2 + \frac{c_4\vartheta^4}{c_5\vartheta\frac{r}{L} + c_6 + c_7\frac{r}{L}} + c_8\vartheta^7 \tag{4.12}$$

$$\begin{aligned}
c_1 &= 0.000489911011960653,\\
c_2 &= -7.708585607305636e \times 10^{-4},\\
c_3 &= 0.001122924359743,\\
c_4 &= -0.019046236046962,\\
c_5 &= 57.295779513082323,\\
c_6 &= -0.0923645619398372,\\
c_7 &= -30.0023461726314,\\
c_8 &= -0.175434258024175.
\end{aligned}$$

The genetic algorithm provides the user options to balance complexity of the resulting equation and a better fit of the data. This equation best fits the experimental data. While some of the coefficients are small in magnitude, they are multiplied by exponential terms, which increases their contribution to the overall equation. This polynomial produced an R-squared value of 0.966 for the data collected, and reflects the expected compliance of the manipulator when given an aspect ratio and an angular displacement of the flexible links from the mid-line (see Figure 4.1). We measured the percent error between the data set and the fitted equation and found a maximum percent error of 25.4%. The results of the dimensional analysis simulation are shown in Figure 4.7. It is important to note that this function is valid only for the

Table 4.2: Force Application [N] per Configuration

Pose/Variation	$x = 1$ mm	$y = 1$ mm	$z = 1$ mm
Nominal	[1.54 0 0.01]	[0 1.54 0]	[0.01 0 109.5]
Aspect Ratio	[160.5 0 1.5]	[0 160.4 -0.4]	[0.8 -0.02 210.4]
Angular Offset	[1.65 0 0.05]	[0 1.65 -0.01]	[0.04 0.01 407.0]
Twisting	[0.03 0 0]	[0 0.03 0]	[0 0 3.82]
Translating	[2.36 0 9.37]	[0 0.1 0]	[9.35 0 37.7]
Bending	[0.81 0 1.28]	[0 0.05 0]	[1.29 0 2.36]

limits of the simulation data and will decrease in accuracy if used outside these limits. There is a hyperbolic relationship between the angular offset of the flexible links and the compliance term. This curve is sharpened when the aspect ratio of the robot is increased. Due to the non-dimensional nature of the analysis, these findings and this equation applies to all Stewart-Gough PCR robots, regardless of size or materials. The findings will facilitate robot design without requiring the full kinetostatic model.

4.5 Force Application

It is important to know the end-effector's force application capacity in different directions and for different configurations in order to assess the manipulator's ability to perform certain tasks. In order to assess the force application capacity, the displacement/force (upper 3×3) sub-block of the compliance matrix can be used to solve for the force required to produce any small linear displacement. Using this approach, we analyzed the 3D forces required to produce a displacement of 1 mm in the x, y and z directions (in the local end-effector frame) for a manipulator in the 6 pose and geometry variations examined in this section. The results are presented in Table 4.2. In the nominal configuration the x and y displacement forces are symmetrical while the z force is quite large in comparison. This agrees with the representation of the compliance matrix in Figures 4.5 and 4.6. The equal aspect ratio values demonstrate the scaling of the force application capacity when the manipulator is shortened. If the manipulator is shortened 87%, then the force it can apply before displacement of 1 mm increases by a factor of 2 in the z direction and by a factor of 100 in the x and y directions. The increase in angular offset results in only marginal increases in force application capacity in the x and y directions, but increases the capacity in the z direction by a factor of 4. Twisting is shown to greatly decrease the stiffness in the x and y directions and increase it slightly in the z direction. Translating in the $x-z$ plane greatly reduces the stiffness in the y direction. Bending in the $x-z$ plane also decreases the stiffness in the y direction.

Chapter 5

Force Sensing and Control with Parallel Continuum Manipulators

In this chapter, we utilize the kinetostatic formulations presented in Section 3.5 to sense tip forces on a PCR equipped with tension/compression load cells at the base of each rod to provide an input for $\boldsymbol{\tau}$. The results demonstrate that force sensing with actuation-based inputs is accurate to within 0.3 N and has better conditioning than deflection based force sensing.

We also present a passive stiffness controller using the kinetostatic matrices formulated in Section 4.2. This control scheme uses a gain matrix based on these matrices to change actuator inputs (either $\mathbf{q}$ or $\boldsymbol{\tau}$) and can be used in position control or direct drive control.

5.1 Force Sensing

In Section 3.5, we presented three different model formulations for force sensing with parallel continuum manipulators. In choosing a force sensing approach, it is important to understand how the errors in the input values will affect the accuracy of the sensed wrench. In order to compare the available options for force sensing methods, the 3

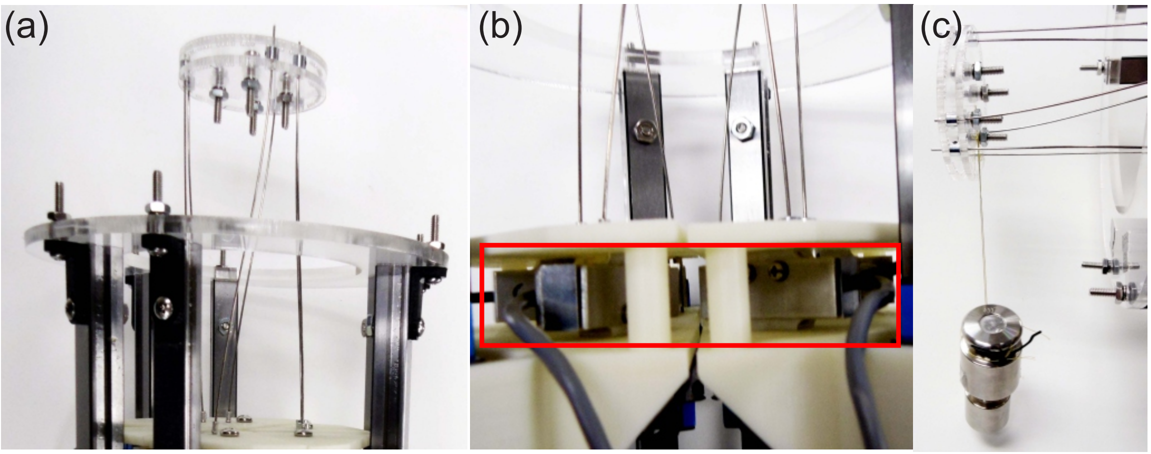

Figure 5.1: (a) The manipulator consists of 6 flexible steel spring tempered carbon steel wire rods (AISI 302/304 stainless steel) connected in the traditional Stewart Gough configuration. (b) The Omega load cells are connected directly to the flexible rods to measure the actuation forces and translated by linear rails and carriages. (c) A 300g weight was hung from the centroid of the end effector for each of the force application experiments.

sensing formulations were evaluated to investigate error propagation from the actuator positions, actuator forces, and pose.

In $\mathrm{F}_{q,\tau}$, error could arise from the actuator force measurement or the commanded actuator variables. Solving the second equation in (4.1) for the wrench gives,

$$\delta \mathbf{w} = \mathbf{W}^{-1}\delta\boldsymbol{\tau} - \mathbf{W}^{-1}\mathbf{K}\delta\mathbf{q} \tag{5.1}$$

In order to analyze the effect of errors in actuator displacement and force measurement, we assume Gaussian distributions in the input and output variables and define the input covariance matrix which is then transformed through the above equation to provide an output covariance (187). This has the following form,

$$\Sigma_w = \begin{bmatrix} \mathbf{W}^{-1} & -\mathbf{W}^{-1}\mathbf{K} \end{bmatrix} \begin{bmatrix} \Sigma_\tau & \mathbf{0} \\ \mathbf{0} & \Sigma_q \end{bmatrix} \begin{bmatrix} \mathbf{W}^{-1} & -\mathbf{W}^{-1}\mathbf{K} \end{bmatrix}^T \tag{5.2}$$

where the Σ_τ and Σ_q terms are the input covariances of the actuation forces and actuation variables. We assume that the error of each input is independent and uncorrelated so that these are both diagonal matrices.

The covariance is based on the range of accuracy that is estimated for each input. The square root of the variance of the error can be tripled to provide a range of error that contains the 95th percentile for the Gaussian distribution. Therefore, the estimated maximum error range can be divided by 3 and squared to arrive at the covariance value. The diagonal elements of the output covariance matrix, Σ_w, can be rooted and multiplied by 3 to find the 95th percentile range of error for tip wrench. For an input range of 0.1 N for $\boldsymbol{\tau}$ (estimated from our force sensor data in Section 5.1.3) and 0.5 mm for $\mathbf{q}$ (estimated from linear actuator repeatability), the maximum range for force errors using the actuation based force sensing method, $\mathrm{F}_{q,\tau}$, is 0.0136 N in the nominal configuration, with a moment error range of less than $1\mathrm{e}^{-4}$ Nm. We note that this error estimate is pose dependent, since it uses the linearized matrices about the current pose.

The generalized deflection-based force sensing method, $\mathrm{F}_{g,q}$, for a PCR would use the following equation

$$\delta\mathbf{w} = \mathbf{C}^{-1}(\mathbf{g}_e^{-1}\delta\mathbf{g}_e)^\vee - \mathbf{C}^{-1}\mathbf{J}\delta\mathbf{q} \tag{5.3}$$

Here, the covariance matrix contains ranges for pose accuracy and link length accuracy. For values of 0.2 mm (estimated from the accuracy of commercially available 3D image tracking systems), and 1 mm for the pose and link lengths error ranges, the resulting force error range is 1.4×10^{15} N. This large error range is due to the ill-posed nature of the deflection-based force sensing method. The compliance matrix is close to singular in the nominal configuration. This will mean that the $\mathrm{F}_{g,q}$ formulation is not guaranteed to converge if $\mathbf{C}$ is singular. The third method of force sensing, $\mathrm{F}_{g,\tau}$, estimates an even larger error range for the tip wrench with the same values for error range used previously. These results indicate that the $\mathrm{F}_{q,\tau}$ formulation (actuation based) is the best conditioned force sensing approach for our parallel continuum manipulator prototype.

5.1.1 Manipulator Construction

The manipulator consists of six flexible steel spring tempered carbon steel wires (AISI 302/304 stainless steel) with a stated diameter of 1.04 mm. The overall length is 145 mm with a radius of 32.9 mm and an angular offset of 8°. The force sensors are connected to the wires via 3D printed interface parts that transfer the axial force directly to the sensor. The sensors are mounted to a steel slide carriage driven by a Firgelli L16 linear actuator. The linear actuators change the position of each wire base to create 6 DOF motion of the end effector. The design and construction are similar to previous systems (75; 170; 132), but this configuration removes the base platform in order to eliminate friction between the flexible links and the through holes, which can increase error in force estimation. The physical system used in the experiments is shown in Figure 5.1.

5.1.2 Repeatability

The repeatability of the force sensor measurements was evaluated by placing the manipulator in the nominal configuration, and actuating to 8 different positions and then back to the nominal pose while measuring data from the force sensors. This resulted in 9 instances of nominal configuration measurements with 6 load cells each. The average distance from the mean sensor reading in the nominal configuration was 0.15 N for all 6 sensors. This provides an estimation of the repeatability of the force sensors. Note that this measurement does not contain any friction terms due to the lack of a base plate and no sliding contact of the flexible links.

5.1.3 Data Collection

In order to validate the force sensing capabilities of the manipulator, the actuation force applied to each link was recorded with Omega-LC703 load cells. These load cells were rigidly attached to the flexible links and reflect the internal axial force of the link at the proximal end. These measurements are then used as an input, along with the commanded link positions, to the force sensing model ($\mathrm{F}_{q,\tau}$), to calculate an estimate of the external forces applied at the tip of the manipulator. The measurements were taken while the robot was in 9 different positions (nominal, tilted (clockwise and counter-clockwise about the y-axis), twisted ($+z$ and $-z$), translated in the x-y plane ($+x$ and $-x$), and bent (clockwise and counter-clockwise about the y-axis)) with a 300 g calibration weight hanging from the center of the end effector via Kevlar thread. This measurement was taken with the forces applied in the positive x, then the negative y, and finally the negative z directions. This resulted in 27 cases of 3 DOF force application symmetric to the global frame (twisting in the positive z and negative z directions, etc.). In the nominal configuration, the readings from the load cells are assumed to be zero in order to calibrate the sensor readings. The manipulator was actuated to the previously described configurations with the weight hanging freely from the centroid, and measurements from all 6 load cells were taken. Then, the manipulator was returned to the nominal configuration with the weight removed, and measurements were taken again to ensure proper zeroing of the load cells.

5.1.4 Data Analysis

The load cell measurements were collected with an Omega DAQ-USB-2401 system. Each measurement was taken for a minimum of 1 minute at each position to ensure a steady-state reading. The force data signal was filtered with a built-in Butterworth filter in Matlab using the `butter`() command to remove the high frequency noise of the sensor. Once the data was filtered, the zero values were subtracted from the weighted values to find the actuator loads. To analyze the data, the known load was compared to the estimated load calculated using the force sensing algorithm ($F_{q,\tau}$). The absolute value of the difference between the magnitudes of the known load and the estimated load, M_e, and the angular distance between the two vectors, Θ_e, were calculated with the following equations

$$\begin{aligned} M_e &= \left| \|\mathbf{F}_t\| - \|\mathbf{F}_{est}\| \right| \\ \Theta_e &= \cos^{-1}\left(\frac{\mathbf{F}_t \cdot \mathbf{F}_{est}}{\|\mathbf{F}_t\| \, \|\mathbf{F}_{est}\|} \right) \end{aligned} \tag{5.4}$$

where $\mathbf{F}_t$ is the known force of the hanging weight and $\mathbf{F}_{est}$ is the estimated force from the sensing algorithm. The percent error, shown as %, was calculated by dividing the magnitude of the error vector by the magnitude of the known load vector. The results of the force sensing experiments with no calibration are shown in Table 5.1.

5.1.5 Stiffness Calibration

The nominal Young's Modulus for AISI 302/304 is 193 GPa. We measured the diameter of the rods and found agreement with their nominal diameter of 1.04 mm. Thus, the nominal bending stiffness (flexural rigidity) for the links used in this manipulator is 0.0110 Nm^2. To more accurately determine the flexural rigidity, we performed an experimental calibration of the Young's Modulus using a simple cantilevered bending test with a rod of the same diameter and material as the links in the PCR. The rod was clamped at one end with a 16 cm cantilevered length extending horizontally, and weights of 10, 20, 50, and 100 grams were hung from its tip. For each case, we manually measured the tip deflection in the direction of the load. We chose a calibrated E value by minimizing the least squares error between the measured tip deflection and the predicted deflection of the Cosserat rod model. Our calibrated value for E is 161 GPa, which results in a bending stiffness of 0.0092 Nm^2. This value was use to re-evaluate all experimental wrench sensing data, and the results are presented in Table 5.1. While the mean magnitude error of 0.35 N was not

Table 5.1: Force Estimation Experiments

		Nominal EI (EI=0.0110 Nm^2)				Bending Test Calibrated EI (EI=0.0092 Nm^2)			
$\mathbf{F}_t$	Configuration	$\mathbf{F}_{est}$ [N]	M_e [N]	%	Θ_e [	$\mathbf{F}_{est}$ [N]	M_e [N]	%	Θ_e [
[2.94 0 0]	Nominal	[2.97 0.20 0.22]	0.04	1.31	5.69	[2.97 0.20 0.22]	0.04	1.33	5.64
	Twisting	[2.57 -0.21 -0.19]	0.35	12.00	6.19	[2.59 -0.20 -0.19]	0.34	11.63	6.05
		[2.89 0.02 -0.94]	0.10	3.2	18.0	[2.25 0.30 0.22]	0.67	22.65	9.43
	Tilting	[2.39 0.56 0.22]	0.48	16.30	14.05	[2.64 -0.25 -1.74]	0.23	7.95	33.66
		[2.84 0.03 -0.63]	0.04	1.27	12.47	[3.06 0.21 -0.62]	0.19	6.43	12.13
	Translating	[3.04 -0.25 -1.74]	0.57	19.47	30.07	[0.14 -2.72 -0.44]	0.18	6.28	9.73
		[2.26 0.24 1.24]	0.35	11.92	29.20	[0.57 -2.67 0.06]	0.22	7.34	12.14
	Bending	[3.09 0.22 -0.62]	0.21	7.30	12.04	[-0.14 -2.63 -0.22]	0.30	10.12	5.61
		[2.70 0.30 -0.39]	0.19	6.61	10.29	[0.57 -3.13 -0.60]	0.30	10.11	14.84
[0 -2.94 0]	Nominal	[0.14 -2.72 -0.44]	0.19	6.31	9.73	[0.10 -2.34 -0.63]	0.52	17.65	15.31
	Twisting	[0.57 -2.68 0.06]	0.20	6.85	12.10	[-0.03 0 -2.82]	0.12	4.11	0.56
		[-0.15 -2.57 -1.39]	0.02	0.60	28.54	[-0.01 0.10 -2.45]	0.49	16.77	2.33
	Tilting	[-0.35 -2.65 -0.22]	0.26	8.99	8.87	[-0.25 0.47 -2.95]	0.06	1.91	10.25
		[0.47 -2.51 -1.37]	0.04	1.43	29.97	[0.81 -0.35 -3.56]	0.73	24.80	13.94
	Translating	[0.99 -3.17 -0.60]	0.43	14.67	20.08	[-0.32 0.04 -3.42]	0.49	16.57	5.41
		[-0.77 -2.18 0.84]	0.49	16.56	27.60	[2.89 0.04 -0.94]	0.10	3.37	17.97
	Bending	[0.12 -2.33 -0.63]	0.52	17.79	15.42	[2.63 0.02 -0.63]	0.24	8.03	13.40
		[0.23 -1.95 -0.43]	0.93	31.61	14.07	[2.67 0.23 1.24]	0.01	0.44	25.32
[0 0 -2.94]	Nominal	[-0.03 0.00 -2.82]	0.12	4.11	0.56	[2.71 0.28 -0.39]	0.19	6.43	10.12
	Twisting	[-0.02 0.12 -2.45]	0.49	16.74	2.76	[-0.15 -2.59 -1.39]	0	0.13	28.33
		[0.33 -0.04 -2.78]	0.14	4.81	6.72	[0.26 -2.50 -1.37]	0.08	2.68	29.15
	Tilting	[-0.44 0.51 -2.95]	0.08	2.89	12.91	[-0.36 -2.18 0.84]	0.58	19.59	22.73
		[0.57 -0.01 -2.88]	0.01	0.38	11.17	[0.24 -1.93 -0.43]	0.95	32.27	14.25
	Translating	[1.20 -0.37 -3.56]	0.84	28.45	19.44	[0.32 -0.03 -2.78]	0.14	4.83	6.63
		[-1.06 0.23 -1.33]	1.22	41.62	39.13	[0.37 0.01 -2.88]	0.04	1.46	7.31
	Bending	[-0.31 0.04 -3.42]	0.49	16.55	5.28	[-0.66 0.23 -1.33]	1.44	48.89	27.62
		[0.28 0.29 -3.60]	0.68	23.00	6.51	[0.29 0.28 -3.60]	0.68	22.97	6.40
		Max	**1.22**	**41.62**	**39.13**	**Max**	**1.44**	**48.89**	**33.66**
		Mean	**0.35**	**11.96**	**15.14**	**Mean**	**0.35**	**11.73**	**13.56**
		Median	**0.26**	**8.99**	**12.47**	**Median**	**0.23**	**7.95**	**12.13**

improved by the calibration, the mean directional error was improved by 1.5°. The relatively low change in the error statistics in response to a 17% change in E suggests that actuation-based wrench estimates are actually not very sensitive to the value of E. In contrast, deflection-based wrench estimates would vary linearly with E.

5.1.6 Results

The median difference in the magnitudes between the estimated force and the known force was 0.26 N in the uncalibrated data set and 0.22 N in the calibrated data set. Since this is higher than our estimated error of 0.08 N based on sensor resolution, other errors in construction and load application likely affected the measurement of the actuation loads and the force estimation. The median directional error in the uncalibrated data set was 12.47° and 12.09° in the calibrated data set. The highest errors occurred in the case of pure translation. Possible sources of error in force estimation include inaccuracies in the specification of the nominal link lengths and/or positional inaccuracies of the linear motion system, and mechanical tolerances in the construction of the manipulator and linear motion system. The linear actuators have a backlash of 0.5 mm and the linearity of the potentiometer is less than 2%. Other sources include elastic deformation of the end effector plate, which is assumed to be a rigid body in the model, and the potential small plastic deformation of the links.

5.2 Passive Stiffness Control

The goal of a stiffness controller is to provide a command to the robot that incorporates the sensed tip force and changes the robot's stiffness. In the case of a PCR this could be a change to the actuation variable commands ($\mathbf{q}$) or the actuation forces ($\boldsymbol{\tau}$). Here we present a stiffness controller that could be formulated to provide outputs of either variable.

The stiffness controller utilizes a single solve of the inverse kinetostatics formulation (inputs of pose and wrench with outputs of actuation variables and actuation forces) and the manipulator matrices (see Section 3.5) to solve for a desired proportional control gain between the actuation forces and the link translations. The general control law is given as

$$\boldsymbol{\tau} = \boldsymbol{\tau}_d - \mathbf{K}_p(\mathbf{q} - \mathbf{q}_d) \tag{5.5}$$

where $\boldsymbol{\tau}$ are the actuation forces on the robot links, $\boldsymbol{\tau}_d$ are the desired actuation forces based on the inverse kinetostatics solution, $\mathbf{K}_p$ is the desired proportional control gain of the controller, $\mathbf{q}$ are the link lengths of the robot, and $\mathbf{q}_d$ are the desired link lengths. The goal of this controller is to supply a $\mathbf{K}_p$ matrix such that the manipulator will change its configuration based on the applied force at the tip. The control law

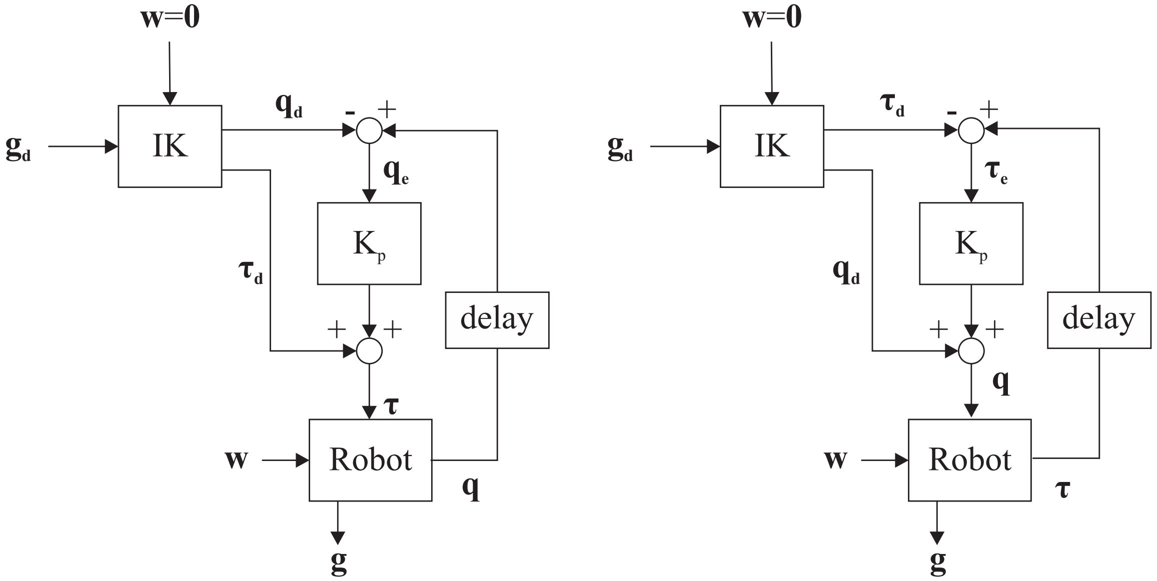

Figure 5.2: This passive stiffness controller takes in a commanded pose from the master and solves the inverse kinetostatics formulation assuming a zero load on the manipulator. The desired and current actuation forces or link lengths are multiplied by the $\mathbf{K}_p$ matrix and added to the desired link lengths or actuation forces from the inverse kinetostatics, respectively. Either of these outputs can be commanded to the robot depending on the actuation strategy.

can be used to change inputs of link lengths (desirable for linear actuators with potentiometer feedback on motor location) or actuation forces (desirable for torque control DC motors). In order to select the appropriate $\mathbf{K}_p$ for a desired output compliance, we can rewrite the control law in the following way,

$$\delta\boldsymbol{\tau} = -\mathbf{K}_p\delta\mathbf{q} \tag{5.6}$$

By substituting this expression into Equation 4.1, we can solve for $\mathbf{K}_p$ in terms of a desired output compliance, $\mathbf{C}_d$. We substitute the control equation into the relationship between actuation forces, actuation variables and wrench as follows,

$$-\mathbf{K}_p\delta\mathbf{q} = \mathbf{K}\delta\mathbf{q} + \mathbf{W}\delta\mathbf{w} \tag{5.7}$$

Collecting coefficients for $\delta\mathbf{q}$ leads to the following,

$$(-\mathbf{K}_p - \mathbf{K})\delta\mathbf{q} = \mathbf{W}\delta\mathbf{w}. \tag{5.8}$$

Solving for $\delta\mathbf{w}$ and substituting into the relationship between pose, actuation variables and wrench provides the following,

$$(\mathbf{g}_e^{-1}\delta\mathbf{g}_e)^{\vee} = \mathbf{J}[(-\mathbf{K}_p - \mathbf{K})^{-1}\mathbf{W}]\delta\mathbf{w} + \mathbf{C}\delta\mathbf{w} \tag{5.9}$$

This leads to a new matrix relating pose and wrench that is a function of the kinetostatics matrices and a gain matrix as follows,

$$\mathbf{C}_d = \mathbf{J}[(-\mathbf{K}_p - \mathbf{K})^{-1}\mathbf{W}] + \mathbf{C} \tag{5.10}$$

We can solve this equation for $\mathbf{K}_p$ given by,

$$\mathbf{K}_p = -\mathbf{K} + [\mathbf{J}^{-1}(\mathbf{C}_d - \mathbf{C})\mathbf{W}^{-1}]^{-1} \tag{5.11}$$

This will allow us to specify a desired compliance behavior and solve for a gain matrix for the actuation forces related to the actuation variables. A control diagram is show in Figure 5.2 for both options. The inverse kinetostatics formulation takes in the commanded pose from the controller ($\mathbf{g}_d$) with an assumed zero load on the manipulator ($\mathbf{w} = \mathbf{0}$) and outputs the desired link lengths and actuation forces. The difference between the sensed or measured variable ($\mathbf{q}$ or $\boldsymbol{\tau}$) is multiplied by the proportional controller gain and added to the control variables which are provided to the manipulator. In the following results the general control law was solved for $\mathbf{q}$.

5.2.1 Simulation Results

The following simulation results were produced with a inverse kinetostatics formulation (inputs of pose and wrench) to initialize $\mathbf{q}$ and $\boldsymbol{\tau}$ along with the matrices needed

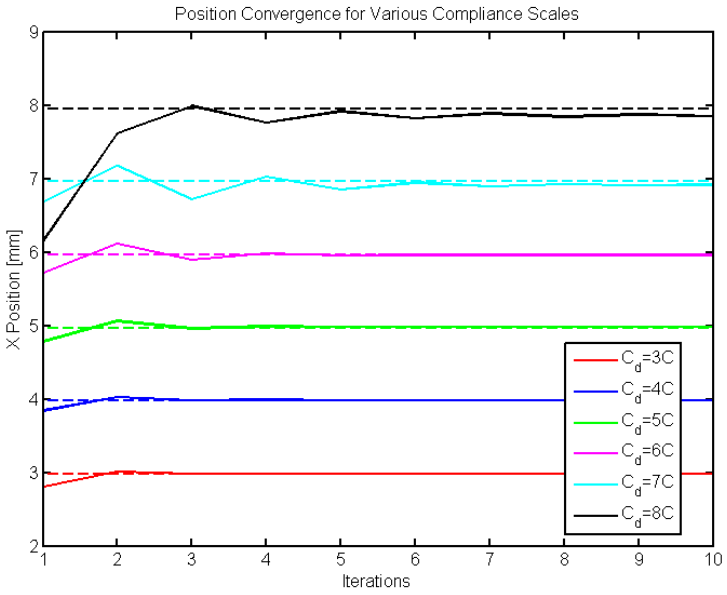

Figure 5.3: The desired compliance of the manipulator was scaled from $\mathbf{C}_d = 3\mathbf{C}$ to $\mathbf{C}_d = 8\mathbf{C}$ and a constant force of 1.1 N was applied on the end effector in the positive x direction. Different simulations for the desired compliance matrices are shown here.

for calculation of $\mathbf{K}_p$. A forward kinetostatics formulation (inputs of $\mathbf{q}$ and wrench) was used to apply a force to the end effector and measure the displacement.

Passive Stiffness Controller Position Convergence

The passive stiffness controller solves for new actuation forces or link lengths with a constant $\mathbf{K}_p$ matrix based on the current pose of the manipulator. The convergence of the controller onto the correct pose for the desired stiffness is measured in the number of times the robot plant model is provided new actuation variables and solved for the pose. The figure shows results for 6 different desired stiffness behaviors and the position convergence for each was simulated with a robot plant in the form of a forward kinetostatic model. Results are shown in Figure 5.3. The dotted line represents the displacement desired when the force is placed on the end effector. This is calculated by multiplying the x component of the $\mathbf{C}_d$ matrix (the first diagonal) by the applied force. It is important to note that for the first 5 simulations the control law is simply Equation (5.5). In the simulation with $\mathbf{C}_d = 8\mathbf{C}$, an additional damping term is required for convergence. The control law is of the form

$$\boldsymbol{\tau} = \alpha(\boldsymbol{\tau}_d - \mathbf{K}_p(\mathbf{q} - \mathbf{q}_d)) + (1 - \alpha)\boldsymbol{\tau}_{old} \tag{5.12}$$

where $\boldsymbol{\tau}_{old}$ is the previous input to the robot plant.

All of the simulations produced actuation forces of less than 3 N. This demonstrates that the control law is achievable with modest motor effort.

Chapter 6

Continuum Robot Tool Manipulators for Colonoscopy

In chapters 3 and 4, kinematic modeling and design analyses of continuum robots were developed. These results provide the means by which to analyze a particular concentric tube robot for a surgical task. This chapter outlines the task goals and requirements, development of a robotically enhanced colonoscope, challenges with actuation via a long transmission section of the colonoscope, and the resulting design and construction of a prototype sufficient for bench-top evaluation.

Colonoscopy is a procedure where a colonoscope (endoscope specifically sized for the colon) is introduced via the rectum and navigated by a surgeon to view and sample patient tissue to test for abnormal or cancerous growths. A standard colonoscope has a light source, a camera, air ports that insufflate, or pump air into, the colon, and tool channels. These tools channels are used to introduce a variety of components into the working area of the colonoscope which is defined by the field of view of the camera. Currently, these tools are extremely flexible with only 2 degrees of freedom (insertion and grasping). The flexibility of these tools increases the difficulty of complex tissue removal. Surgeons have to manipulate the entire colonoscope in order to change the direction and reach of these tools. Moving the scope in this way increases the risk to the patient for tissue damage or even perforation. The goal of the continuum robot tool manipulators is to increase the dexterity of the currently available tools and allow for complex tool manipulation without moving the colonoscope. The design requires incorporation of current tools and minimal changes in colonoscope functionality.

Due to the size constraints and the need for an open lumen with which to pass currently available tools, concentric tube robots are the most logical choice for the tool manipulator. As previously described, these robots consist of flexible pre-curved tubes that are routed concentrically. The most suitable material is super-elastic Nitinol due to it's high elastic stress-strain range and the ability to set pre-curved shapes with relative ease.

6.1 Design Specifications

A literature review of the relevant anatomy and surgical techniques provided insight into the workspace and force requirements needed for the physical guidelines and constraints of the colon. Specifically, we have established (1) a volumetric representation of the desired workspace that our instrument manipulator design must exhibit, (2) a stiffness requirement specifying the maximum allowable deflection that the instruments can exhibit under typical forces during submucosal dissection, (3) size constraints on the instrument manipulators such that they can be deployed through tool-port channels in currently available endoscopes, and (4) an accuracy requirement for effective surgical teleoperation.

Workspace Volume: The colon is approximately 130-150 centimeters long and 5 centimeters wide on average (188; 189). Since the desired operation is with a stationary colonoscope tip, the desired workspace for the tool manipulators needs to cover the largest local stage lesions encountered. We estimate that this workspace is 4-6 centimeters in diameter and 8-10 centimeters in length. This cylindrical volume will be the desired workspace specification for our endoscopic robot.

Forces and Stiffness: The force application required during endoscopic submucosal dissection consists of applying traction to displace the mucosal and submucosal layers away from the musculature in order to dissect the tissue. This pull force has been measured on average to be 2.5 Newtons with a maximum of 5 Newtons (177). The force required for perforation of the colon wall has also been measured and has a great degree of variability based on the location and tissue condition. In a study with porcine bowel segments, the perforation force averaged 13.5 Newtons with a range of 7-19 Newtons (190). Considering these force magnitudes and the small scale of the procedure, we can specify a desired tool displacement of less than 1 millimeter per 5 Newtons of force. Therefore, the output stiffness requirement for our robot will be 5 N/mm.

Tube Sizes: A standard colonoscope measures 1700 mm in length, 11-15 mm in diameter and has 1-2 working channels for tools. These tool ports measure between 2.8 and 4.2 mm with most measuring around 3.8 mm (191). This measurement will dictate the sizes of our concentric tubes.

Accuracy: We can specify the required positional accuracy of the robot based on the suggested negative margins (amount of normal tissue removed along with cancerous tissue) of 2-5 mm to decrease the recurrence of cancerous lesions (192). Based on this margin requirement, a reasonable accuracy goal for our robot's end-effector position is less than 1 mm.

6.2 Instrument Manipulator Design

The main requirements of the manipulator design are: (1) increase the workspace, dexterity and stiffness of colonoscopic tools, (2) incorporation of existing colonoscopic tools without the need for a specifically manufactured robotic manipulator for each tool, (3) minimize the increase in flexural rigidity of the colonoscope, and (4) actuate

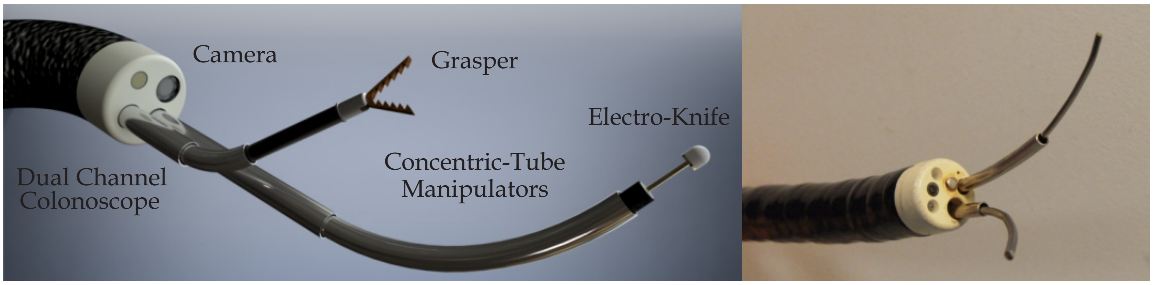

Figure 6.1: Concentric tube manipulators can be deployed down the tool channels of existing colonoscopes.

robotic tool manipulators without moving the colonoscope. This will allow for the system to function in a "drive-park-and-move" paradigm (193) where the field of view is stabilized and multi-degree-of-freedom instrument manipulation occurs independent of the colonoscope tip. This will allow the surgeon to easily apply sufficient traction to tissue, excise and cauterize from a range of incidence angles *without ever moving the colonoscope tip*, thus eliminating the burden of non-intuitive tool motion. This will decrease the counter-intuitive movement seen with manual colonoscope tools and tortuous colon paths (33).

There are two design cases to consider for the deployment of the concentric tubes: (1) down the tool channels of the colonoscope, and (2) down additional tubes attached outside the colonoscope. The subsequent discussion will consider the first case. In order to increase the dexterity of the tools, 3 concentric tubes is the most desirable configuration. This will provide 6 DOF for the manipulator of the colonoscopic tools. The workspace of a 3 tube concentric tube robot is examined below and compared to the colon and field of view of a standard colonoscope.

6.2.1 Deployed Inside the Colonoscope

Deploying the concentric tube manipulators inside the colonoscope (see Figure 6.1) is desirable because no modifications are required for the colonoscope and no additional space is added to the colonoscope diameter. Here we describe the analysis conducted

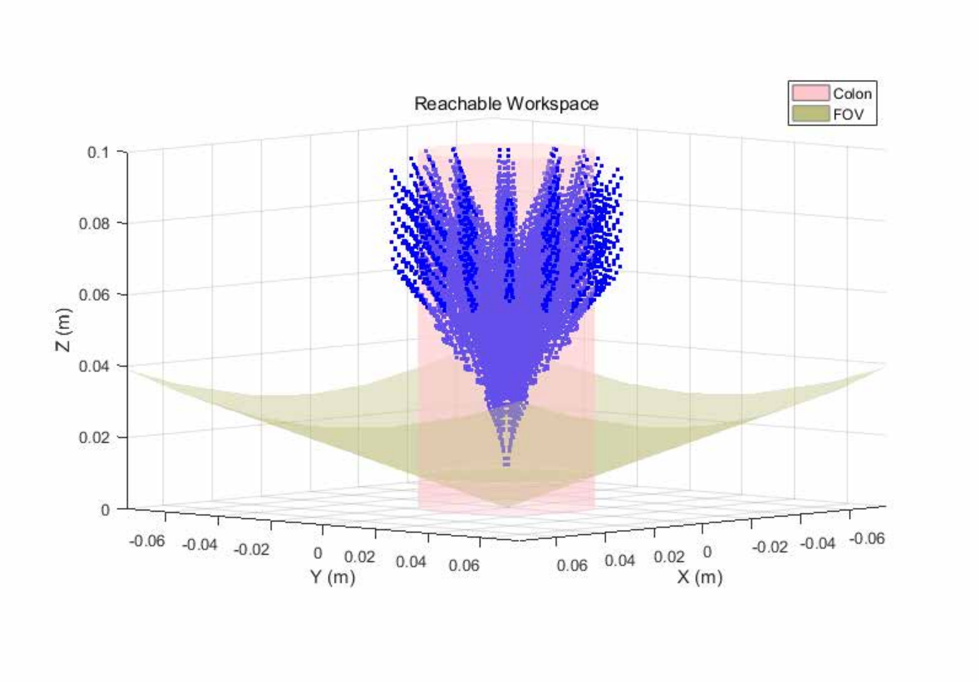

Figure 6.2: The workspace of the concentric tube manipulator with an overlay of the colon in pink and the field of view of the colonoscope in gray.

for this design case. It uses three solid concentric tubes that are between 5.5 and 6 feet long to span the entire length of the colonoscope.

Workspace

We determined the reachable workspace of the manipulator by uniformly sampling the 5-DOF actuation space with a resolution of 2 mm in translation and 30 degrees in

Table 6.1: Manipulator design parameters for workspace simulation.

Tube	**OD** (mm)	**ID** (mm)	**Pre-Curvature** (m^{-1})	**Pre-Curved Length** (mm)	**Distal Straight Length** (mm)
Inner	2.54	2.25	40	20	0
Middle	2.87	2.57	35	25	20
Outer	3.43	2.92	0	0	45

rotation, resulting in a total of 16,000+ points. At each sampled point, the forward kinetostatics was solved within the user defined tolerance. The point cloud in Figure 6.2 represents the set of Cartesian coordinates that the robot could possibly reach. This set was generated using the design parameters found in Table 6.1. An iterative simulation process was performed in order to characterize the effect of the other design parameters. Early in the design process, it was discovered that outer tubes with any pre-curvature greatly reduced the reachable workspace within the colon wall. This is because the overlap constraint (see Section 3.9) has an accumulating effect on the length of distal straight sections for outer tubes, and reveals a trade-off introduced by the overlap constraint. Therefore, we limited designs to have straight outer tubes. Then, increasing pre-curvature and pre-curved lengths of the middle and inner tubes yielded workspaces with increasingly better coverage, but diminishing spatial resolution. The reachable workspace shown in Figure 6.2 extends beyond the simulated bounds of the colon (in pink), but all points are still within the 140 degree field of view of the colonoscopic camera (in green).

Stiffness Analysis

Once the workspace of the concentric tube robot is established, the stiffness of the manipulator at the edge of the colon (where most procedures take place) needs to be measured to ensure the appropriate amount of force can be applied to the tissue. It is important to note that the workspace result directly affects the predicted force capability of the end effector at the colon wall, since the stiffness calculation is computed at a particular point in the workspace where the colon wall intersects. It is then logical to first choose designs which meet workspace and then further evaluate them for force capability. The design highlighted in Figure 6.2 was chosen for further stiffness analysis because it yielded a workspace with sufficient coverage.

Two distinct stiffness properties are considered in this analysis. The end effector stiffness of the manipulator at the boundary of the workspace is used to analyze the force capability of the manipulator. The bending stiffness of the collection of proximal

Table 6.2: Computation of end effector force capability at colon wall with all tube sections made of Nitinol.

Distance to Colon Wall $[N/mm]$	**Minimum Singular Value** $[mm]$	**Minimum Force Output** $[N]$
0.0378	24.6	0.930
0.0343	28.4	0.974
0.0367	25.1	0.921
0.0427	20.4	0.871
0.0378	24.5	0.929

tube transmission segments is also examined and compared with the bending stiffness of a standard colonoscope. For the current case, this would be the three Nitinol tubes given in Table 6.1. It is desirable that the transmission section of the robot, which lies inside the colonoscope, does not significantly add to the overall bending stiffness in the system and thereby hinder navigation of the colon. The colonoscope bending stiffness is not specified by the manufacturer and was approximated through a series of bending tests.

End Effector Stiffness

Using the kinematics model described in Section 3.9, we can compute the robot end effector stiffness at any reachable workspace point. Several representative points near the workspace boundary were chosen to measure the stiffness in regions critical to colon wall procedures. Small forces were applied to the end effectors at these points and the resulting deflection was recorded for finite difference approximation of the stiffness matrix. In order to ensure that the manipulator can achieve the required forces for the procedure, we can compute the minimum singular value of the stiffness matrix at each point, and the distance between the point and the nearest point on colon wall. This allows us to express a conservative estimate of the force capability as the force applied by the end effector at the colon wall in the *least* stiff direction. Table 6.2 contains the results of these computations. The average output force is 0.925 N, which does not meet the desired surgical value, but does not suggest total

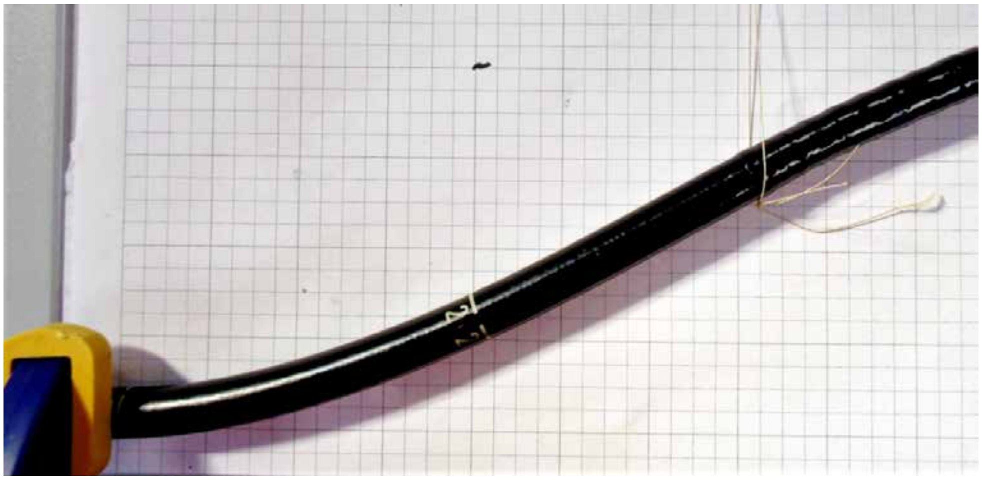

Figure 6.3: Colonoscope bending stiffness experiment.

infeasibility. Note that our simulation study places the endoscope at the center of the colon channel. One way to increase the force capacity is to move the endoscope closer to the wall during operation, thus providing a larger range of possible end-effector forces.

Colonoscope Bending Test

In order to define a maximum permissible bending stiffness for the robot transmission section, a simple experiment was performed to approximate the bending stiffness of the colonoscope. The experimental setup is shown in Figure 6.3. We use the same rod model introduced in Section 3.9 to describe the shape of a section of the colonoscope as a cantilevered elastic rod, where we assume that the colonoscope exhibits linear elastic deformation under load, excluding the actuated distal section. Using a spring-scale with a digital read-out, we apply a load in the x direction to the end of the bending section of the colonoscope. The opposite end of this section is fixed using a clamp. Since the experiment is performed on a flat surface, the effect of gravity is negligible. By measuring the deflection of the colonoscope at the location of the load, we can solve the boundary value problem of static equilibrium by guessing the bending stiffness EI of the colonoscope along with the values of the unknown

Table 6.3: Colonoscope bending test data.

L (m)	**Applied Force** (kg)	**Deflection** (m)	**EI** (Nm^2)
0.1	0.25	0.003	0.0307
0.1	0.40	0.040	0.0274
0.1	0.56	0.050	0.0272
0.2	0.08	0.067	0.0276
0.2	0.14	0.107	0.0238
0.2	0.25	0.140	0.0211
0.2	0.30	0.150	0.0196
0.3	0.08	0.165	0.0271
0.3	0.13	0.197	0.0307
0.3	0.19	0.227	0.0256

state variables at the cantilevered end. The results of this experiment are shown in Table 6.3. Three segments of different length were tested using varying applied forces. The values of EI vary in the range of $0.02 - 0.03$ Nm^2, with the average being 0.0261 Nm^2. The inconsistency in these values can be attributed to unknown elastic behavior of the colonoscope, as it is not composed of uniform material. The results are used to establish an approximate specification for the stiffness of endoscopic robot transmissions. This value is compared to the combined bending stiffness of all three Nitinol tubes in parallel equaling 0.3125 Nm^2. This result indicates that the manipulator will require a significantly more compliant transmission section in order to decrease the overall bending stiffness that is added to the colonoscope.

Notched Transmission Approach

In order reduce the bending stiffness inside the colonoscope, we modeled a manipulator with a transmission made of structurally modified stainless steel tubes, which are joined to Nitinol sections at the distal end. The stainless steel tubes have a Youngs Modulus of around 200 GPa (an increase by a factor of 3 from the Nitinol tubes). In order to decrease the bending stiffness, these tubes will be notched with a pattern similar to the one studied in (194). Figure 6.4 depicts a solid model of

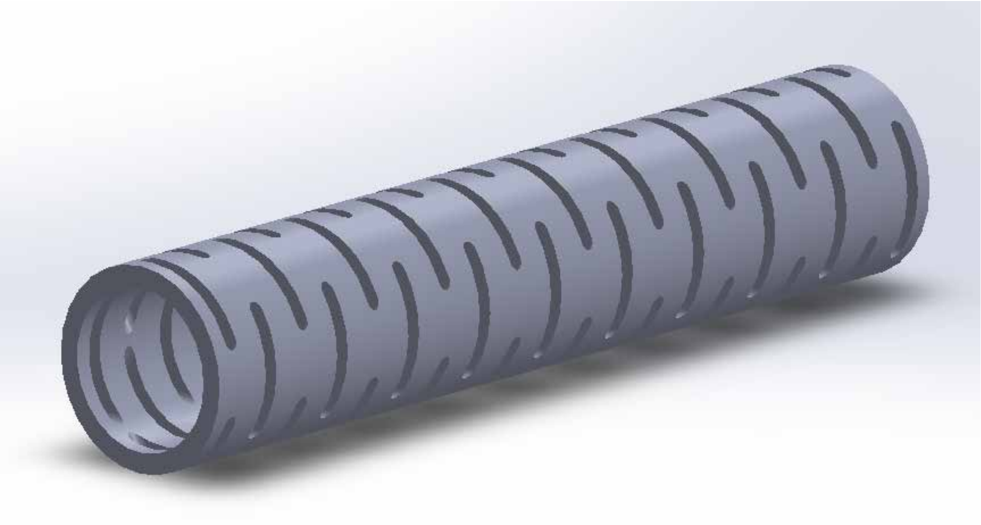

Figure 6.4: A solid model of a stainless steel notched tube design for the robot transmission, based on the work done Lee et. al(194).

a representative notched tube, for which we determined stiffness values by applying finite element analysis to designs of this type under defined loading. We chose the finite element method over the analytical solution of calculating the I values of each of the sections of the tube and adding them together like springs in series. The finite element method is required due to the Saint-Venant's Principle stating that the difference between the effects of two different but statically equivalent loads becomes very small at sufficiently large distances from load. The springs are small enough that the load applied to them is no longer statically equivalent. This particular design was shown to decrease bending stiffness while maintaining a relatively high torsional stiffness. The notches were designed so that the bending stiffness of the colonoscope is only increased by 50% due to the stainless steel transmission tubes. This approach was then analyzed for force capability using the computation approach discussed in Section 6.2.1. The results are stored in Table 6.4, and the average output force is 0.871 N. Therefore, while this design meets the requirement of not adding to the bending stiffness of the colonoscope, it still does not have sufficient stiffness at the tip to perform surgical tasks.

Table 6.4: Computation of end effector force capability at colon wall with a notched stainless steel transmission.

Distance to Colon Wall (N/mm)	**Minimum Singular Value** (mm)	**Minimum Force Output** (N)
0.0403	21.7	0.875
0.0391	22.2	0.868
0.0456	20.3	0.926
0.0388	23.8	0.923
0.0428	17.8	0.762

Subsequent Transmission Design

Since both the all Nitinol transmission section and the notched stainless steel transmission section do not provide the needed tip stiffness, other designs should be considered. The accuracy and machining time required to notch stainless steel tubes along with the length of the sections needed to reach the end of the colonoscope also make these components cost-prohibitive. Another option for the transmission section design is coil pipe made from stainless steel. This is a tightly wound sheath that is very flexible. These are the components used inside the actual colonoscope for the tool channels. This means that they will not add too much stiffness to the colonoscope. However, these coils are unsuitable for torque transmission due to their ability to un-wind when twisted.

The current design uses a Helical Hollow Strand® Tube from Fort Wayne Metals (see Figure 6.5). This tube is described as a single strand tube with single, double, or triple layers of strand wrappings at pitches of left, right, unidirectional and reverse. Materials are mostly tempered steel but Nitinol and Platinum alloys are also possible. The benefits of this type of component are the very low bending stiffness and the high degree of torsional transmission that is possible when double strands with opposing pitches are selected. This eliminates un-winding of the coil since the strands are joined together.

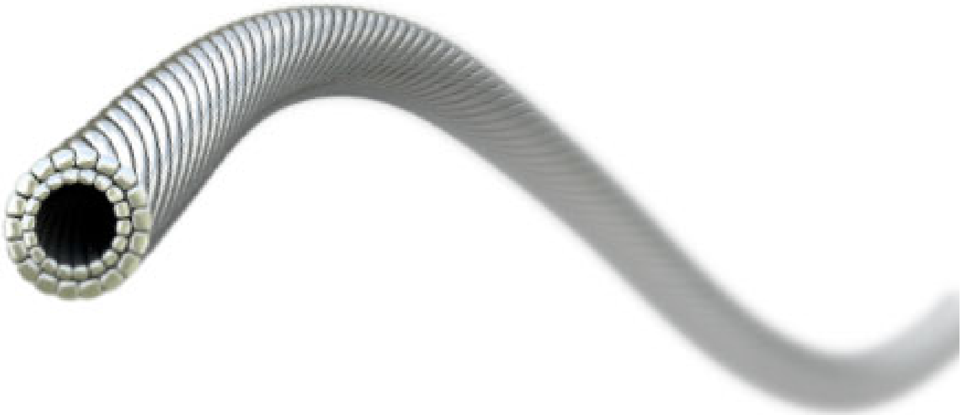

Figure 6.5: A double layer, left and right pitch Helical Hollow Strand® Tube from Fort Wayne Metals.

6.2.2 Deployed Outside the Colonoscope

The main challenge of deploying the concentric tubes down the colonoscope is the added thickness of the concentric tubes. The ones previously described do fit inside the colonoscope. However, they require the use of much smaller tools than are usually employed during colonoscopic procedures. For this reason, it is important to explore deploying the tubes outside of the colonoscope.

In this design (see Figure 6.6), two flexible polytetrafluoroethylene (PTFE) tubes are mounted to the outside of the colonoscope near the tool channel openings. These tubes provide a low friction transmission channel to hold the manipulators and are also flexible enough to add no additional stiffness to the colonoscope. The channels measures 5.5 mm in diameter. They are mounted so that their centerlines are not co-linear. Each instrument manipulator consists of two flexible concentric tubes, where the inner and outer tube is pre-curved, providing four degrees-of-freedom for each instrument manipulator. The transmission sections are double layer HHS®tubes.

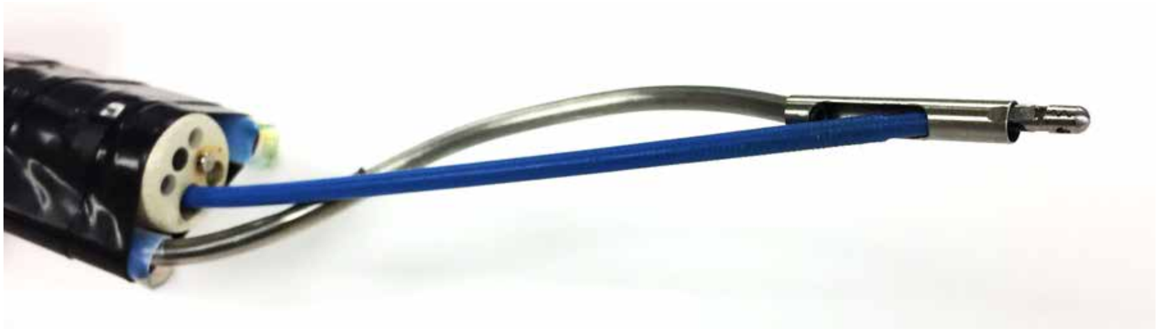

Figure 6.6: The colonoscope is fitted with two additional PTFE channels. Concentric tube manipulators are deployed down the channels. The standard colonoscopic tools are deployed down the tool channel and then captured by the concentric tube manipulators.

6.2.3 Actuation Module Design

We made several design choices for the actuation system to achieve compactness, modularity, and accuracy. The core of the mechanical design takes advantage of the inherent collinearity of nested concentric tubes by aligning the actuation of all six joint variables on one guide rail. Hollow-shaft stepper motors serve as actuators that allow the rotation of each tube to be driven directly, without gearing, while at the same time allowing several tubes to pass through the center of its frame. We used six Nanotec NEMA 17 stepper motors to drive the translation and rotation of each tube. The motors are rated for up to 25 N-cm in our desired speed range, greater than the loads necessary to actuate the robot by a factor of 10-20. This ensures the motors will not miss steps due to high load torques. We arranged the motors on a cart and guide rail system as shown in Figure 6.7. The carts and rail are THK-SSR series caged-ball linear motion guides. Each cart carries two motors: one which is threaded onto a stationary lead screw to drive the linear motion of the cart, and one which grips and rotates a concentric tube. Since the carriage sub-assembly can be duplicated for each concentric tube in a given design, assembly and disassembly of multiple tube designs is straightforward and time efficient. The system is easily modified for use in a variety of continuum manipulators, since many existing robot designs require prismatic and revolute joint motion aligned on a single axis.

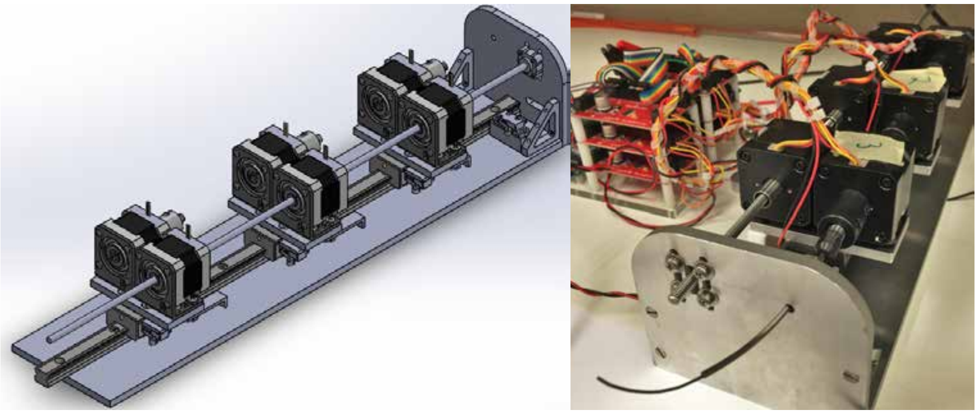

Figure 6.7: The actuation module consists of three dual motor carriages that translate and rotate the pre-curved concentric tubes while maintaining an accurate and rigid actuation platform.

Our stepper motors are driven by L6470 AutoDriver boards from Sparkfun. They offer an advantage in low-level access to motor commands, have relatively large electrical capacities, and are inexpensive. Each driver can be sent commands through SPI communication, reducing time and wiring complexity. The boards are controlled through the serial communication pins of an Arduino Uno. The AutoDrivers are able to receive motion commands and execute them independently while monitoring current level. Because the step counter for each motor is offset by the initial position at startup, we designed a zeroing scheme that makes use of limit switches mounted on the carriages. The switches are wired in parallel with distinct resistors and then connected to a single analog input on the Arduino.

Resolution Analysis

We measured positional accuracy by computing the resolution of the instrument tip using the minimum step angle specification of 1.8 degrees for each motor, which converts to 0.025 mm of translation through the lead screw. More precision is possible through microstepping, but for preliminary analysis we consider motor control to be without this capability. The computation for the resolution shown in Figure 6.8 was performed for the same tube set design analyzed in Section 6.2.1. In order to show

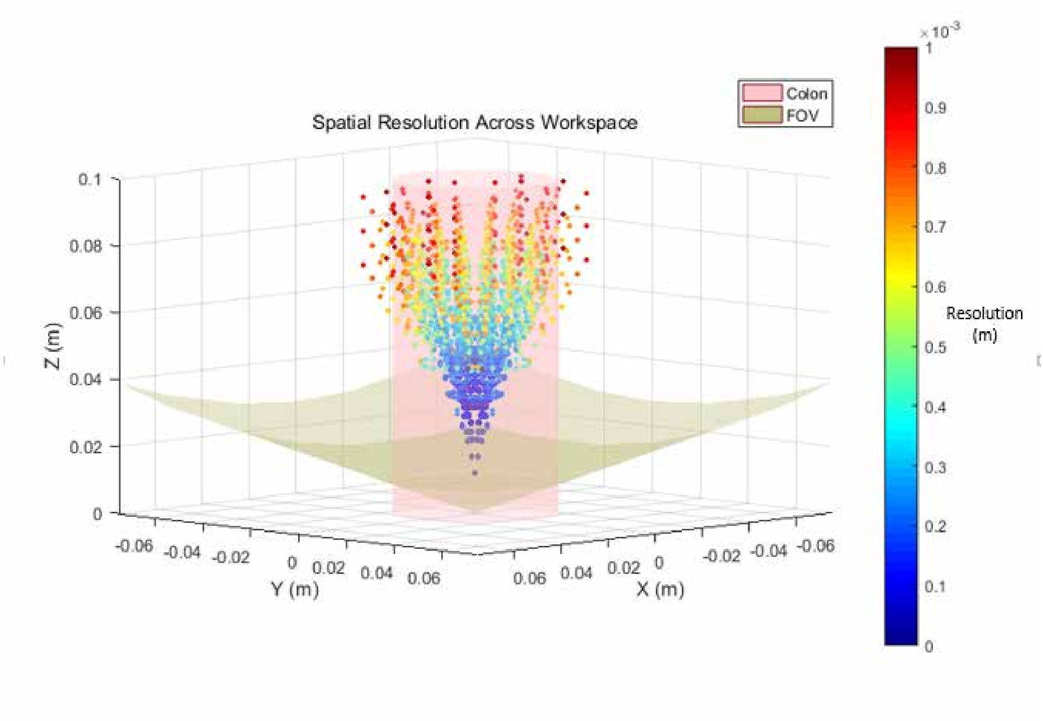

Figure 6.8: The spatial resolution of the end effector is represented as the color of each point in the workspace.

end effector spatial resolution across the workspace, we sampled the actuation space to find an initial set of 3600 nominal manipulator configurations. For each point in this set, 5 *additional* points were solved corresponding to a minimum step by each actuator away from the nominal point. Then, we calculated the maximum Euclidean distance that the end effector could travel away from the nominal configuration by referencing the subspace bounded by the 5-point subset. This maximum Euclidean distance represents a measure of spatial resolution in that it defines an upper bound on the end effector displacement that is caused by minimum actuator steps. Figure 6.8 shows a workspace point cloud, in which the color represents the spatial resolution.

Chapter 7

Conclusions and Future Work

This dissertation has presented several contributions in the growing field of continuum robots. The generalized modeling of parallel continuum robots presented in Chapter 3 to account for joint types, base plate configurations and various inputs and outputs will provide a foundation for future analysis in design and manipulator capabilities. The manipulator analysis methods presented in Chapter 4 allow for substantial quantitative study of a continuum robot's ability to complete certain tasks. The force sensing and control methodologies presented in Chapter 5 will provide enhanced feedback signals and safety to a new line of robotic manipulators. Finally, the prototype concentric tube tool manipulators for a colonoscope presented in Chapter 6 will provide the basis for a bench-top user trial and subsequent clinical evaluations for an enhanced surgical system.

7.1 Future Work in Parallel Continuum Robot Modeling and Analysis

The next step in modeling of PCRs is to explore the capabilities of robots with different leg designs. Currently, work is being done on a forward kinetostatics formulation with 3 links instead of 6 like in the Stewart Gough configuration. This modeling is fairly simple for inputs of actuation variables and wrench (the standard forward formulation). However, the inverse formulation (inputs of pose and wrench) is limited due to the decrease in the number of equations. This limitation is currently being explored by including the Euler angles of the end effector rotation matrix as unknowns in order to balance out the number of equation and unknowns.

Another area of exploration is adding twisting of the flexible links as an actuation variable. In this case as well, the forward kinetostatics model is fairly straight forward. However, more research is needed to formulate the inverse formulation. All of these design variations will need to be analyzed to see how the change the capabilities of the manipulator.

7.2 Future Work in Stiffness Control

The work done in the control of PCRs seeks to impact safe, robot-assisted rehabilitation of the wrist, specifically flexible rehabilitation for patients who have suffered from injury or stroke. Studies have proven that these patients can recover faster with training directed toward improving strength and motor control, relearning sensorimotor relationships and improving functional performance. This training can be further enhanced with haptic feedback from a mechanical device such as the RiceWrist (195). The future work of stiffness control will be to increase the safety and effectiveness of this device by applying PCRs in collaboration with Dr. Marcia O'Malley at Rice University. The flexible nature of this design will allow for use in more fragile patient populations like the elderly who are more likely to suffer from strokes.

7.3 Future Work in Tool Manipulators for Colonoscopic Surgery

In order to evaluate the prototype robotic manipulators presented in this dissertation, input devices and testing environments will be constructed to simulate the surgical task. The first testing structure should be a cylindrical structure (clear plastic tubing for example) in which a robotic manipulator can perform common laparoscopic tasks. Subsequent test beds would need to be comprised of tissue phantom arranged in an anatomically correct jig. These structures will provide preliminary testing for the prototype prior to ex vivo trials.

Bibliography

[1] H. Chen, S. Stavinoha, M. Walker, B. Zhang, and T. Fuhlbrigge, "Opportunities and challenges of robotics and automation in offshore oil & gas industry," *Intelligent Control and Automation*, vol. 2014, 2014. 1

[2] K. Qian, A. Song, J. Bao, and H. Zhang, "Small teleoperated robot for nuclear radiation and chemical leak detection," *International Journal of Advanced Robotic Systems*, vol. 9, 2012. 1

[3] J. Rosen, B. Hannaford, and R. M. Satava, *Surgical Robotics: Systems Applications and Visions*. Springer Science & Business Media, 2011. 1, 23, 24, 72

[4] R. A. Beasley, "Medical robots: current systems and research directions," *Journal of Robotics*, vol. 2012, 2012. 1

[5] J. Burgner-Kahrs, D. C. Rucker, and H. Choset, "Continuum robotics for medical applications: A survey," *Robotics, IEEE Transactions on*, vol. unknown, no. unknown, p. unknown, 2015. 1, 7, 8

[6] C.-H. Kuo, J. S. Dai, and P. Dasgupta, "Kinematic design considerations for minimally invasive surgical robots: an overview," *The International Journal of Medical Robotics and Computer Assisted Surgery*, vol. 8, no. 2, pp. 127–145, 2012. 1, 6, 72

[7] M.-A. Vitrani, C. Poquet, and G. Morel, "Applying virtual fixtures to the distal end of a minimally invasive surgery instrument," *IEEE Transactions on Robotics*, 2016. 2

[8] A. Hussain, A. Malik, M. Halim, and A. Ali, “The use of robotics in surgery: a review,” *International journal of clinical practice*, vol. 68, no. 11, pp. 1376–1382, 2014. 2

[9] J. Silva-Velazco, D. W. Dietz, L. Stocchi, M. Costedio, E. Gorgun, M. F. Kalady, H. Kessler, I. C. Lavery, and F. H. Remzi, “Considering value in rectal cancer surgery: An analysis of costs and outcomes based on the open, laparoscopic, and robotic approach for proctectomy.” *Annals of surgery*, 2016. 3

[10] C. Bergeles, P. Pratt, R. Merrifield, A. Darzi, and G.-Z. Yang, “Multi-view stereo and advanced navigation for transanal endoscopic microsurgery,” *Medical Image Computing and Computer-Assisted Intervention MICCAI*, vol. 8674, pp. 332–339, 2014. 6, 7, 9

[11] V. Vitiello, S.-L. Lee, T. P. Cundy, and G.-Z. Yang, “Emerging robotic platforms for minimally invasive surgery.” *IEEE reviews in biomedical engineering*, vol. 6, pp. 111–26, Jan. 2013. 6, 7, 17

[12] C. A. Seneci, J. Shang, K. Leibrandt, V. Vitiello, N. Patel, A. Darzi, J. Teare, and G. Z. Yang, “Design and evaluation of a novel flexible robot for transluminal and endoluminal surgery,” in *Intelligent Robots and Systems (IROS 2014), 2014 IEEE/RSJ International Conference on*, Sept 2014, pp. 1314–1321. 7, 23

[13] A. De Donno, F. Nageotte, P. Zanne, L. Zorn, and M. de Mathelin, “Master/slave control of flexible instruments for minimally invasive surgery,” in *Intelligent Robots and Systems (IROS), 2013 IEEE/RSJ International Conference on*. IEEE, 2013, pp. 483–489. 7

[14] K. Taniguchi, A. Nishikawa, F. Miyazaki, K. Kazuhara, M. Mori, M. Sekimoto, N. Kurashita, S. Takiguchi, T. Ichihara, T. Kobayashi *et al.*, *Classification, design and evaluation of endoscope robots*. INTECH Open Access Publisher, 2010. 7

[15] R. E. Goldman, A. Bajo, L. S. MacLachlan, R. Pickens, S. D. Herrell, and N. Simaan, “Design and performance evaluation of a minimally invasive telerobotic platform for transurethral surveillance and intervention,” *Biomedical Engineering, IEEE Transactions on*, vol. 60, no. 4, pp. 918–925, 2013. 7

[16] V. Trévillot, R. Garrel, E. Dombre, P. Poignet, R. Sobral, and L. Crampette, “Robotic endoscopic sinus and skull base surgery: Review of the literature and future prospects,” *European annals of otorhinolaryngology, head and neck diseases*, vol. 130, no. 4, pp. 201–207, 2013. 7

[17] N. Simaan, K. Xu, W. Wei, A. Kapoor, P. Kazanzides, R. Taylor, and P. Flint, “Design and integration of a telerobotic system for minimally invasive surgery of the throat,” *The International journal of robotics research*, vol. 28, no. 9, pp. 1134–1153, 2009. 7, 16, 17

[18] T. Ota, A. Degani, D. Schwartzman, B. Zubiate, J. McGarvey, H. Choset, and M. A. Zenati, “A highly articulated robotic surgical system for minimally invasive surgery,” *The Annals of thoracic surgery*, vol. 87, no. 4, pp. 1253–1256, 2009. 7

[19] P. J. Swaney, J. Burgner, H. B. Gilbert, and R. J. Webster, “A flexure-based steerable needle: high curvature with reduced tissue damage,” *Biomedical Engineering, IEEE Transactions on*, vol. 60, no. 4, pp. 906–909, 2013. 7

[20] J. M. Romano, R. J. Webster III, and A. M. Okamura, “Teleoperation of steerable needles,” in *Robotics and Automation, 2007 IEEE International Conference on*. IEEE, 2007, pp. 934–939. 7

[21] D. C. Rucker, J. Das, H. B. Gilbert, P. J. Swaney, M. I. Miga, N. Sarkar, and R. J. Webster, “Sliding Mode Control of Steerable Needles,” *IEEE Transactions on Robotics*, vol. 29, no. 5, pp. 1289–1299, Oct. 2013. 7

[22] S. Atallah, B. Martin-Perez, D. Keller, J. Burke, and L. Hunter, “Natural-orifice transluminal endoscopic surgery,” *British Journal of Surgery*, vol. 102, no. 2, pp. e73–e92, 2015. 8

[23] N. Patel, C. Seneci, G.-Z. Yang, A. Darzi, and J. Teare, “Flexible platforms for natural orifice transluminal and endoluminal surgery,” *Endoscopy International Open*, vol. 2, no. 2, p. E117, 2014. 8

[24] E. D. Auyang, B. F. Santos, D. H. Enter, E. S. Hungness, and N. J. Soper, “Natural orifice translumenal endoscopic surgery (notes): a technical review,” *Surgical Endoscopy*, vol. 25, no. 10, pp. 3135–3148, 2011. 8

[25] A. C. Society, “Colorectal cancer facts & figures 2011-2013,” American Cancer Society, Report, 2011 2011. 9

[26] M. Braga, A. Vignali, L. Gianotti, W. Zuliani, G. Radaelli, P. Gruarin, P. Dellabona, and V. Di Carlo, “Laparoscopic versus open colorectal surgery: a randomized trial on short-term outcome,” *Annals of surgery*, vol. 236, no. 6, p. 759, 2002. 9

[27] P. F. Middleton, L. M. Sutherland, and G. J. Maddern, “Transanal endoscopic microsurgery: a systematic review,” *Diseases of the colon & rectum*, vol. 48, no. 2, pp. 270–284, 2005. 9

[28] M. Morino and M. E. Allaix, “Transanal endoscopic microsurgery: what indications in 2013?” *Gastroenterology report*, vol. 1, no. 2, pp. 75–84, 2013. 9

[29] G. Seva-Pereira, L. G. C. Romagnolo, J. J. d. Oliveira Filho, R. Bolzam-Nascimento, S. P. d. Moraes, and G. D. A. Ribeiro, “Transanal minimally invasive surgery (tamis) for local excision of selected rectal neoplasms: efficacy and outcomes in the first 11 patients,” *Journal of Coloproctology (Rio de Janeiro)*, vol. 34, no. 3, pp. 148–153, 2014. 9

[30] N. C. Buchs, F. Pugin, F. Volonte, M. E. Hagen, P. Morel, and F. Ris, "Robotic transanal endoscopic microsurgery: technical details for the lateral approach," *Diseases of the Colon & Rectum*, vol. 56, no. 10, pp. 1194–1198, 2013. 9

[31] S. Kiriyama, Y. Saito, S. Yamamoto, R. Soetikno, T. Matsuda, T. Nakajima, and H. Kuwano, "Comparison of endoscopic submucosal dissection with laparoscopic-assisted colorectal surgery for early-stage colorectal cancer: a retrospective analysis," *Endoscopy*, vol. 44, no. 11, p. 1024?1030, November 2012. [Online]. Available: http://dx.doi.org/10.1055/s-0032-1310259 10

[32] M. Kranzfelder, A. Schneider, A. Fiolka, S. Koller, D. Wilhelm, S. Reiser, A. Meining, and H. Feussner, "What do we really need? visions of an ideal human-machine interface for notes mechatronic support systems from the view of surgeons, gastroenterologists, and medical engineers," *Surgical Innovation*, p. 1553350614550720, 2014. 10

[33] N. Yoshida, N. Yagi, Y. Naito, and T. Yoshikawa, "Safe procedure in endoscopic submucosal dissection for colorectal tumors focused on preventing complications," *World Journal of Gastroenterology : WJG*, vol. 16, no. 14, pp. 1688–1695, 2010, 20379999[pmid] World J Gastroenterol. [Online]. Available: http://www.ncbi.nlm.nih.gov/pmc/articles/PMC2852815/ 11, 107

[34] V. I. Egorov, I. V. Schastlivtsev, E. V. Prut, A. O. Baranov, and R. A. Turusov, "Mechanical properties of the human gastrointestinal tract," *Journal of Biomechanics*, vol. 35, no. 10, pp. 1417 – 1425, 2002. [Online]. Available: http://www.sciencedirect.com/science/article/pii/S0021929002000842 11

[35] E.-J. Lee, J. Lee, Y. Choi, S. Lee, D. Lee, D. Kim, and E. Youk, "Clinical risk factors for perforation during endoscopic submucosal dissection (esd) for large-sized, nonpedunculated colorectal tumors," *Surgical Endoscopy*, vol. 26, no. 6, pp. 1587–1594, 2012. [Online]. Available: http://dx.doi.org/10.1007/s00464-011-2075-5 11, 12

[36] T. Sakamoto, Y. Saito, S. Fukunaga, T. Nakajima, and T. Matsuda, “Learning curve associated with colorectal endoscopic submucosal dissection for endoscopists experienced in gastric endoscopic submucosal dissection,” *Diseases of the Colon & Rectum*, vol. 54, no. 10, pp. 1307–1312, 2011. [Online]. Available: http://journals.lww.com/dcrjournal/Fulltext/2011/10000/Learning_Curve_Associated_With_Colorectal.16.aspx 11

[37] F. Iacopini, A. Bella, G. Costamagna, T. Gotoda, Y. Saito, W. Elisei, C. Grossi, P. Rigato, and A. Scozzarro, “Stepwise training in rectal and colonic endoscopic submucosal dissection with differentiated learning curves,” *Gastrointestinal Endoscopy*, vol. 76, no. 6, pp. 1188 – 1196, 2012. [Online]. Available: http://www.sciencedirect.com/science/article/pii/S0016510712026454 11

[38] T. Kato, I. Okumura, S.-e. Song, and N. Hata, “Multi-section Continuum Robot for Endoscopic Surgical Clipping of Intracranial Aneurysms,” *Med Image Comput Comput Assist Interv*, pp. 364–371, 2013. 11

[39] A. Y. B. Teoh, P. W. Y. Chiu, S. K. H. Wong, J. J. Y. Sung, J. Y. W. Lau, and E. K. W. Ng, “Difficulties and outcomes in starting endoscopic submucosal dissection,” *Surgical endoscopy*, vol. 24, no. 5, pp. 1049–1054, 2010. 12

[40] E. Manilich, J. Vogel, R. Kiran, J. Church, D. Seyidova-Khoshknabi, and F. Remzi, “Key factors associated with postoperative complications in patients undergoing colorectal surgery,” *Diseases of the Colon & Rectum*, vol. 56, no. 1, pp. 64–71, 2013. 12

[41] H. Feussner, V. Becker, M. Bauer, M. Kranzfelder, R. Schirren, T. Luth, A. Meining, and D. Wilhelm, “Developments in flexible endoscopic surgery: a review,” *Clinical and experimental gastroenterology*, vol. 8, p. 31, 2015. 12

[42] E. Butler, R. Hammond-Oakley, S. Chawarski, A. Gosline, P. Codd, T. Anor, J. Madsen, P. Dupont, and J. Lock, “Robotic neuro-emdoscope with

concentric tube augmentation," in *Intelligent Robots and Systems (IROS), 2012 IEEE/RSJ International Conference on*, Oct 2012, pp. 2941–2946. 12

[43] J. Zhao, X. Zheng, M. Zheng, A. Shih, and K. Xu, "An endoscopic continuum testbed for finalizing system characteristics of a surgical robot for notes procedures," in *Advanced Intelligent Mechatronics (AIM), 2013 IEEE/ASME International Conference on*, July 2013, pp. 63–70. 12

[44] G. Chen, M. T. Pham, and T. Redarce, "Sensor-based guidance control of a continuum robot for a semi-autonomous colonoscopy," *Robotics and autonomous systems*, vol. 57, no. 6, pp. 712–722, 2009. 12, 17

[45] J. Burgner, D. C. Rucker, H. B. Gilbert, P. J. Swaney, P. T. Russell, K. D. Weaver, and R. J. Webster, "A telerobotic system for transnasal surgery," *IEEE/ASME Transactions on Mechatronics*, vol. 19, no. 3, pp. 996–1006, 2014. 12, 17, 18, 23

[46] P. E. Dupont, J. Lock, B. Itkowitz, and E. Butler, "Design and control of concentric-tube robots," *Robotics, IEEE Transactions on*, vol. 26, no. 2, pp. 209–225, 2010. 13, 16, 22, 29, 43

[47] E. C. Burdette, D. C. Rucker, P. Prakash, C. J. Diederich, J. M. Croom, C. Clarke, P. J. Stolka, T. Juang, E. M. Boctor, and R. J. Webster III, "The ACUSITT Ultrasonic Ablator: The First Steerable Needle with an Integrated Interventional Tool," *Proceedings of SPIE Medical Imaging*, 2010. 13, 18

[48] R. J. Hendrick, S. D. Herrell, and R. J. Webster, "A multi-arm hand-held robotic system for transurethral laser prostate surgery," in *2014 IEEE International Conference on Robotics and Automation (ICRA)*, May 2014, pp. 2850–2855. 13, 18

[49] P. J. Swaney, A. W. Mahoney, A. A. Remirez, E. Lamers, B. I. Hartley, R. H. Feins, R. Alterovitz, and R. J. Webster, "Tendons, concentric tubes, and a bevel

tip: Three steerable robots in one transoral lung access system," in *2015 IEEE International Conference on Robotics and Automation (ICRA)*, May 2015, pp. 5378–5383. 13, 18

[50] S. J. Bardaro and L. Swanström, "Development of advanced endoscopes for Natural Orifice Transluminal Endoscopic Surgery (NOTES)." *Minimally invasive therapy & allied technologies : MITAT : official journal of the Society for Minimally Invasive Therapy*, vol. 15, no. 6, pp. 378–83, Jan. 2006. 13

[51] L. Swanström, P. Swain, and P. Denk, "Development and validation of a new generation of flexible endoscope for NOTES." *Surgical innovation*, vol. 16, no. 2, pp. 104–10, Jun. 2009. 13

[52] J. A. Astudillo, E. Sporn, S. Bachman, and B. Miedema, "Transgastric cholecystectomy using a prototype endoscope with 2 deflecting working channels (with video)," *Gastrointestinal Endoscopy*, vol. 69, no. 2, pp. 297–302, 2009. 13

[53] C. C. Thompson, M. Ryou, and N. J. Soper, "Evaluation of a manually driven , multitasking platform for complex endoluminal and natural orifice transluminal endoscopic surgery applications (with video)," *Gastrointestinal Endoscopy*, vol. 70, no. 1, pp. 121–125, 2009. 13

[54] B. Dallemagne and J. Marescaux, "The ANUBIS project." *Minimally invasive therapy & allied technologies : MITAT : official journal of the Society for Minimally Invasive Therapy*, vol. 19, no. 5, pp. 257–61, Oct. 2010. 13

[55] A. D. Donno, L. Zorn, P. Zanne, F. Nageotte, and M. D. Mathelin, "Introducing STRAS : a New Flexible Robotic System for Minimally Invasive Surgery," *IEEE International Conference on Intelligent Robots and Systems*, pp. 1213–1220, 2013. 13

[56] A. De Donno, F. Nageotte, P. Zanne, L. Zorn, and M. De Mathelin, "Master/slave control of flexible instruments for minimally invasive surgery," *IEEE International Conference on Intelligent Robots and Systems*, pp. 483–489, 2013. 13

[57] S. J. Phee, S. C. Low, V. A. Huynh, A. P. Kencana, Z. L. Sun, and K. Yang, "Master and slave transluminal endoscopic robot (MASTER) for natural orifice transluminal endoscopic surgery (NOTES)." *Conference proceedings : ... Annual International Conference of the IEEE Engineering in Medicine and Biology Society. IEEE Engineering in Medicine and Biology Society. Annual Conference*, vol. 2009, pp. 1192–5, Jan. 2009. 13

[58] K.-Y. Ho, S. J. Phee, A. Shabbir, S. C. Low, V. A. Huynh, A. P. Kencana, K. Yang, D. Lomanto, B. Y. J. So, Y. Y. J. Wong, and S. C. S. Chung, "Endoscopic submucosal dissection of gastric lesions by using a Master and Slave Transluminal Endoscopic Robot (MASTER)." *Gastrointestinal endoscopy*, vol. 72, no. 3, pp. 593–9, Sep. 2010. 13

[59] B. Siciliano and O. Khatib, *Springer handbook of robotics.* Springer, 2008. 15

[60] R. J. Webster and B. A. Jones, "Design and kinematic modeling of constant curvature continuum robots: A review," *The International Journal of Robotics Research*, 2010. 15, 17, 21, 28, 43

[61] W. McMahan, V. Chitrakaran, M. M. Csencsits, D. Dawson, I. D. Walker, B. A. Jones, M. Pritts, D. Dienno, M. Grissom, and C. D. Rahn, "Field trials and testing of the OctArm continuum manipulator," *IEEE International Conference on Robotics and Automation*, pp. 2336–2341, 2006. 16, 22

[62] J. Ding, R. E. Goldman, K. Xu, P. K. Allen, D. L. Fowler, and N. Simaan, "Design and coordination kinematics of an insertable robotic effectors platform

for single-port access surgery," *Mechatronics, IEEE/ASME Transactions on*, vol. 18, no. 5, pp. 1612–1624, 2013. 16, 21, 22

[63] D. C. Rucker and R. J. Webster III, "Deflection-Based Force Sensing for Continuum Robots: A Probabilistic Approach," *IEEE/RSJ International Conference on Intellegent Robots and Systems*, pp. 3764–3769, 2011. 16, 26, 30, 42

[64] D. B. Camarillo, C. F. Milne, C. R. Carlson, M. R. Zinn, and J. K. Salisbury, "Mechanics Modeling of Tendon-Driven Continuum Manipulators," *IEEE Transactions on Robotics*, vol. 24, no. 6, pp. 1262–1273, 2008. 16

[65] I. A. Gravagne, C. D. Rahn, and I. D. Walker, "Large-Deflection Dynamics and Control for Planar Continuum Robots," *IEEE/ASME Transactions on Mechatronics*, vol. 8, no. 2, pp. 299–307, Jun. 2003. 16

[66] P. E. Dupont, J. Lock, B. Itkowitz, and E. Butler., "Design and Control of Concentric-Tube Robots," *IEEE Transactions on Robotics*, vol. 26, pp. 209–225, 2010. 16, 18

[67] D. C. Rucker, B. A. Jones, and R. J. Webster, "A geometrically exact model for externally loaded concentric-tube continuum robots," *Robotics, IEEE Transactions on*, vol. 26, no. 5, pp. 769–780, 2010. 16, 22, 28, 30, 68

[68] R. J. Webster III, J. M. Romano, and N. J. Cowan, "Mechanics of Precurved-Tube Continuum Robots," *IEEE Transactions on Robotics*, vol. 25, no. 1, pp. 67–78, 2009. 16

[69] W. McMahan, V. Chitrakaran, M. Csencsits, D. Dawson, I. D. Walker, B. A. Jones, M. Pritts, D. Dienno, M. Grissom, and C. D. Rahn, "Field trials and testing of the octarm continuum manipulator," in *Robotics and Automation, 2006. ICRA 2006. Proceedings 2006 IEEE International Conference on*. IEEE, 2006, pp. 2336–2341. 16

[70] D. C. Rucker and R. J. Webster, “Statics and dynamics of continuum robots with general tendon routing and external loading,” *Robotics, IEEE Transactions on*, vol. 27, no. 6, pp. 1033–1044, 2011. 16, 28

[71] D. B. Camarillo, C. F. Milne, C. R. Carlson, M. R. Zinn, and J. K. Salisbury, “Mechanics modeling of tendon-driven continuum manipulators,” *Robotics, IEEE Transactions on*, vol. 24, no. 6, pp. 1262–1273, 2008. 16, 17, 22

[72] I. A. Gravagne, C. D. Rahn, and I. D. Walker, “Large deflection dynamics and control for planar continuum robots,” *Mechatronics, IEEE/ASME Transactions on*, vol. 8, no. 2, pp. 299–307, 2003. 16, 28

[73] D. C. Rucker, B. A. Jones, and R. J. Webster III, “A Model for Concentric Tube Continuum Robots Under Applied Wrenches,” *IEEE International Conference on Robtics and Automation*, pp. 1047–1052, 2010. 16

[74] D. C. Rucker, R. J. Webster, G. S. Chirikjian, and N. J. Cowan, “Equilibrium Conformations of Concentric-tube Continuum Robots,” *The International Journal of Robotics Research*, vol. 29, no. 10, pp. 1263–1280, Apr. 2010. 16, 69

[75] C. E. Bryson and D. C. Rucker, “Toward parallel continuum manipulators,” in *Robotics and Automation (ICRA), 2014 IEEE International Conference on*. IEEE, 2014, pp. 778–785. 16, 29, 40, 44, 46, 59, 63, 79, 87, 95

[76] H.-S. Yoon and B.-J. Yi, “A 4-dof flexible continuum robot using a spring backbone,” in *Mechatronics and Automation, 2009. ICMA 2009. International Conference on*. IEEE, 2009, pp. 1249–1254. 17

[77] M. D. M. Kutzer, S. M. Segreti, C. Y. Brown, M. Armand, R. H. Taylor, and S. C. Mears, “Design of a new cable-driven manipulator with a large open lumen: Preliminary applications in the minimally-invasive removal of osteolysis,” in *Robotics and Automation (ICRA), 2011 IEEE International Conference on*. IEEE, 2011, pp. 2913–2920. 17

[78] K. Xu and N. Simaan, "Intrinsic wrench estimation and its performance index for multisegment continuum robots," *Robotics, IEEE Transactions on*, vol. 26, no. 3, pp. 555–561, 2010. 17, 26

[79] N. Simaan, "Snake-like units using flexible backbones and actuation redundancy for enhanced miniaturization," in *Robotics and Automation, 2005. ICRA 2005. Proceedings of the 2005 IEEE International Conference on.* IEEE, 2005, pp. 3012–3017. 17, 21

[80] A. H. Gosline, N. V. Vasilyev, E. J. Butler, C. Folk, A. Cohen, R. Chen, N. Lang, P. J. Del Nido, and P. E. Dupont, "Percutaneous intracardiac beating-heart surgery using metal mems tissue approximation tools," *The International journal of robotics research*, p. 0278364912443718, 2012. 17

[81] M. Mahvash and P. E. Dupont, "Stiffness control of surgical continuum manipulators," *Robotics, IEEE Transactions on*, vol. 27, no. 2, pp. 334–345, 2011. 17, 26

[82] R. J. Webster, J. M. Romano, and N. J. Cowan, "Mechanics of precurved-tube continuum robots," *Robotics, IEEE Transactions on*, vol. 25, no. 1, pp. 67–78, 2009. 17

[83] J. Burgner, P. J. Swaney, R. A. Lathrop, K. D. Weaver, and R. J. Webster, "Debulking from within: a robotic steerable cannula for intracerebral hemorrhage evacuation," *Biomedical Engineering, IEEE Transactions on*, vol. 60, no. 9, pp. 2567–2575, 2013. 17

[84] M. Xu, X.-Y. Wang, P.-H. Zhou, Q.-L. Li, Y. Zhang, Y. Zhong, W. Chen, L. Ma, S. Ishaq, W. Qin *et al.*, "Endoscopic full-thickness resection of colonic submucosal tumors originating from the muscularis propria: an evolving therapeutic strategy," *Endoscopy*, vol. 45, no. 09, pp. 770–773, 2013. 17

[85] Y. Bailly, Y. Amirat, and G. Fried, "Modeling and control of a continuum style microrobot for endovascular surgery," *Robotics, IEEE Transactions on*, vol. 27, no. 5, pp. 1024–1030, 2011. 17

[86] K. Ikuta, H. Ichikawa, K. Suzuki, and D. Yajima, "Multi-degree of freedom hydraulic pressure driven safety active catheter," in *Robotics and Automation, 2006. ICRA 2006. Proceedings 2006 IEEE International Conference on*. IEEE, 2006, pp. 4161–4166. 17

[87] K. Ikuta, M. Matsuda, D. Yajima, and Y. Ota, "Pressure pulse drive: A control method for the precise bending of hydraulic active catheters," *Mechatronics, IEEE/ASME Transactions on*, vol. 17, no. 5, pp. 876–883, 2012. 17

[88] B. A. Jones and I. D. Walker, "Kinematics for multisection continuum robots," *Robotics, IEEE Transactions on*, vol. 22, no. 1, pp. 43–55, 2006. 17, 29

[89] W. McMahan, B. A. Jones, and I. D. Walker, "Design and implementation of a multi-section continuum robot: Air-octor," in *Intelligent Robots and Systems, 2005.(IROS 2005). 2005 IEEE/RSJ International Conference on*. IEEE, 2005, pp. 2578–2585. 17

[90] J. Jayender, M. Azizian, and R. V. Patel, "Autonomous image-guided robot-assisted active catheter insertion," *Robotics, IEEE Transactions on*, vol. 24, no. 4, pp. 858–871, 2008. 17

[91] J. Jayender, R. V. Patel, and S. Nikumb, "Robot-assisted active catheter insertion: algorithms and experiments," *The International Journal of Robotics Research*, vol. 28, no. 9, pp. 1101–1117, 2009. 17

[92] E. Ayvali, C.-P. Liang, M. Ho, Y. Chen, and J. P. Desai, "Towards a discretely actuated steerable cannula for diagnostic and therapeutic procedures," *The International journal of robotics research*, vol. 31, no. 5, pp. 588–603, 2012. 17

[93] J. H. Crews and G. D. Buckner, “Design optimization of a shape memory alloy–actuated robotic catheter,” *Journal of Intelligent Material Systems and Structures*, p. 1045389X12436738, 2012. 17, 23

[94] S. Hirose, *Biologically Inspired Robots, Snake-Like Locomotors and Manipulators.* Oxford University Press, 1993. 17

[95] G. Robinson and J. B. C. Davies, “Continuum robots-a state of the art,” in *Robotics and Automation, 1999. Proceedings. 1999 IEEE International Conference on*, vol. 4. IEEE, 1999, pp. 2849–2854. 17

[96] C. Majidi, “Soft robotics: a perspectivecurrent trends and prospects for the future,” *Soft Robotics*, vol. 1, no. 1, pp. 5–11, 2014. 17

[97] D. Trivedi, A. Lotfi, and C. D. Rahn, “Geometrically exact models for soft robotic manipulators,” *Robotics, IEEE Transactions on*, vol. 24, no. 4, pp. 773–780, 2008. 17, 28

[98] S. Kim, C. Laschi, and B. Trimmer, “Soft robotics: a bioinspired evolution in robotics,” *Trends in biotechnology*, vol. 31, no. 5, pp. 287–294, 2013. 17

[99] J. K. Hopkins, B. W. Spranklin, and S. K. Gupta, “A survey of snake-inspired robot designs,” *Bioinspiration & Biomimetics*, vol. 4, no. 2, p. 021001, 2009. 17

[100] A. A. Transeth, K. Y. Pettersen, and P. Liljebäck, “A survey on snake robot modeling and locomotion,” *Robotica*, vol. 27, no. 07, pp. 999–1015, 2009. 17

[101] S. Hirose and H. Yamada, “Snake-like robots [tutorial],” *Robotics & Automation Magazine, IEEE*, vol. 16, no. 1, pp. 88–98, 2009. 17

[102] I. D. Walker, “Robot strings: long, thin continuum robots,” in *Aerospace Conference, 2013 IEEE.* IEEE, 2013, pp. 1–12. 17

[103] ——, “Continuous backbone continuum robot manipulators,” *ISRN Robotics*, vol. 2013, 2013. 17

[104] H. B. Gilbert, D. C. Rucker, and R. J. Webster III, “Concentric tube robots: The state of the art and future directions,” in *Robotics Research*. Springer, 2016, pp. 253–269. 18

[105] J.-P. Merlet, *Parallel robots*. Springer, 2001, vol. 74. 19, 20

[106] X. Zhang, J. K. Mills, and W. L. Cleghorn, “Dynamic modeling and experimental validation of a 3-prr parallel manipulator with flexible intermediate links,” *Journal of Intelligent and Robotic Systems*, vol. 50, no. 4, pp. 323–340, 2007. 19

[107] B. Kang and J. K. Mills, “Dynamic modeling of structurally-flexible planar parallel manipulator,” *Robotica*, vol. 20, no. 03, pp. 329–339, 2002. 19

[108] B. Kang, B. Yeung, and J. K. Mills, “Two-time scale controller design for a high speed planar parallel manipulator with structural flexibility,” *Robotica*, vol. 20, no. 05, pp. 519–528, 2002. 19

[109] G. Piras, W. Cleghorn, and J. Mills, “Dynamic finite-element analysis of a planar high-speed, high-precision parallel manipulator with flexible links,” *Mechanism and Machine Theory*, vol. 40, no. 7, pp. 849–862, 2005. 19

[110] S. Briot and V. Arakelian, “On the dynamic properties of rigid-link flexible-joint parallel manipulators in the presence of type 2 singularities,” *Journal of Mechanisms and Robotics*, vol. 2, no. 2, p. 021004, 2010. 19

[111] S. Briot and W. Khalil, “Recursive symbolic calculation of the dynamic model of flexible parallel robots,” in *Robotics and Automation (ICRA), 2013 IEEE International Conference on*. IEEE, 2013, pp. 5433–5438. 19

[112] S. Tzafestas, M. Kotsis, and T. Pimenides, “Observer-based optimal control of flexible stewart parallel robots,” *Journal of Intelligent and Robotic Systems*, vol. 34, no. 4, pp. 489–503, 2002. 19

[113] J. Lee and Z. Geng, "A dynamic model of a flexible stewart platform," *Computers & structures*, vol. 48, no. 3, pp. 367–374, 1993. 19

[114] Y. Qin, K. Zhang, J. Li, and J. S. Dai, "Modelling and analysis of a rigid-compliant parallel mechanism," *Robotics and Computer-Integrated Manufacturing*, vol. 29, no. 4, pp. 33–40, Aug. 2013. 19

[115] C. Amici, a. Borboni, R. Faglia, D. Fausti, and P. Magnani, "A parallel compliant meso-manipulator for finger rehabilitation treatments: Kinematic and dynamic analysis." *2008 IEEE/RSJ International Conference on Intelligent Robots and Systems*, pp. 735–740, Sep. 2008. 19

[116] G. Aridon, D. Remond, F. Morestin, L. Blanchard, and R. Dufour, "Self-Deployment of a Tape-Spring Hexapod: Experimental and Numerical Investigation," *Journal of Mechanical Design*, vol. 131, no. 2, p. 021003, 2009. [Online]. Available: http://mechanicaldesign.asmedigitalcollection.asme.org/article.aspx?articleid=1472493 19

[117] G. Hao and X. Kong, "Design and Modeling of a Large-Range Modular XYZ Compliant Parallel Manipulator Using Identical Spatial Modules," *Journal of Mechanisms and Robotics*, vol. 4, no. 2, p. 021009, 2012. [Online]. Available: http://mechanismsrobotics.asmedigitalcollection.asme.org/article.aspx?articleid=1484753 19

[118] C. Quennouelle and C. Gosselin, "A Quasi-Static Model for Planar Compliant Parallel Mechanisms," *Journal of Mechanisms and Robotics*, vol. 1, no. 2, p. 021012, 2009. [Online]. Available: http://mechanismsrobotics.asmedigitalcollection.asme.org/article.aspx?articleid=1484875 19

[119] ——, "Kinematostatic modeling of compliant parallel mechanisms," *Meccanica*, vol. 46, no. 1, pp. 155–169, Jan. 2011. [Online]. Available: http://link.springer.com/10.1007/s11012-010-9408-7 19

[120] J. McInroy and J. Hamann, “Design and control of flexure jointed hexapods,” *IEEE Transactions on Robotics and Automation*, vol. 16, no. 4, pp. 372–381, 2000. [Online]. Available: http://ieeexplore.ieee.org/lpdocs/epic03/wrapper.htm?arnumber=864229 19

[121] J. McInroy, “Modeling and design of flexure jointed Stewart platforms for control purposes,” *IEEE/ASME Transactions on Mechatronics*, vol. 7, no. 1, pp. 95–99, Mar. 2002. [Online]. Available: http://ieeexplore.ieee.org/lpdocs/epic03/wrapper.htm?arnumber=990892 19

[122] W. Dong, L. Sun, and Z. Du, “Design of a precision compliant parallel positioner driven by dual piezoelectric actuators,” *Sensors and Actuators A: Physical*, vol. 135, no. 1, pp. 250–256, Mar. 2007. 19

[123] J. Hesselbach and A. Raatz, “Compliant parallel robot with 6 DOF,” in *Intelligent Systems and Advanced Manufacturing*, B. J. Nelson and J.-M. Breguet, Eds. International Society for Optics and Photonics, Oct. 2001, pp. 143–150. [Online]. Available: http://proceedings.spiedigitallibrary.org/proceeding.aspx?articleid=900944 19

[124] Y. Yun and Y. Li, “Design and analysis of a novel 6-DOF redundant actuated parallel robot with compliant hinges for high precision positioning,” *Nonlinear Dynamics*, vol. 61, no. 4, pp. 829–845, Mar. 2010. [Online]. Available: http://link.springer.com/10.1007/s11071-010-9690-x 19

[125] F. Sergi, M. M. Lee, and M. K. OMalley, “Design of a series elastic actuator for a compliant parallel wrist rehabilitation robot,” *IEEE International Conference on Rehabilitation Robotics*, 2013. 19

[126] J. Peirs, D. Reynaerts, and H. Van Brussel, “Design of miniature parallel manipulators for integration in a self-propelling endoscope,” *Sensors and Actuators A: Physical*, vol. 85, no. 1, pp. 409–417, 2000. 19

[127] J.-P. Merlet, "Parallel manipulators: state of the art and perspectives," *Advanced Robotics*, vol. 8, no. 6, pp. 589–596, 1993. 20

[128] A. L. Orekhov, C. E. Bryson, J. Till, S. Chung, and D. C. Rucker, "A surgical parallel continuum manipulator with a cable-driven grasper," in *Engineering in Medicine and Biology Society (EMBC), 2015 37th Annual International Conference of the IEEE*. IEEE, 2015, pp. 5264–5267. 20, 21, 54

[129] J.-P. Merlet, *Parallel robots*. Springer Science & Business Media, 2012, vol. 74. 21

[130] N. Simaan, R. Taylor, and P. Flint, "A dexterous system for laryngeal surgery," in *Robotics and Automation, 2004. Proceedings. ICRA'04. 2004 IEEE International Conference on*, vol. 1. IEEE, 2004, pp. 351–357. 21, 22

[131] J. Burgner-Kahrs, D. C. Rucker, and H. Choset, "Continuum robots for medical applications: A survey," *Robotics, IEEE Transactions on*, vol. 31, no. 6, pp. 1261–1280, 2015. 21

[132] A. Orekhov, C. B. Black, J. Till, and D. C. Rucker, "Analysis and validation of a teleoperated surgical parallel continuum manipulator," in *The IEEE Robotics and Automation Letters*. IEEE, 2016, p. In Press. 21, 95

[133] M. Veloso, J. Biswas, B. Coltin, S. Rosenthal, T. Kollar, C. Mericli, M. Samadi, S. Brando, and R. Ventura, "Cobots: Collaborative robots servicing multi-floor buildings," in *2012 IEEE/RSJ International Conference on Intelligent Robots and Systems*, Oct 2012, pp. 5446–5447. 22

[134] R. E. Goldman, A. Bajo, and N. Simaan, "Compliant motion control for multisegment continuum robots with actuation force sensing," *Robotics, IEEE Transactions on*, vol. 30, no. 4, pp. 890–902, 2014. 22, 26

[135] [Online]. Available: http://www.festo.com/net/SupportPortal/Files/46268 22

[136] N. Simaan, R. Taylor, and P. Flint, “High dexterity snake-like robotic slaves for minimally invasive telesurgery of the upper airway,” in *Medical Image Computing and Computer-Assisted Intervention–MICCAI 2004*. Springer, 2004, pp. 17–24. 22

[137] N. Simaan, R. Taylor, A. Hillel, and P. Flint, “Minimally invasive surgery of the upper airways: Addressing the challenges of dexterity enhancement in confined spaces,” *Surgical Robotics-History, Present and Future Applications*, pp. 261–280, 2007. 22

[138] D. Trivedi, C. D. Rahn, W. M. Kier, and I. D. Walker, “Soft robotics: Biological inspiration, state of the art, and future research,” *Applied Bionics and Biomechanics*, vol. 5, no. 3, pp. 99–117, 2008. 22

[139] J. Burgner, H. B. Gilbert, and R. J. Webster, “On the computational design of concentric tube robots: Incorporating volume-based objectives,” in *Robotics and Automation (ICRA), 2013 IEEE International Conference on*. IEEE, 2013, pp. 1193–1198. 23

[140] C. Bedell, J. Lock, A. Gosline, and P. E. Dupont, “Design optimization of concentric tube robots based on task and anatomical constraints,” in *Robotics and Automation (ICRA), 2011 IEEE International Conference on*. IEEE, 2011, pp. 398–403. 23

[141] H. Hu, P. Wang, B. Zhao, M. Li, and L. Sun, “Design of a novel snake-like robotic colonoscope,” in *Robotics and Biomimetics (ROBIO), 2009 IEEE International Conference on*, Dec 2009, pp. 1957–1961. 23

[142] A. Bajo, R. E. Goldman, L. Wang, D. Fowler, and N. Simaan, “Integration and preliminary evaluation of an insertable robotic effectors platform for single port access surgery,” in *Robotics and Automation (ICRA), 2012 IEEE International Conference on*, May 2012, pp. 3381–3387. 23

[143] P. Qi, H. Liu, L. Seneviratne, and K. Althoefer, "Towards kinematic modeling of a multi-dof tendon driven robotic catheter," in *Engineering in Medicine and Biology Society (EMBC), 2014 36th Annual International Conference of the IEEE*, Aug 2014, pp. 3009–3012. 23

[144] J. Granna and J. Burgner, "Characterizing the workspace of concentric tube continuum robots," in *ISR/Robotik 2014; 41st International Symposium on Robotics; Proceedings of*, June 2014, pp. 1–7. 23

[145] K. Xu and X. Zheng, "Configuration comparison for surgical robotic systems using a single access port and continuum mechanisms," in *Robotics and Automation (ICRA), 2012 IEEE International Conference on*, May 2012, pp. 3367–3374. 23

[146] J.-P. Merlet, "Jacobian, manipulability, condition number, and accuracy of parallel robots," *Journal of Mechanical Design*, vol. 128, no. 1, pp. 199–206, 2006. 23, 80

[147] G. Gogu, *Structural synthesis of parallel robots.* Springer, 2008. 23

[148] X.-J. Liu, C. Wu, and J. Wang, "A new index for the performance evaluation of parallel manipulators: A study on planar parallel manipulators," in *Intelligent Control and Automation, 2008. WCICA 2008. 7th World Congress on*, June 2008, pp. 353–357. 23

[149] J. Shim, S. Song, D. Kwon, and H. Cho, "Kinematic feature analysis of a 6-degree-of-freedom in-parallel manipulator for micro-positioning surgical," in *Intelligent Robots and Systems, 1997. IROS '97., Proceedings of the 1997 IEEE/RSJ International Conference on*, vol. 3, Sep 1997, pp. 1617–1623 vol.3. 23

[150] S. Patel and T. Sobh, "Manipulator performance measures - a comprehensive literature survey," *Journal of Intelligent & Robotic Systems*, vol. 77, no. 3-4, pp. 547–570, 2015. 23, 80, 85, 86

[151] I. Gravagne, I. D. Walker *et al.*, "Manipulability, force, and compliance analysis for planar continuum manipulators," *Robotics and Automation, IEEE Transactions on*, vol. 18, no. 3, pp. 263–273, 2002. 23, 25, 74

[152] K. Xu, M. Fu, and J. Zhao, "An experimental kinestatic comparison between continuum manipulators with structural variations," in *Robotics and Automation (ICRA), 2014 IEEE International Conference on*. IEEE, 2014, pp. 3258–3264. 23

[153] M. Mahvash, J. Gwilliam, R. Agarwal, B. Vagvolgyi, L.-M. Su, D. D. Yuh, and A. M. Okamur, "Force-feedback surgical teleoperator: Controller design and palpation experiments," in *Haptic interfaces for virtual environment and teleoperator systems, 2008. haptics 2008. symposium on*. IEEE, 2008, pp. 465–471. 24

[154] J. C. Gwilliam, M. Mahvash, B. Vagvolgyi, A. Vacharat, D. D. Yuh, and A. M. Okamura, "Effects of haptic and graphical force feedback on teleoperated palpation," in *Robotics and Automation, 2009. ICRA'09. IEEE International Conference on*. IEEE, 2009, pp. 677–682. 24

[155] C. Basdogan, S. De, J. Kim, M. Muniyandi, H. Kim, and M. A. Srinivasan, "Haptics in minimally invasive surgical simulation and training," *Computer Graphics and Applications, IEEE*, vol. 24, no. 2, pp. 56–64, 2004. 24

[156] M. A. Srinivasan and C. Basdogan, "Haptics in virtual environments: Taxonomy, research status, and challenges," *Computers & Graphics*, vol. 21, no. 4, pp. 393–404, 1997. 24

[157] D. A. Lawrence, “Stability and transparency in bilateral teleoperation,” *Robotics and Automation, IEEE Transactions on*, vol. 9, no. 5, pp. 624–637, 1993. 25

[158] M. J. Lum, D. C. Friedman, H. H. King, R. Donlin, G. Sankaranarayanan, T. J. Broderick, M. N. Sinanan, J. Rosen, and B. Hannaford, “Teleoperation of a surgical robot via airborne wireless radio and transatlantic internet links,” in *Field and service robotics.* Springer, 2008, pp. 305–314. 25

[159] O. Mohareri, C. Schneider, and S. Salcudean, “Bimanual telerobotic surgery with asymmetric force feedback: A davinci; surgical system implementation,” in *2014 IEEE/RSJ International Conference on Intelligent Robots and Systems*, Sept 2014, pp. 4272–4277. 25

[160] M. Moradi Dalvand, B. Shirinzadeh, A. H. Shamdani, J. Smith, and Y. Zhong, “An actuated force feedback-enabled laparoscopic instrument for robotic-assisted surgery,” *The International Journal of Medical Robotics and Computer Assisted Surgery*, vol. 10, no. 1, pp. 11–21, 2014. 25

[161] P. B. McBeth, D. F. Louw, P. R. Rizun, and G. R. Sutherland, “Robotics in neurosurgery,” *The American Journal of Surgery*, vol. 188, no. 4, pp. 68–75, 2004. 25

[162] T. Yoshikawa, *Foundations of robotics: analysis and control.* Mit Press, 1990. 25, 74, 80, 85, 86

[163] K. Xu and N. Simaan, “An investigation of the intrinsic force sensing capabilities of continuum robots,” *Robotics, IEEE Transactions on*, vol. 24, no. 3, pp. 576–587, 2008. 26, 43

[164] A. Bajo and N. Simaan, “Finding lost wrenches: Using continuum robots for contact detection and estimation of contact location,” in *Robotics and*

Automation (ICRA), 2010 IEEE International Conference on. IEEE, 2010, pp. 3666–3673. 26

[165] J. Back, T. Manwell, R. Karim, K. Rhode, K. Althoefer, and H. Liu, "Catheter contact force estimation from shape detection using a real-time cosserat rod model," in *Intelligent Robots and Systems (IROS), 2015 IEEE/RSJ International Conference on.* IEEE, 2015, pp. 2037–2042. 26

[166] M. Khoshnam, A. Skanes, and R. V. Patel, "Modeling and estimation of tip contact force for steerable ablation catheters," *IEEE Transactions on Biomedical Engineering*, pp. 1404–1415, 2015. 26

[167] R. E. Goldman, A. Bajo, and N. Simaan, "Compliant motion control for continuum robots with intrinsic actuation sensing," in *Robotics and Automation (ICRA), 2011 IEEE International Conference on.* IEEE, 2011, pp. 1126–1132. 26

[168] A. Shiva, A. Stilli, Y. Noh, A. Faragasso, I. D. Falco, G. Gerboni, M. Cianchetti, A. Menciassi, K. Althoefer, and H. A. Wurdemann, "Tendon-based stiffening for a pneumatically actuated soft manipulator," *IEEE Robotics and Automation Letters*, vol. 1, no. 2, pp. 632–637, July 2016. 27

[169] I. Tunay, "Spatial continuum models of rods undergoing large deformation and inflation," *Robotics, IEEE Transactions on*, vol. 29, no. 2, pp. 297–307, 2013. 28

[170] J. Till, C. E. Bryson, S. Chung, A. Orekhov, and D. C. Rucker, "Efficient computation of multiple coupled cosserat rod models for real-time simulation and control of parallel continuum manipulators," in *Robotics and Automation (ICRA), 2015 IEEE International Conference on*, May 2015, pp. 5067–5074. 29, 41, 58, 59, 63, 67, 95

[171] S. S. Antman and S. Antman, *Nonlinear problems of elasticity*. Springer, 2005, vol. 107. 29, 30

[172] R. M. Murray, Z. Li, and S. S. Sastry, *A mathematical introduction to robotic manipulation*. CRC press, 1994. 30, 48, 69

[173] C. B. S. a. R. Wall-Epstein, S. P. S. a. R. Kordell, S. M. S. a. R. Chamberlain, and K. A. F. a. M. Stafford, *Multi-Segment Parallel Continuum Manipulator*. Worcester, MA: Worcester Polytechnic Institute, 2015. 44

[174] J. Till and D. C. Rucker, "Elastic stability of cosserat rods and parallel continuum robots," *IEEE Transactions on Robotics*, vol. PP, no. 99, pp. 1–16, 2017. 54

[175] A. M. Okamura, "Haptic feedback in robot-assisted minimally invasive surgery," *Current Opinion in Urology*, vol. 19, no. 1, pp. 102–107, 2009. 59

[176] O. A. J. van der Meijden and M. P. Schijven, "The value of haptic feedback in conventional and robot-assisted minimal invasive surgery and virtual reality training: a current review," *Surgical Endoscopy*, vol. 23, no. 6, pp. 1180–1190, 2009. 59

[177] H. Visser, E. Heijnsdijk, J. Herder, and P. Pistecky, "Forces and displacements in colon surgery," *Surgical Endoscopy And Other Interventional Techniques*, vol. 16, no. 10, pp. 14 263–1430, 2002. [Online]. Available: http://dx.doi.org/10.1007/s00464-002-9003-7 62, 106

[178] J. Manton, "A globally convergent numerical algorithm for computing the centre of mass on compact lie groups," *Control, Automation, Robotics and Vision Conference*, vol. 3, pp. 2211–2216, Dec 2004. 62

[179] P. E. Dupont, J. Lock, B. Itkowitz, and E. Butler, "Design and control of concentric-tube robots," *IEEE Transactions on Robotics*, vol. 26, no. 2, pp. 209–225, 2010. 69

[180] A. Sánchez, P. Poignet, E. Dombre, A. Menciassi, and P. Dario, "A design framework for surgical robots: Example of the araknes robot controller," *Robotics and Autonomous Systems*, vol. 62, no. 9, pp. 1342–1352, 2014. 72

[181] D. C. Rucker and R. Webster, "Computing jacobians and compliance matrices for externally loaded continuum robots," *Robotics and Automation (ICRA), 2011 IEEE International Conference on*, pp. 945–950, 2011. 74

[182] Y. Zhu, J. Yang, H. Jin, X. Zang, and J. Zhao, "Design and evaluation of a parallel-series elastic actuator for lower limb exoskeletons." IEEE, 2014, pp. 1335–1340. 74

[183] M. Grimmer, M. Eslamy, S. Gliech, and A. Seyfarth, "A comparison of parallel- and series elastic elements in an actuator for mimicking human ankle joint in walking and running," in *Robotics and Automation (ICRA), 2012 IEEE International Conference on*, May 2012, pp. 2463–2470. 74

[184] S. Chung, C. Bryson, J. Till, J. Carlton, and C. Rucker, "Teleoperation of parallel continuum manipulators using approximate kinematic models," in *Intelligent Robots and Systems (IROS), 2014 IEEE International Conference on*. IEEE, 2014. 77

[185] M. W. Spong, S. Hutchinson, and M. Vidyasagar, *Robot modeling and control*. Wiley New York, 2006, vol. 3. 80

[186] W. Curtis, J. D. Logan, and W. Parker, "Dimensional analysis and the pi theorem," *Linear Algebra and its Applications*, vol. 47, pp. 117–126, 1982. 88

[187] S. Thrun, W. Burgard, and D. Fox, *Probabilistic robotics*. MIT press, 2005. 93

[188] T. T. Kararli, "Comparison of the gastrointestinal anatomy, physiology, and biochemistry of humans and commonly used laboratory animals," *Biopharmaceutics & drug disposition*, vol. 16, no. 5, pp. 351–380, 1995. 105

[189] S. Sadahiro, T. Ohmura, Y. Yamada, T. Saito, and Y. Taki, "Analysis of length and surface area of each segment of the large intestine according to age, sex and physique," *Surgical and Radiologic Anatomy*, vol. 14, no. 3, pp. 251–257, 1992. 105

[190] E. A. M. Heijnsdijk, M. van der Voort, H. de Visser, J. Dankelman, and D. J. Gouma, "Inter- and intraindividual variabilities of perforation forces of human and pig bowel tissue," *Surgical Endoscopy And Other Interventional Techniques*, vol. 17, no. 12, pp. 1923–1926, 2003. [Online]. Available: http://dx.doi.org/10.1007/s00464-003-9002-3 106

[191] S. Varadarajulu, S. Banerjee, B. A. Barth, D. J. Desilets, V. Kaul, S. R. Kethu, M. C. Pedrosa, P. R. Pfau, J. L. Tokar, A. Wang, L.-M. W. K. Song, and S. A. Rodriguez, "{GI} endoscopes," *Gastrointestinal Endoscopy*, vol. 74, no. 1, pp. 1 – 6.e6, 2011. [Online]. Available: http://www.sciencedirect.com/science/article/pii/S0016510711001301 106

[192] J. G. Guillem, P. B. Paty, and A. M. Cohen, "Surgical treatment of colorectal cancer," *CA: A Cancer Journal for Clinicians*, vol. 47, no. 2, pp. 113–128, 1997. [Online]. Available: http://dx.doi.org/10.3322/canjclin.47.2.113 106

[193] S. N. Shaikh and C. C. Thompson, "Natural orifice translumenal surgery: Flexible platform review." *World journal of gastrointestinal surgery*, vol. 2, no. 6, pp. 210–6, Jun. 2010. 107

[194] D. Y. Lee, J. Kim, J. S. Kim, C. Baek, G. Noh, D. N. Kim, K. Kim, S. Kang, and K. J. Cho, "Anisotropic patterning to reduce instability of concentric-tube robots," *IEEE Transactions on Robotics*, vol. 31, no. 6, pp. 1311–1323, Dec 2015. 112, 113

[195] A. Gupta, M. K. O'Malley, V. Patoglu, and C. Burgar, "Design, control and performance of ricewrist: a force feedback wrist exoskeleton for rehabilitation

and training," *The International Journal of Robotics Research*, vol. 27, no. 2, pp. 233–251, 2008. 120

Vita

Caroline Black was born and raised in Madison, AL and attended Madison Academy for elementary and high school. She graduated as Valedictorian and recieved a full academic scholarship to the University of Alabama Huntsville (UAH). She received two Bachelor's Degrees in Nursing and Mechanical Engineering while working on undergraduate research in technologies to increase the operational efficiency of hospitals and humanitarian aid distribution. This research led to an offer from Dr. Caleb Rucker to be the first PhD graduate student at his lab at the University of Tennessee Knoxville (UTK). Black was awarded the Chancellor's Fellowship for her first year and then was awarded a National Science Foundation (NSF) Graduate Research Fellowship. While at UTK, she was named the College of Engineerings Outstanding Graduate Student for the year 2015. Along the way, she also organized an event designed to inspire pre-college students to become engineers. Her research resulted in several conference and journal publications, one of which won the award for "Best Manipulator" at the 2014 IEEE Conference on Robotics and Automation (ICRA), held in Hong Kong. She received the Extraordinary Professional Promise commendation from the Chancellor for 2016. She also received the Jimmy and Ileen Cheek Graduate Student Medal of Excellence in 2017. Black graduated with a Masters and Doctorate in Biomedical Engineering in May 2017. She plans to continue her career in Huntsville, AL in industry and education.